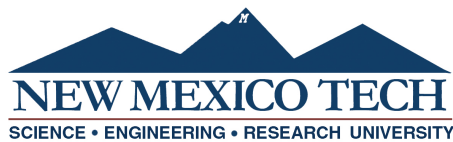


**FULL-FIELD DENSITY MEASUREMENTS IN SUPERSONIC
AND EXPLOSIVELY DRIVEN FLOWS USING
QUANTITATIVE SCHLIEREN**

by

Jessica Cooke

Submitted in Partial Fulfillment
of the Requirements for the Degree of
Masters of Science in Mechanical Engineering
with Specialization in Explosives Engineering



New Mexico Institute of Mining and Technology
Socorro, New Mexico
June, 2025

This thesis is dedicated to...

To my mom and dad, for their continued support and sacrifice. To my sister, who has been a lifelong friend. And to Chloe, who has kept me sane through it all.

Jessica Cooke
New Mexico Institute of Mining and Technology
June, 2025

ACKNOWLEDGMENTS

I would first like to thank my research advisor, Dr. Michael Hargather, for giving me the opportunity and freedom to grow as a researcher. His thoughtful feedback and high standards have pushed me to refine my work and achieve the best results possible. I would also like to thank Dr. Austin Mier for stepping into the role of an advisor and his support in this research. I would also like to thank Dr. Ernst Esch and Eric Larson for their years of mentorship and support.

To everyone in SGDL and EFDL, past and present, thank you for your support, friendship, and long hours. The time and sleep you sacrificed to help set up and test at odd times of the day will not be forgotten. I also want to extend my gratitude to give a special thanks to Dustin Lester, Melton Flores, Budge Jones, Charles Gallegos, and Timothy Collister. Their expertise and dedication made it possible to conduct the high-risk testing required for this research. Without their support, these experiments would not have been possible.

To my family—thank you for your unwavering love and encouragement. Your support has been the foundation that kept me going through every challenge.

Finally, to my dog, Chloe—thank you for keeping me company through it all.

Partial support for this research was provided by Lawrence Livermore National Laboratory through ACT-UP Grant B645442 and by the DOE/NNSA MSIPP program Rio Grande CARES award DE-NA0004108.

This dissertation was typeset with L^AT_EX¹ by the author.

¹The L^AT_EX document preparation system was developed by Leslie Lamport as a special version of Donald Knuth's T_EX program for computer typesetting. T_EX is a trademark of the American Mathematical Society. The L^AT_EX macro package for the New Mexico Institute of Mining and Technology dissertation format was written by John W. Shipman.

ABSTRACT

Quantitative schlieren is an optical technique for measuring density fields in subsonic and supersonic flows. This study extends its application from shock waves surrounding 10° half-angle cone projectiles to measure the density fields of explosively driven shock waves and overlapping axisymmetric shock waves. High-speed imaging is paired with schlieren to capture images of these flow fields. Horizontal and vertical knife-edge schlieren configurations are used to capture refractive angle fields which are quantified using the pixel intensities of a weak lens as a calibration object. By applying an Abel inversion transform and the Gladstone-Dale law, the full density distribution across the flow is reconstructed. Three Abel inversion methods—Two-point, Three-point, and ARAP—are employed to deconvolute the three-dimensional flow within the constrained axisymmetric field. The limitations of Abel inversion are examined by varying the axis of rotation. Results are compared to the well-established Taylor-Maccoll solution for supersonic conical flow, compressible flow relationships, and experimental pressure measurements. Quantitative schlieren is demonstrated to reliably measure density inside conical projectile flows at velocities ranging from Mach 2.09 to 2.67, as well as explosively driven shocks and intersecting shocks using the Two-point Abel inversion.

Keywords: Schlieren; Shocks; High-speed imaging; quantitative

CONTENTS

	Page
LIST OF TABLES	vii
LIST OF FIGURES	viii
NOMENCLATURE	1
CHAPTER 1. INTRODUCTION	1
1.1 Research motivation	1
1.2 Review of Experimental Techniques for Supersonic Flow Diagnostics	1
1.2.1 Quantitative schlieren	2
1.2.2 Tomographic Reconstruction	5
1.2.3 Abel inversion methods	6
1.3 Objectives for present research	9
CHAPTER 2. ANALYSIS IN QUANTITATIVE SCHLIEREN	10
2.1 Calibration	10
2.2 Background subtraction	11
2.3 Makeup of a Schlieren Image	12
2.4 Axis of rotation	13
CHAPTER 3. COMPARISON METHODS	15
3.1 Taylor-Maccoll's analytical solution for conical projectiles	15
3.2 Normal Shock Relationships	16
3.3 Oblique Shocks	17
CHAPTER 4. EXPERIMENTAL METHODS	19
4.1 Conical projectile	19
4.2 High resolution images of conical projectiles, explosively driven shocks, and intersecting shocks	21
4.3 Pressure probe measurements	22

CHAPTER 5. QUANTITATIVE SCHLIEREN DENSITY RECONSTRUCTION OF CONICAL PROJECTILE SHOCKS	25
5.1 Determination of Mach Number from Projectile Images	25
5.2 Density reconstruction from a high resolution image	26
5.3 Density of the conical shock under non-ideal conditions	30
5.4 Density reconstruction from a low resolution image	32
5.5 Uncertainty propagation of high resolution projectile images	33
5.6 Discussion on Using Quantitative Schlieren to Measure Density Inside a Conical Shock	36
CHAPTER 6. EXPERIMENTAL DENSITY RECONSTRUCTION OF EXPLOSIVELY DRIVEN SHOCKS	37
6.1 Characterization of detonators using pressure probes	37
6.2 Quantitative schlieren analysis of explosively driven shocks	41
6.2.1 Lens distortion	44
CHAPTER 7. QUANTITATIVE SCHLIEREN DENSITY RECONSTRUCTION OF INTERACTING CONICAL AND EXPLOSIVELY DRIVEN SHOCKS	47
7.1 Quantitative schlieren of intersecting shocks	47
CHAPTER 8. CONCLUSION AND RECOMMENDATION ON FUTURE WORK	53
8.1 Conclusion	53
8.2 Recommendations for future work	53
REFERENCES	55
APPENDIX A. 1ST APP TITLE	59
A.1 Appendix A: Conical projectile and detonator test plan	59

LIST OF TABLES

Table	Page
5.1 Comparison of The Different Methods for Calculating Projectile Velocity	26

LIST OF FIGURES

Figure	Page
Figure 1.1 Schematic of a quantitative schlieren system.	3
Figure 1.2 Schematic showing how refracted light due to a schlieren object focuses at different locations compared to background light.	4
Figure 1.3 (a) The Abel inverse transform converts a two dimensional projection to a three dimensional object.	7
Figure 2.1 (a) Calibration image of the weak lens. A column of pixels is extracted at the red line. (b) The pixel intensity is graphed against location in the lens. A line of best fit (red line) is applied to the intensity range observed in the projectile image which are shown as the black horizontal lines.	10
Figure 2.2 Difference in projectile images before (top) and after (bottom) background subtraction.	12
Figure 2.3 Images of the same conical projectile. The left image uses a horizontal cutoff, while the right image has a vertical bright-side cutoff. In the right image, a dark region appears on top of the cone, with a bright region beneath it.	12
Figure 2.4 Explosively driven shock from a detonator using (a) horizontal and (b) vertical cutoffs.	13
Figure 2.5 To analyze the shock from a detonator, the Abel inversion can be applied from a (a) horizontal or (b) vertical axis of rotation about the detonator center. The field viewed by the schlieren system and camera is added.	14
Figure 3.1 Conceptual figure showing the pressure as a function of time for an explosively driven shock wave.	17
Figure 4.1 Typical quantitative schlieren set up. The SIMX camera for this test can be replaced with the Nova-R5s seen in Figure 4.2. A 3D printed detonator holder was mounted on the Detonator Cross Beam Holder as seen in Figure 4.3.	20

Figure 4.2	(a) Schematic of the schlieren setup. (b) Schlieren setup modified for pressure probe measurements. (c) Two Nova R5-4K cameras captured horizontal and vertical cutoffs for each image. Light from the schlieren system was split using a beam splitter, filtered by either a horizontal or vertical knife-edge cutoff, and then recorded by the cameras.	22
Figure 4.3	3D-printed Onyx detonator holder with the detonator positioned squarely in front of the gun.	23
Figure 4.4	Shadowgraph image of the detonator shock showing the position of each pressure measurement. The center of the schlieren lenses is 25.4 cm (10 in) from the detonator holder. Scale bar shows the distance from where the detonator was set in cm.	24
Figure 5.1	Three projectiles of varying speeds as noted on each image. The faster projectiles have a smaller shock wave angle.	26
Figure 5.2	Density reconstruction of a projectile traveling at Mach 2.09, captured at a resolution of 2304x4096 pixels. The image was taken with a Phantom Nova R5-4k camera and corresponds with Figures 5.3, 5.4, 5.5, and 5.9	27
Figure 5.3	Air density starting from the surface of the cone, through the shock, and through to atmospheric air. Pixel data was extracted 3.3 cm from the tip of the projectile seen in Figure 5.4.	28
Figure 5.4	High-resolution image of a supersonic conical projectile. The red vertical line indicates the pixel column extracted to generate Figure 5.3. Columns extracted between the solid white lines are graphed in Figure 5.5. The dashed and solid horizontal lines represent the axis of rotation for each Abel inversion. This image was captured with a Photron Nova R5-4k.	29
Figure 5.5	Density was calculated along the shock surrounding the cone. The distance from the cone surface was normalized relative to the shock radius for each analyzed column. The selected schlieren density profile, shown in blue, is the same profile displayed in Figure 5.3, extracted using the two-point Abel inversion at a distance of 3.3 cm from the tip of the cone. Darker gray lines are closer to the tip and lighter gray lines are closer to the base of the projectile.	30
Figure 5.6	Quantitative schlieren density maps of the same projectile using three methods: (a) horizontal knife edge with the dark field, (b) horizontal knife edge with the bright field, and (c) vertical knife edge.	31
Figure 5.7	Comparison of quantitative schlieren using the dark and bright sides of a horizontal cutoff, a vertical cutoff, and the Taylor-Maccoll analytical solution. The calibration lens focal lengths used for each analysis are included in the legend.	32

Figure 5.8	Density reconstruction for Mach 2.13, 2.36, and 2.67 projectiles, respectively, at a low resolution.	33
Figure 5.9	Full compilation of error propagation for the projectile image taken by the Photron Nova R5-4k. The bold lines represent the measured normalized density and the normalized index of refraction $\delta + 1$ along with one standard deviation error regions.	33
Figure 5.10	Intensity deviations from the background is the primary contributor to error.	35
Figure 5.11	Breakdown of error contributions for projectile tilt, spacial uncertainty due to pixel location, and pressure and temperature.	35
Figure 6.1	Three sets of pressure ratio measurements taken at three different locations in the schlieren lenses. Best fit of the shock front shows the decay of the shock front's pressure ratio as it travels further from the detonator.	38
Figure 6.2	Three sets of images taken one after the other of the 15 frames captured using the SIMX Framing camera. Shocks vary despite detonators being placed in the same place for every test.	39
Figure 6.3	The difference between the density when using the Mach number from the inter-frame velocity or the pressure ratio from the PCB probe to compute an assumed temperature is negligible.	40
Figure 6.4	Three quantitative schlieren measurements are overlaid onto the density plot in Figure 6.3, using the inter-frame Mach number to estimate temperature. The solid lines represent quantitative schlieren data obtained with a vertical knife edge. The peak densities from two corresponding horizontal knife edge schlieren measurements are shown as points.	41
Figure 6.5	Quantitative schlieren of an explosively driven shock: (a) Density map using a horizontal knife-edge cutoff, (b) density map using a vertical knife-edge cutoff	42
Figure 6.6	(a) density profile along the white line from the horizontal cutoff image, and (b) density profile along the white line from the vertical cutoff image. In (b), the vertical axis.	43
Figure 6.7	Comparison of two quantitative schlieren density profiles: one with a vertical cutoff and one with a horizontal cutoff.	44
Figure 6.8	Vectors showing how each point in the mesh shifts relative to the location the point would be without distortion.	45
Figure 6.9	Histogram showing the frequency horizontal and vertical pixels are distorted and to what magnitude.	46

Figure 7.1	Shock features formed from the intersecting shocks: (a) atmosphere, (b) conical shock from atmosphere, (c) explosively driven shock (d) conical shock from the explosively driven shock, (e) reflection shock off the conical projectile	48
Figure 7.2	Progression of the shocks intersecting over 15 frames taken with the SIMX framing camera.	49
Figure 7.3	Projectile flying through an explosively driven shock. (a) horizontal cutoff schlieren image and (b) vertical cutoff schlieren image	49
Figure 7.4	Quantitative schlieren density map using a horizontal knife edge cutoff.	50
Figure 7.5	Density measured with quantitative schlieren compared to compressible shock relationships.	51
Figure 7.6	Angles can be measured for sections of the flow.	52

NOMENCLATURE

β	Shock wave angle
$\delta(r_i)$	Deviation in refractive index at radial position r_i
ϵ	Angle of refraction
ϵ_j	Local refraction angle at the j -th azimuthal position
$\frac{dn}{dy}$	Derivative of refractive index in the y direction
γ	Ratio of specific heats
ρ	Density
ρ_1	Atmospheric density
ρ_2	Density behind the shock
Θ	Taylor-Maccoll flow angle
θ	Turn angle
$A_{i,j}$	Matrix for Abel inversion calculation
$B_{i,j}$	Matrix for Abel inversion calculation
$C_{i,j}$	Matrix for Abel inversion calculation
$D_{i,j}$	Matrix for Abel inversion calculation
dz	Depth of refracting object
f	Effective focal length
f_1	Focal length of the collimating lens
f_2	Focal length of the schlieren object
i, j	indices
k	Gladstone Dale coefficient
M	Mach number

M_1	Shock Mach number
M_{n1}	Normal Mach component
n	Index of refraction
$n(r_i)$	Refractive index at radial position r_i
n_0	Reference refractive index
P	Pressure
P_1	Atmospheric pressure
P_2	Pressure behind the shock
R	Specific gas constant for air
r	Radial position
T	Temperature
T_1	Atmospheric temperature
T_2	Temperature behind the shock
V	Normalized radial velocity component
v	Velocity
V_w	Radial velocity component at the cone surface
V_{2r}	Radial velocity component immediately behind a conical shock

This dissertation is accepted on behalf of the faculty of the Institute by the following committee:

Michael J. Hargather

Academic and Research Advisor

Frank Austin Mier

William Anderson

I release this document to the New Mexico Institute of Mining and Technology.

Jessica Cooke

May 12, 2025

CHAPTER 1

INTRODUCTION

1.1 Research motivation

The ability to measure density fields in supersonic, complex, and hypersonic flows is essential to validate computational and analytical models used to design and predict the behavior of aircraft and shock waves. Quantitative schlieren has previously been established as an effective experimental method for measuring density fields within the flow surrounding a supersonic conical projectile [1]. This technique has been primarily applied under ideal conditions to capture flow fields and provide detailed density measurements within conical shock structures. The present work extends quantitative schlieren beyond this ideal case by expanding the technique to incorporate multiple cutoff directions across multiple interacting shock waves in high-resolution images. Ultimately, this effort aims to measure the flow field around a supersonic projectile penetrating an explosively driven shock and provide a comprehensive understanding of quantitative schlieren's limitations in non-ideal conditions. Explosively driven shocks are also studied to establish a baseline for validation. High-resolution schlieren images identify and characterize regions within the overlapping shocks, while results are validated through analytical methods and experimental data.

1.2 Review of Experimental Techniques for Supersonic Flow Diagnostics

Understanding fluid flow properties is essential when designing supersonic systems in aircraft, ballistics, and propulsion. Key parameters include temperature, pressure, density, and Mach number. Analytical solutions, such as Taylor-Maccoll's method for conical shocks [2, 3], Prandtl-Meyer expansion theory, and Rankine-Hugoniot relations, provide theoretical models for compressible flows [4]. However, these models assume ideal conditions and do not account for real-world complexities, especially when ideal gas law assumptions break down, such as in hypersonic flows where high-temperature effects like dissociation and ionization alter gas behavior. Computational Fluid Dynamics (CFD) provides a numerical approach for predicting fluid properties, but as flow complexity increases, validation becomes important. As a result, various experimental techniques have been developed to measure flow properties.

Supersonic flow is difficult to measure due to the transient nature of many relevant events, such as shock waves and detonation fronts. Supersonic wind tunnels were developed to study the aerodynamics of objects such as cones and airfoils by controlling the flow to be supersonic rather than by accelerating the object itself. Imaging is generally easier to perform in these controlled environments, as time constraints are reduced and seeding the flow with small, trackable particles or droplets to visualize fluid motion is more straightforward. An optical method, one which can measure the entire flow field simultaneously without implementing sensors and other obstructions into the flow field, is preferred [5]. Methods of characterizing fluid flow, such as laser Doppler velocimetry (LDV) and particle image velocimetry (PIV), which utilize laser-based systems to non-intrusively measure velocity profiles, are well suited [6, 7].

However, for transient supersonic events such as explosively driven shocks or detonation waves which cannot be easily replicated in wind tunnels, diagnostic tools such as piezoelectric pressure transducers, pyrometers, and Doppler-based velocimetry techniques are employed for time-resolved measurements [8–10]. Traditional intrusive methods include orifice plates, venturi meters, and pitot tubes, which measure pressure differentials and velocity by directly interacting with the flow [4, 11]. These techniques have become dated because of their intrusive nature and limitation to point-specific measurements. Affixing sensors to costly or compact experimental vehicles introduces additional layers of complexity and frequently restricts testing to wind tunnels. These challenges are further exacerbated in hypersonic flow conditions [12]. Other methods, such as PIV or particle tracking velocimetry (PTV), enable flow visualization and analysis, but these require adequate particle seeding and tracking algorithms [13].

1.2.1 Quantitative schlieren

Air is a transparent medium, making its flow characteristics invisible to the naked eye. Specialized flow visualization techniques are required to visualize and measure variations in density and refractive index within these otherwise invisible flow fields. These methods provide both qualitative and quantitative insights into fluid motion. Traditional techniques, such as schlieren imaging and shadowgraphy, have been widely applied to capture density gradients in compressible flows [1, 14]. When coupled with high-speed cameras, these techniques reveal transient features such as shock structures, flow separation, and turbulence. While primarily qualitative, schlieren and shadowgraphy can also support quantitative analysis, such as determining shock angles and applying compressible flow relations including isentropic flow equations, normal and oblique shock relations, and conical shock solutions [4]. Additionally, high-speed imaging enables velocity measurements by tracking feature displacement over time.

Shadowgraph imaging is a technique used to visualize both subsonic and supersonic flows by detecting changes in fluid density. As light passes through the flow field, variations in refractive index caused by density gradients bend the

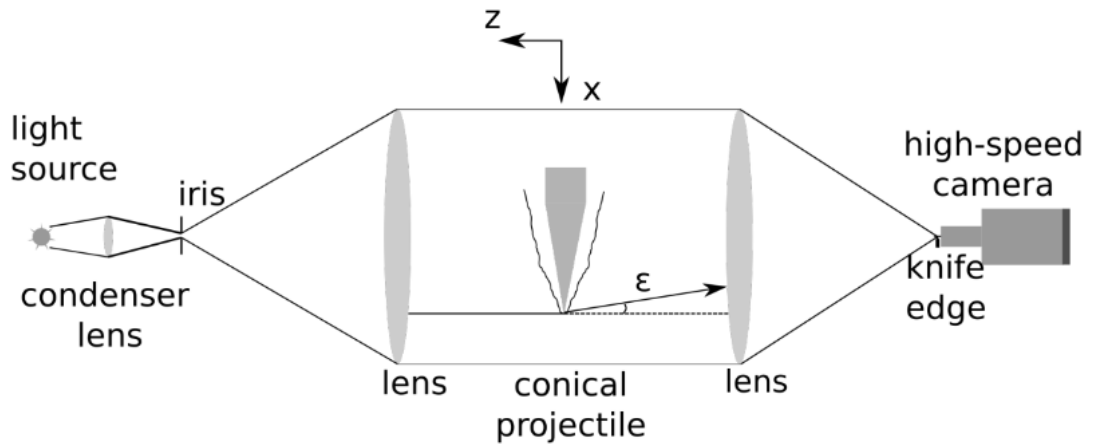


Figure 1.1: Schematic of a quantitative schlieren system.

light rays, resulting in the formation of shadows on the imaging plane or camera. These shadows highlight regions with rapidly changing density, such as shock wave fronts and expansion fans [14]. The pixel intensity in a shadowgraph image corresponds to the second spatial derivative of the refractive index, making the technique particularly sensitive to sharp gradients and discontinuities. Due to its high contrast and responsiveness to steep changes in density, shadowgraphy is typically used for qualitative analysis of flow structures, including shock waves, expansion fans, oblique shocks, and conical shocks. However, quantitative estimates can still be obtained by analyzing the position and geometry of these features within the image.

For visualizing more subtle density variations, such as thermal gradients, internal shock structure, or subsonic plumes, schlieren imaging is more effective. Unlike shadowgraphy, which responds to the second spatial derivative of the refractive index, schlieren is sensitive to the first derivative, allowing it to capture more gradual changes in flow properties.

Schlieren imaging works by detecting changes in the refractive index of a transparent medium, which correspond to variations in density or gas composition. These refractive index gradients bend light rays passing through the flow field by an amount known as the refractive angle (ϵ_y). To capture this effect, a standard schlieren setup includes a point light source, collimating optics to produce a parallel beam, a test section, a knife edge positioned at the optical focal point, and a camera for image capture, as shown schematically in Figure 1.1. The light is first collimated to ensure that rays enter the test section without any initial angular deviation. As the collimated rays traverse the test section, any local refractive gradients from a schlieren object deflect them. These deflected rays are then focused by a lens or mirror onto the knife edge, which partially blocks them based on their angle of refraction. This selective cutoff converts refractive angle variations into brightness variations in the final image. This process is shown

schematically in Figure 1.2. The thin lens equation best describes the behavior of the optical system:

$$\frac{1}{f} = \frac{1}{f_1} + \frac{1}{f_2} \quad (1.1)$$

Here, f is the effective focal length, determined by f_1 (the focal length of the collimating lens) and f_2 (the effective focal length change due to the schlieren object). Variations in refractive angle alter the focal length, producing intensity variations in the final image. Light and dark regions correspond to the magnitude of density gradients and the direction the gas is moving relative to the knife edge.

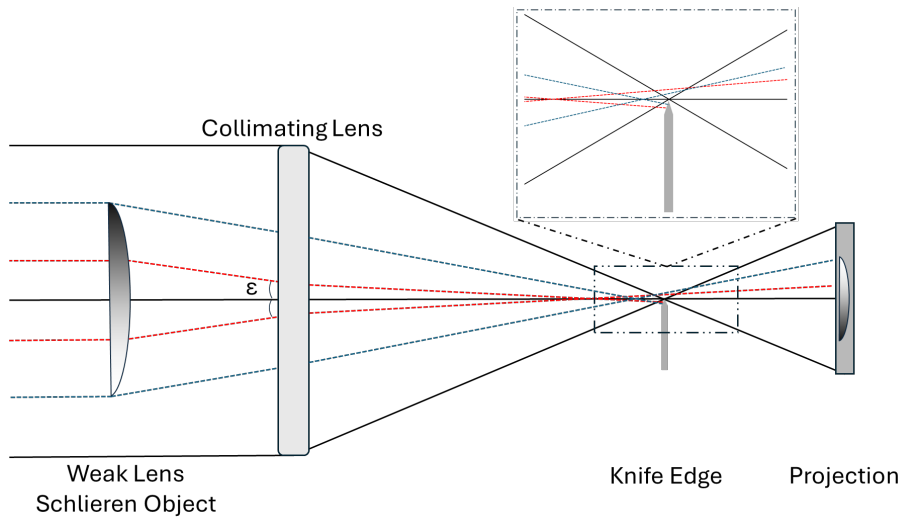


Figure 1.2: Schematic showing how refracted light due to a schlieren object focuses at different locations compared to background light.

Quantitative schlieren uses this setup to measure the refractive angle field produced by a flow to calculate the index of refraction and density field. The amount of light blocked at the knife edge is proportional to the local refractive angle, creating a continuous gradient of pixel intensities. By comparing these intensities to those from a reference image of a known object, such as a weak lens, the refractive angles in the test image can be mapped [1, 14–16]. The relationship between refractive angle and refractive index n is given by:

$$\epsilon_y = \frac{1}{n} \int \frac{dn}{dy} dz \quad (1.2)$$

The refractive angle at each point depends on the local refractive index, which is influenced by gas density and composition, and on the path length the

light travels through the medium. The schlieren image is a two-dimensional projection of a three-dimensional object. A form of tomography must be used here to deconvolute the refractive angle field to solve the line path integral. Finally, the Gladstone-Dale law, which relates gas density to a refractive angle, can be used to determine density once the refractive index is known:

$$n - 1 = k\rho \quad (1.3)$$

where ρ is the gas density and k is the Gladstone-Dale constant, specific to the gas. Here, the medium is all air and $k = 0.000226 \text{ m}^3/\text{kg}$.

1.2.2 Tomographic Reconstruction

Schlieren images provide two-dimensional projections of three-dimensional refractive index fields. Because each pixel records the integrated effect of refractive index variations along the entire optical path, the resulting image does not directly reveal the local refractive properties of the flow. This line-of-sight integration obscures important spatial variations and makes it difficult to distinguish between regions of high density and regions where the ray simply traveled through more material.

This is seen in the case of the conical flow field analyzed here. Light rays passing closer to the cone's surface encounter not only higher-density gas, but also traverse longer path lengths due to the curved geometry of the shock. As a result, the measured refractive angle at each pixel reflects a combination of both local density and cumulative path effects. To recover the underlying spatial distribution of refractive index, tomographic reconstruction must be applied.

There are several tomographic methods for determining the path length of light in a fluid. The most straightforward approach would be to confine the medium to a known volume, making the path length well-defined. However, this is only feasible for solids, whereas fluids' volume is not easily controlled. Filtered Back Projection (FBP) [17, 18] and other Radon inversion methods can reconstruct flow fields but require multiple fields of view, which are difficult to achieve in quantitative schlieren due to practical limitations on the number of cameras and viewing angles. Algebraic Reconstruction Technique (ART) is an iterative method for reconstructing three-dimensional fields from a limited number of projections, but it still requires more than two views [19]. Proper Orthogonal Decomposition (POD) combined with tomography extracts dominant flow features over time using multiple schlieren images but also requires more than two projections [20].

1.2.3 Abel inversion methods

In the case of an axisymmetric flow, such as the flow surrounding a conical projectile, an Abel inversion can be applied to reconstruct the full refractive field from the schlieren image [21, 22]. The Abel inversion is a specific case of the Radon transform [23], which assumes that one projection view is identical to any other around an axis. Several Abel inversion methods, such as Two-point, Three-point, ARAP, and onion-peeling, have been developed for discrete analysis, each offering different levels of noise control [24, 25].

Here, the two-point Abel inversion, the three-point Abel inversion, and the ARAP Abel inversion are compared in their reliability to reconstruct the density across the shock wave and to the projectile surface. The two-point Abel inversion does not employ any smoothing and is the simplest of the three methods compared here [21, 26]:

$$\delta(r_i) = \sum_{j=i}^{N+1} D_{i,j} \cdot \epsilon_j \quad (1.4)$$

$$D_{i,j} = \begin{cases} \frac{1}{\pi} (A_{i,j} - A_{i,j-1} - jB_{i,j} + (j-2)B_{i,j-1}), & \text{if } j > i \text{ and } j \neq 2, \\ \frac{1}{\pi} (A_{i,j} - jB_{i,j} - 1), & \text{if } j > i \text{ and } j = 2, \\ \frac{1}{\pi} (A_{i,j} - jB_{i,j}), & \text{if } j = i \text{ and } i \neq 1, \\ 0, & \text{if } j = i = 1 \text{ or } j < i. \end{cases} \quad (1.5)$$

$$A_{i,j} = \sqrt{j^2 - (i-1)^2} - \sqrt{(j-1)^2 - (i-1)^2} \quad (1.6)$$

$$B_{i,j} = \ln \left(\frac{j + \sqrt{j^2 - (i-1)^2}}{(j-1) + \sqrt{(j-1)^2 - (i-1)^2}} \right) \quad (1.7)$$

$$\delta(r_i) = \frac{n(r_i)}{n_0} - 1 \quad (1.8)$$

The deviation in the refractive index, $\delta(r_i)$, is calculated to obtain the refractive index at a given radial position $n(r_i)$ relative to n_0 , the ambient refractive index. The variable $D_{i,j}$ represents the difference value at radial position i and azimuthal angle j which are summarized using the variables $A_{i,j}$ and $B_{i,j}$. The radial position in the image is denoted by r_i , and e_j represents the local refraction angle at azimuthal position j , which is determined from the intensity values in the image. These variables are used in the two-point and three-point Abel inversion processes to determine the refractive index across the shock wave.

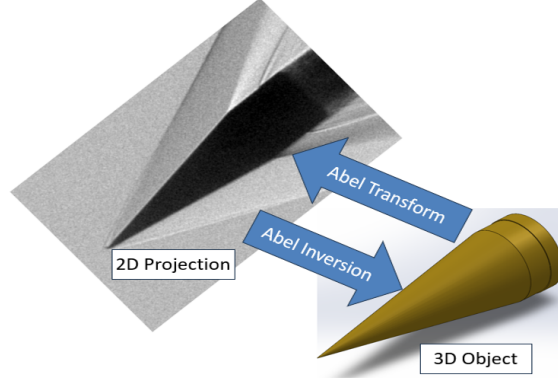


Figure 1.3: (a) The Abel inverse transform converts a two dimensional projection to a three dimensional object.

The three-point Abel inversion method improves on the two-point method by considering local changes in the projection data, making it suitable for smoothing noise and sharp edges. This approach divides the Abel integral into segments around each point r_j , where projection data is approximated as a quadratic function. This expansion around each point smooths noise more effectively but introduces non-zero $D_{i,i-1}$ terms. These segments are then integrated analytically, creating a smoothing effect which is especially useful for noisy data. The three-point Abel inversion is performed via a process similar to the two-point method but with expanded coefficient matrices [22]. The three-point method described by Sipkens et. al. [25] is used:

$$\delta(r_i) = \sum_{j=i}^N D_{i,j} \cdot \epsilon_j \quad (1.9)$$

$$D_{i,j} = \begin{cases} 0, & \text{if } j < i - 1, \\ A(i, j + 1) - B(i, j + 1), & \text{if } j = i - 1, \\ A(i, j + 1) - B(i, j + 1) + 2 \cdot B(i, j), & \text{if } j = i, \\ A(i, j + 1) - B(i, j + 1) + 2 \cdot B(i, j) \\ \quad - A(i, j - 1) - B(i, j - 1), & \text{if } j \geq i + 1, \\ A(i, j + 1) - B(i, j + 1) + 2 \cdot B(i, j) \\ \quad - 2 \cdot B(i, j - 1), & \text{if } i = 0 \text{ and } j = 1. \end{cases} \quad (1.10)$$

$$A(i, j) = \begin{cases} 0, & \text{if } j < i \text{ or } (j = i \text{ and } i = 0), \\ \frac{1}{2\pi} \ln \left(\frac{\sqrt{(2j+1)^2 - 4i^2} + 2j + 1}{2j} \right), & \text{if } j = i \text{ and } i \neq 0, \\ \frac{1}{2\pi} \ln \left(\frac{\sqrt{(2j+1)^2 - 4i^2} + 2j + 1}{\sqrt{(2j-1)^2 - 4i^2} + 2j - 1} \right), & \text{if } j > i. \end{cases} \quad (1.11)$$

$$B(i, j) = \begin{cases} 0, & \text{if } j < i, \\ \frac{\sqrt{(2j+1)^2 - 4i^2}}{2\pi} - 2j \cdot A(i, j), & \text{if } j = i, \\ \frac{\sqrt{(2j+1)^2 - 4i^2} - \sqrt{(2j-1)^2 - 4i^2}}{2\pi} - 2j \cdot A(i, j), & \text{if } j > i. \end{cases} \quad (1.12)$$

$$\delta(r_i) = \frac{n(r_i)}{n_0} - 1 \quad (1.13)$$

Sipkens's *et. al.* arbitrary ray axisymmetric projection (ARAP) [25] is the last Abel inversion considered here. Unlike a traditional Abel transform, which assumes parallel rays, ARAP accounts for rays that diverge or converge. The equations for ARAP are not reproduced here, but are well identified in [25].

The result of the Abel inversion process is the index of the refraction field as a function of distance. Finally, the Gladstone-Dale law is used to determine the density from the refractive index [14].

Abel reconstruction methods have been compared previously in the literature for incompressible low-speed flows [22, 27, 28]. Many of these previous works have identified the advantages of smoothing in the reconstruction algorithms. These techniques have not been applied to compressible flows with shock waves before, for which smoothing is expected to negatively affect the ability to reconstruct shock waves.

1.3 Objectives for present research

This research aims to develop and validate quantitative schlieren as a supersonic measurement tool and investigate its limitations. The objectives of this research are to:

- Measure the density field in supersonic conditions including conical projectiles over a range of velocities, explosively driven shocks, and intersecting shocks validated against preexisting compressible flow theory and pressure probe data.
- Explore alternative Abel inversion transforms for flows with step change density features seen in shocks.
- Perform quantitative schlieren with multiple knife orientations including vertical and horizontal knife orientations and dark and bright field analysis.
- Investigate sources of error and strategies for mitigating error.

CHAPTER 2

ANALYSIS IN QUANTITATIVE SCHLIEREN

A weak lens relates the intensities of a supersonic flow image to a refractive angle field. An Abel inversion deconvolutes the two-dimensional schlieren projection into a three-dimensional field to obtain a refractive index field from the refractive angle. The Gladstone-Dale Law converts the index of refraction of air to a density field. Results are compared against compressible flow theory and experimental pressure probe data.

2.1 Calibration

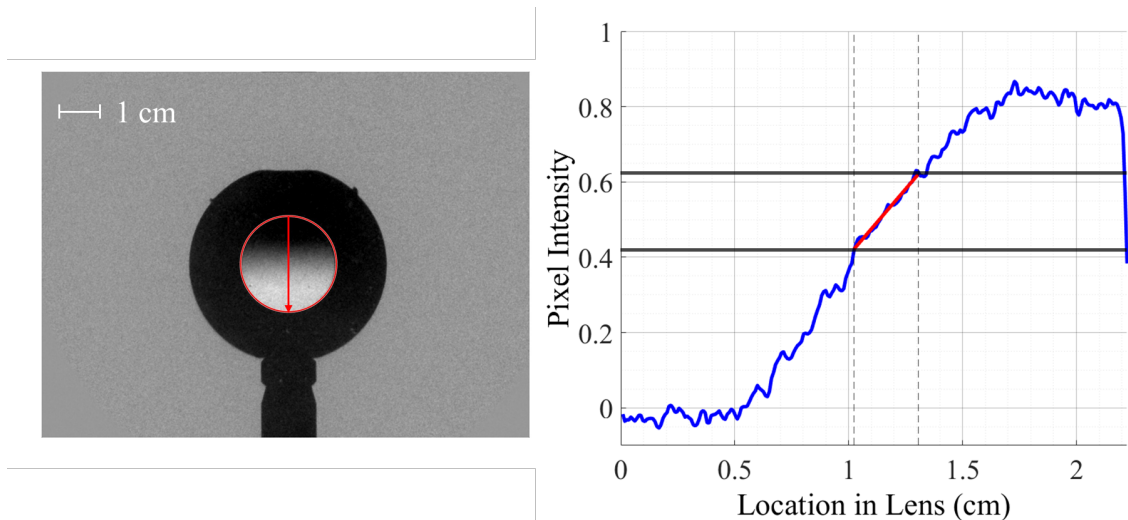


Figure 2.1: (a) Calibration image of the weak lens. A column of pixels is extracted at the red line. (b) The pixel intensity is graphed against location in the lens. A line of best fit (red line) is applied to the intensity range observed in the projectile image which are shown as the black horizontal lines.

Before each test, a calibration image and a bright-field background image were recorded. The calibration image featured a weak lens placed in the middle of the test section, which was used to establish the relationship between refractive

angle and pixel intensity [15]. A weak lens is defined as having a focal length longer than that of the schlieren imaging lens. In this case, a calibration lens with a 5 m focal length was used. An ideal calibration image exhibits a strong intensity gradient that spans the full range of intensities present in the flow region being analyzed. An image of a calibration lens is shown in Figure 2.1.

The maximum expected ray deflection, calculated using the Gladstone–Dale law and Equation 2.1, is 31 arcseconds. The maximum measurable deflection angle for this quantitative schlieren system, as defined in [14], is 37 arcseconds:

$$\epsilon_{\max} = 2 \left(\frac{n}{n_0} - 1 \right) \quad (2.1)$$

Here, n is the maximum index of refraction based on the peak density from the conical shock, n_0 is the ambient (atmospheric) index of refraction, and ϵ_{\max} is the maximum deflection angle the system can resolve at that density. Thus, the theoretical deflection caused by the supersonic shock lies within the detectable range of the schlieren setup.

To determine the relationship between pixel intensity and refractive angle, a line was fit to the curve of measured intensities across the reference lens image. Only intensity values within the linear response region—bounded by the minimum and maximum intensities observed in the analyzed area of the flow image—were included in the fit. These bounds, indicated by dashed lines in Figure 2.1, exclude regions where the response becomes nonlinear to ensure accuracy. The resulting linear equation was then used to map pixel intensities to their corresponding physical locations on the lens, enabling calculation of refractive angles based on the known focal length [15]. A pixel-to-length conversion was also established by measuring the known diameter of the lens holder.

2.2 Background subtraction

The bright-field background image was captured by emptying the test section and taking an image with the laser illumination on. This image was used in the analysis to remove lens dirt and background noise by subtracting the image from the calibration and test images. This subtraction not only reduces noise but also ensures uniformity in the backgrounds of these images. Figure 2.2 demonstrates background subtraction removing dirt, uneven lighting, and noise from a projectile image. Later, when determining the refractive angle from pixel intensity, the background intensity serves as a reference for atmospheric conditions, where the refraction angle is zero. The background intensity is calculated by averaging as many background pixels as possible, sampled from both the flow and calibration images. Excluded from this sampling are regions such as the calibration lens, the projectile, the surrounding flow fields, and the borders where the lens clips the light. Note that quantitative schlieren is best performed with perfectly uniform background intensity, which is not always practical to achieve so the background subtraction allows for small experimental variations [15, 21, 29].

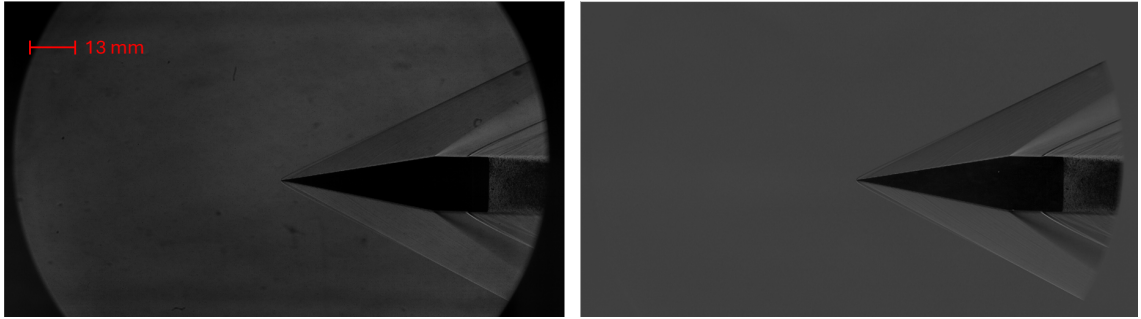


Figure 2.2: Difference in projectile images before (top) and after (bottom) background subtraction.

2.3 Makeup of a Schlieren Image

A schlieren system measures refractive angle changes by selectively blocking refracted light with a knife-edge cutoff. One of the most fundamental adjustments in schlieren imaging is the orientation of this cutoff—whether vertical, horizontal, or angled. Although any cutoff can be used, the most effective orientation is perpendicular to the dominant flow refractive index gradients, as this maximizes grayscale intensity variation in recorded images and enhances sensitivity to the density gradients.

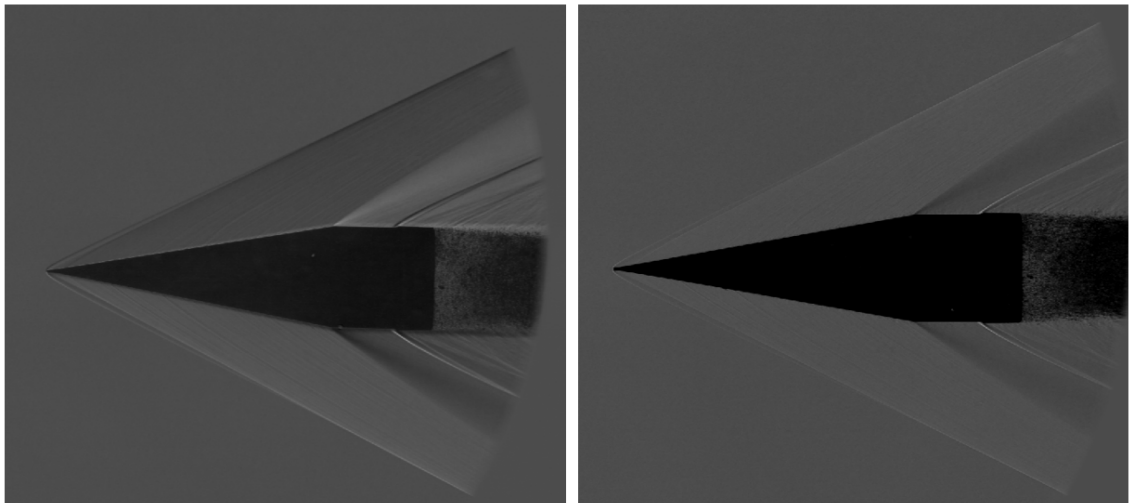


Figure 2.3: Images of the same conical projectile. The left image uses a horizontal cutoff, while the right image has a vertical bright-side cutoff. In the right image, a dark region appears on top of the cone, with a bright region beneath it.

The airflow around a small-angle supersonic conical projectile primarily refracts light normal to the shock, resulting in greater vertical displacement than

horizontal. Because a horizontal knife edge emphasizes vertical refractive gradients, it is typically preferred for imaging supersonic conical projectiles with shock wave angles less than 45 degrees, as this provides optimal contrast. However, a vertical knife-edge can still be used if the camera has sufficient bit depth to capture the smaller grayscale variations with low noise. Figure 2.3 compares a horizontal cutoff to a vertical cutoff for the same projectile.

In a schlieren system, light is either refracted around the knife edge or blocked by it, producing distinct light and dark regions. The pixel intensity reflects the magnitude of the light's deflection, while whether a region appears brighter or darker indicates the direction of deflection relative to the knife edge. In the case of a supersonic projectile, a vertical knife edge results in an image that is bright or dark, since the airflow is displaced primarily in one direction. In comparison, a horizontal knife edge image of the same projectile produces a bright and dark region where the refractive angle is either deflected down or up. The specific appearance depends on the orientation of the knife edge and the direction of the flow-induced deflection. Here, quantitative schlieren will be applied to both bright and dark regions to reconstruct the flow field density.

2.4 Axis of rotation

A key component of quantitative schlieren is using a tomographic transform to account for the three-dimensional nature of the shock as the schlieren image is a two-dimensional projection. To solve the required path line integral and isolate the index of refraction, the Abel inversion is applied for explosively driven and conical shocks [21, 22]. The Abel inversion process starts from outside the flow field to a center rotation axis and assumes that the projection about this axis is the same from any view. Because of this, the Abel inversion is limited to axisymmetric flows.

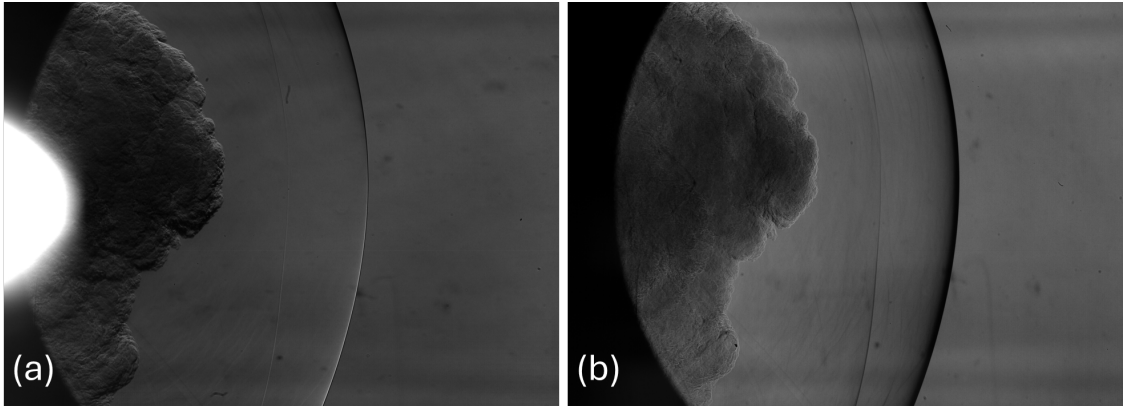


Figure 2.4: Explosively driven shock from a detonator using (a) horizontal and (b) vertical cutoffs.

A conical projectile with no angle of attack is well suited for the Abel inversion when the axis of rotation is taken along the projectile's centerline. However, in the case of detonators, the overall detonation field is not axisymmetric [30]. Only portions of the shock, such as those captured within the camera frame in Figure 2.4, exhibit symmetry. This paper investigates two axes of rotation, one at the detonator's origin and another within the local geometry of the recorded schlieren images, to assess whether the non-axisymmetric shock field surrounding a detonator can be reasonably approximated using local symmetry and the Abel inversion.

The axis of rotation is also dependent on the knife-edge orientation. Both horizontal and vertical knife-edge cutoffs were used to measure the density of the explosively driven shock. Two axes of rotation were explored: one horizontal, centered on the blast, and another ideally vertically positioned at the detonator's location. Figure 2.5 shows a schematic of both methods.

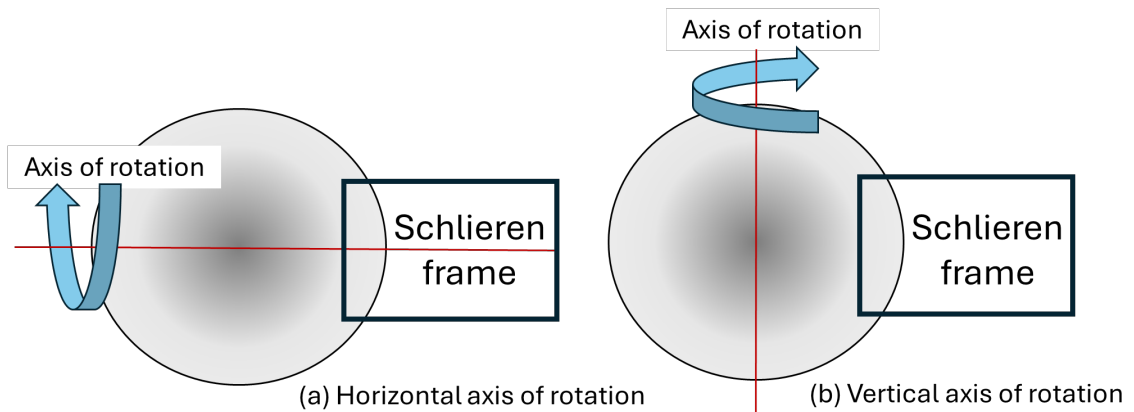


Figure 2.5: To analyze the shock from a detonator, the Abel inversion can be applied from a (a) horizontal or (b) vertical axis of rotation about the detonator center. The field viewed by the schlieren system and camera is added.

A horizontal knife edge is paired with a horizontal axis of rotation, while a vertical knife edge aligns with a vertical axis of rotation. The direction of light refraction, visualized by the knife-edge as the grayscale gradient, is the strongest perpendicular to the knife-edge cutoff. Extracting a row or column across this gradient is best to capture the strongest diversity. Hence, the axis of rotation should be parallel to the knife edge. In detonators refract light radially, certain regions of the shocked air move entirely vertically or horizontally, resulting in no gradient in these sections for their respective cutoff orientation. In contrast, conical projectiles refract the light at an angle along the shock front, leading to a more uniformly distributed motion.

CHAPTER 3

COMPARISON METHODS

Before quantitative schlieren can be verified as an experimental method for measuring density fields, it must first be validated with existing theory and experimentation. This includes understanding the limitations of quantitative schlieren using an Abel inversion and predicting reasons for deviation from theory. Compressible flow equations such as normal shock relationships, oblique shock relationships, and Taylor-Maccoll's analytical solution for conical shocks are combined with experimental data from pressure probes to gauge the accuracy of quantitative schlieren.

3.1 Taylor-Maccoll's analytical solution for conical projectiles

The densities reconstructed using the three Abel inversion methods are compared to the Taylor and Maccoll analytical solution for supersonic conical flows. The Taylor-Maccoll solution is commonly used to compare experimentally measured properties of conical flows, such as those observed in wind tunnel and ballistic experiments [2, 3]. This solution applies the principles of conservation of mass, momentum, and energy to a conical shock in terms of the cone angle and shock wave angle. The model assumes isentropic, irrotational, and axisymmetric flow between the shock wave and the cone surface, simplifying the problem into an ordinary differential equation. By solving this equation numerically, the Mach number, pressure, temperature, and density are determined from the cone surface to the shock wave [4, 31, 32]. Taylor-Maccoll provides solutions along the shock front and near the surface of the conical projectile, with density ratios inside the shock being linearly approximated between these two regions. The governing equation for the flow field around the conical shock is:

$$\frac{dV}{d\Theta} = \frac{2V(1 - V^2)}{\sin \Theta(1 - M_{tm}^2 V^2) - V} \quad (3.1)$$

where V is the normalized radial velocity component, Θ is the flow angle measured from the cone axis, and M_{tm} represents the local Mach number of the flow [4, 33].

The shock angle β can be related to the cone angle θ using the θ - β - M relationship:

$$\tan \theta = \frac{2 \cot \beta (M^2 \sin^2 \beta - 1)}{M^2(\gamma + \cos 2\beta) + 2} \quad (3.2)$$

where θ is the flow deflection angle (half the cone angle), β is the shock wave angle (the angle between the incoming flow direction and the shock front), M is the Mach number of the conical projectile, and γ is the specific heat ratio of the gas (1.4 for air).

The density ratio across the shock can be expressed as:

$$\frac{\rho_b}{\rho_{atm}} = \frac{(\gamma + 1)M^2 \sin^2 \beta}{(\gamma - 1)M^2 \sin^2 \beta + 2} \quad (3.3)$$

where ρ_b is the post-shock density and ρ_{atm} is the ambient atmospheric density. Near the cone surface, the density ratio is approximated by:

$$\frac{\rho_w}{\rho_b} = \frac{V_{2r}}{V_w} \quad (3.4)$$

where V_{2r} is the radial velocity component immediately behind the shock and V_w is the radial velocity component at the cone surface [34].

3.2 Normal Shock Relationships

Normal shock relationships are used to determine properties across one-dimensional shocks, such as those generated by a detonator. The pressure, density, and temperature ratios are all related through the Mach number of the shock, allowing the density ratio to be determined directly if any of these values are known.

The normal shock relations, which convert Mach number to pressure, temperature, and density ratios, are given by [4, 34–36]:

$$\frac{P_2}{P_1} = 1 + \frac{2\gamma}{\gamma + 1}(M_1^2 - 1) \quad (3.5)$$

$$\frac{T_2}{T_1} = \frac{(2\gamma M_1^2 - (\gamma - 1))((\gamma - 1)M_1^2 + 2)}{(\gamma + 1)^2 M_1^2} \quad (3.6)$$

$$\frac{\rho_2}{\rho_1} = \frac{(\gamma + 1)M_1^2}{(\gamma - 1)M_1^2 + 2} \quad (3.7)$$

where M_1 is the Mach number of the shock front, P_2 is the pressure behind the shock, P_1 is the ambient pressure, ρ_2 is the density behind the shock, and ρ_1 is the ambient density.

Density is calculated using the ideal gas law, room temperature, and room pressure:

$$\rho = \frac{P}{RT} \quad (3.8)$$

where P is the pressure, T is the temperature, and $R = 287.0528 \text{ J/kg/K}$ is the specific gas constant for air. This can be applied anywhere in the air flow using local static properties. If the atmospheric density is required, room temperature and pressure should be measured.

As the explosively driven shock expands radially, pressure and density decrease. Figure 3.1 illustrates a typical pressure or density profile across an expanding explosively driven shock. The spike at the front indicates the initial shock jump, followed by a relaxation in pressure and density. Inside the shock, normal shock relations cannot be directly applied as the Mach number conditions change. Instead, the ideal gas law is extended to estimate density inside the shock using pressure measurements from a probe [21]. A temperature must be assumed to use the ideal gas law, and here, a linearly varying temperature is used, assuming the temperature decays with density. The temperature across the shock is solved using the normal shock temperature relation (eq. 3.6), and this temperature is multiplied by a measured atmospheric temperature. The temperature is then linearly varied from this shock temperature to the atmospheric temperature as the density reaches the ambient value.

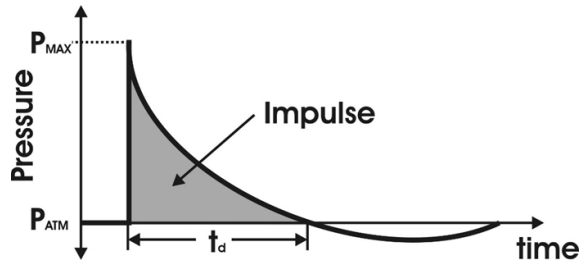


Figure 3.1: Conceptual figure showing the pressure as a function of time for an explosively driven shock wave.

3.3 Oblique Shocks

Unlike normal shocks, oblique shocks are two-dimensional and have both normal and tangential components. The shock-induced changes occur in the normal direction and the tangential component is not used for the pressure change. The normal component is given by [4, 34]:

$$M_{n1} = M_1 \sin \beta \quad (3.9)$$

where M_1 is the Mach number of the incoming flow, M_{n1} is the normal component of the flow, and β is the wave angle. This normal component can be used directly in the normal shock equations to determine the density, pressure, and temperature ratios.

Mach number (M_1), wave angle, and turn angle are related through the θ - β - M relationship (eq. 3.2). The wave angle, which comes from the surface deflection, is usually known, allowing the Mach number to be calculated through the wave angle, or vice versa.

CHAPTER 4

EXPERIMENTAL METHODS

A schlieren set-up was used in conjunction with high speed cameras, a coherent spoiled laser, and timing equipment to capture images of various supersonic events. Images were captured of the event, a calibration lens image, and a background. Horizontal and vertical knife edge images were synonymously captured using Photron Nova R5s with separate optical paths via a beam splitter. Multiple frames were captured with a Specialized Imaging SIMX framing camera to track shock speeds.

4.1 Conical projectile

High-speed imaging was partnered with quantitative schlieren to capture images of supersonic projectiles in free flight. Each test featured a 10-degree half-angle, 0.50-inch (12.7-mm diameter) conical projectile, which was accelerated to speeds exceeding Mach 2 (680 m/s). The projectiles were fired from a rifled barrel using IMR-7828 powder as the propellant.

A light gate was placed after the gun barrel exit to trigger the cameras. The trigger time was adjusted using a delay generator based on the projectile speed and the distance to the quantitative schlieren test section, which was approximately 30 cm from the barrel exit. The cameras used in this study included a Photron Nova R5-4k, Phantom VEO 990S, and Specialized Imaging SIMX framing camera, each with a 12-bit depth. The 12-bit depth was important for resolving fine grayscale levels, allowing for more precise detection of small refractive index gradients [15]. The camera bit depth, combined with the dynamic range, affects the ability to detect very small or very large density gradients simultaneously, especially in regions with both subtle and sharp features, such as a weak compression waves next to a conical shock front.

The schlieren setup used a linear configuration with two achromatic doublet lenses (focal length: 700 mm, diameter: 127 mm) as collimating optics. Optical components between the second collimating lens and the knife edge cutoff included a 640 nm bandpass filter, a neutral density filter to prevent sensor saturation, and, in some configurations, a beam splitter to route light to a second Nova-R5 camera.

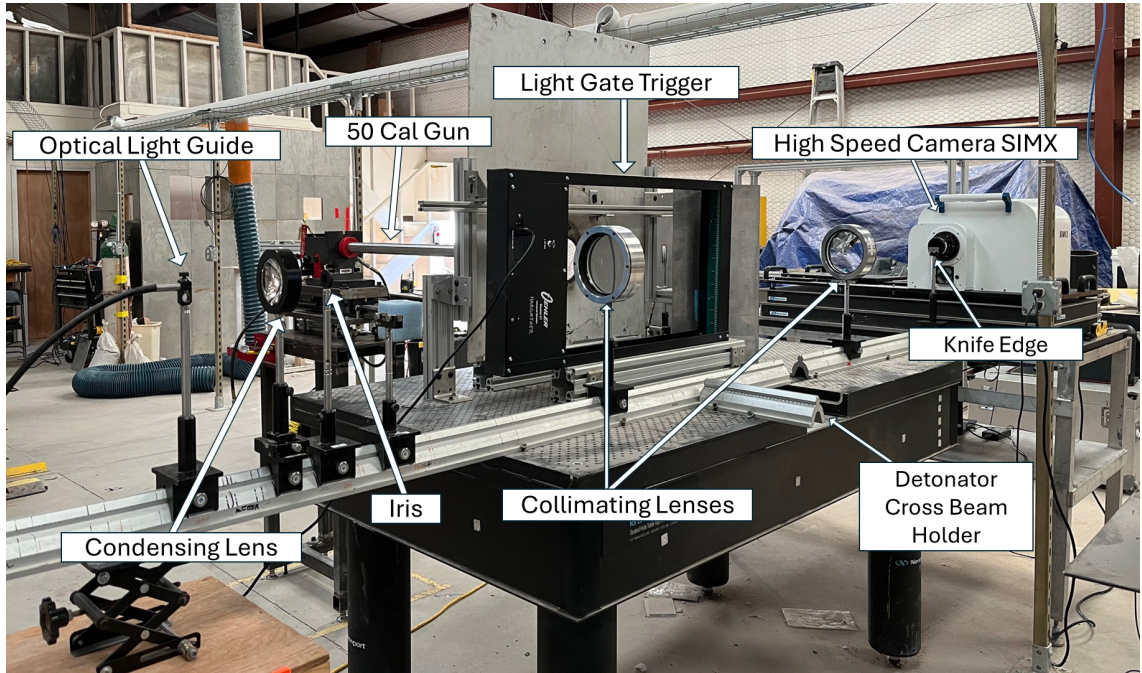


Figure 4.1: Typical quantitative schlieren set up. The SIMX camera for this test can be replaced with the Nova-R5s seen in Figure 4.2. A 3D printed detonator holder was mounted on the Detonator Cross Beam Holder as seen in Figure 4.3.

A Specialized Imaging SI-LUX 640 spoiled-coherence laser was used as the illumination source, operating in pulsed mode to define the exposure duration. Pulse widths ranged from 35 ns to 1 μ s, short enough to eliminate motion blur by ensuring that the exposure time was significantly less than the time required for the projectile to traverse a single pixel. Exposure times were selected based on the camera's resolution, the projectile velocity (ranging from 730 m/s to 900 m/s), and the physical scale per pixel. For the Nova-R5 camera, the shutter remained open for 0.8 ms while exposure was controlled by the laser pulse. Although the Nova-R5 supports a maximum frame rate of 1250 fps at full resolution, this mode proved unsuitable due to trigger timing limitations, which often led to missed shots or incorrect timing. Instead, full 9.4-megapixel resolution was preserved by capturing a single frame with precisely timed laser illumination. For the SIMX framing camera, the frame rate of the 15 frames were individually programmed with exposures ranging from 80 ns to 1 μ s depending on the speed of the projectile.

The schlieren setup included a horizontal knife-edge cut-off which covered approximately half of the light at the focal point. A horizontal cut-off was chosen because the vertical density gradient field was expected to be larger than the horizontal and thus a horizontal knife-edge cutoff would better visualize changes in the refractive index field. The horizontal knife edge orientation cuts off light that has been vertically deflected due to vertical refractive index gradients, resulting

in vertical grayscale intensity gradients in the image. The horizontal knife-edge was also aligned with the axis of symmetry used for the Abel inversion.

The primary limitations of a quantitative schlieren system are related to the light source's size and brightness, and the camera resolution. While higher-resolution cameras are the only way to mitigate the latter, the former was improved by implementing a condensing lens and iris into the schlieren system. The SI-LUX laser was used as the light source in conjunction with a 75-mm-diameter, 40-mm-focal-length aspheric condenser lens and adjustable circular iris. With these, the laser was focused to a circular point approximately 5 mm in diameter. A 640 nm bandpass filter with a 10 nm full-width at half-maximum was placed in front of the camera, ensuring that only a narrow band of wavelengths was recorded. This narrow spectral range largely eliminated chromatic aberrations in the optical system.

4.2 High resolution images of conical projectiles, explosively driven shocks, and intersecting shocks

Two Photron Nova R5-4K cameras simultaneously captured images with horizontal and vertical knife-edge cutoffs of the projectiles and explosively driven shocks. A beam splitter, positioned before the schlieren focal point, directed the light into separate paths, each leading to its respective knife edge and camera. A Specialized Imaging SILUX-640 nm spoiled coherence laser served as the light source, with a condensing lens and iris to reduce the size of the light source.

To maximize the cameras' resolution, a Specialized Imaging Single-Channel Delay Generator controlled the timing of the SILUX laser's pulses and the system exposure with a 35 ns pulse width. The camera shutters were left open, and the laser pulse controlled the exposure, ensuring high-resolution images without motion blur or timing errors. The Nova-R5's fastest frame rate at full resolution is 1250 fps. Still, at this rate, the trigger mechanism could not synchronize quickly enough, resulting in pre-triggering or delayed triggering, which caused the shock event to be missed. Exposure was controlled via the laser to resolve this, leaving the shutter open for its entire duration of 0.8 ms. This allowed the full 9.4-megapixel resolution to be maintained without needing high-speed triggering. A band-pass filter was placed before the beam splitter to eliminate wavelengths outside the 640 nm range originating from the explosive blast or muzzle flash. A tarp was draped over the cameras to help minimize ambient light interference from the room. Any other ambient light was removed in background subtraction.

As with all quantitative schlieren experiments, background and calibration lens images were recorded before the test.

A detonator mount positioned 25.4 cm outside of the schlieren lenses was added to the test set-up as seen in Figure 4.2. This placement ensured that the shock was well separated from the product gases. Because the composition of

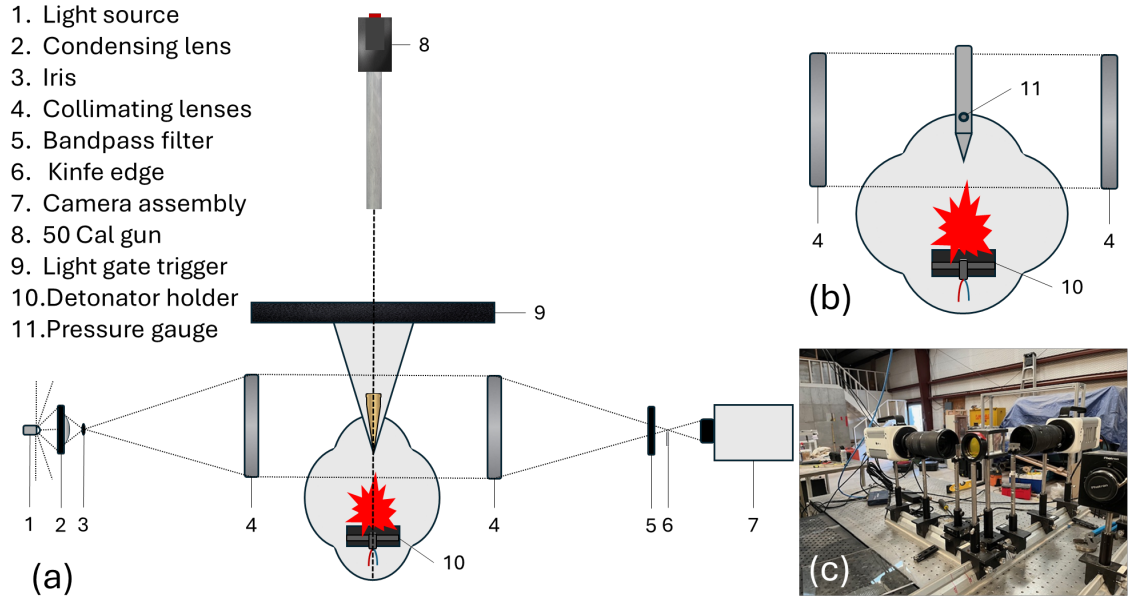


Figure 4.2: (a) Schematic of the schlieren setup. (b) Schlieren setup modified for pressure probe measurements. (c) Two Nova R5-4K cameras captured horizontal and vertical cutoffs for each image. Light from the schlieren system was split using a beam splitter, filtered by either a horizontal or vertical knife-edge cutoff, and then recorded by the cameras.

the explosive product gases differs from air, the Gladstone-Dale coefficient for air cannot be applied. All data here was extracted from images excluding regions containing the explosive product gases.

The detonators were placed directly in front of the gun barrel and mounted using expendable 3D-printed holders. A laser sight was used in the barrel to ensure the detonator was centered with the projectile and removed before loading the gun.

The detonators were RP-80 EBW detonators, fired using an FS-17 fire set. The detonation timing was controlled by a Stanford Research Systems Digital Delay Generator, capable of outputting a 32 V signal which initiated the FS-17. Delay times were refined iteratively based on observed shock arrival times at the center of the schlieren field of view.

4.3 Pressure probe measurements

Explosively driven shocks were imaged using quantitative schlieren to measure density. To validate these density measurements, a PCB piezoelectric pressure probe (340 kPa / 50 psi) was used as an independent measurement source.



Figure 4.3: 3D-printed Onyx detonator holder with the detonator positioned squarely in front of the gun.

The probe was positioned within the schlieren test section at distances of 21.59 cm, 24.13 cm, and 25.4 cm from the detonator. These distances were selected to capture data near the intersection of the explosively driven shock and the projectile.

The pressure probe triggered a Specialized Imaging SIMX framing camera as it sensed the pressure spike of the shock from the detonator blast. The camera recorded the shock on top of the sensor and 14 frames after. Multiple tests were performed at each location to determine the variability between detonators. The shock speed was determined by measuring the distance traveled between frames and dividing by the interframe time. This velocity was then used to calculate pressure and density ratios using compressible flow relationships. Combined with pressure probe data, these measurements provided peak shock pressures and characterized the pressure decay over time and distance.

The pressure probe was connected to an oscilloscope, which recorded the shock wave 10 μs before it reached the sensor and 96 μs after the initial shock front passed. This setup captured both the initial pressure spike and the subsequent relaxation. The oscilloscope was configured with a 200 mV/div sensitivity and a 10 $\mu\text{s}/\text{div}$ time base. The oscilloscope had a sample rate of 2.0×10^9 samples/second, resulting in a total data rate of 4.0×10^{14} samples/second for the 200,000 sample record length.

Figure 4.4 shows the locations where each pressure was measured relative to the detonator. Distance from the detonator to the center of the schlieren system was difficult to measure accurately and has a high degree of error.

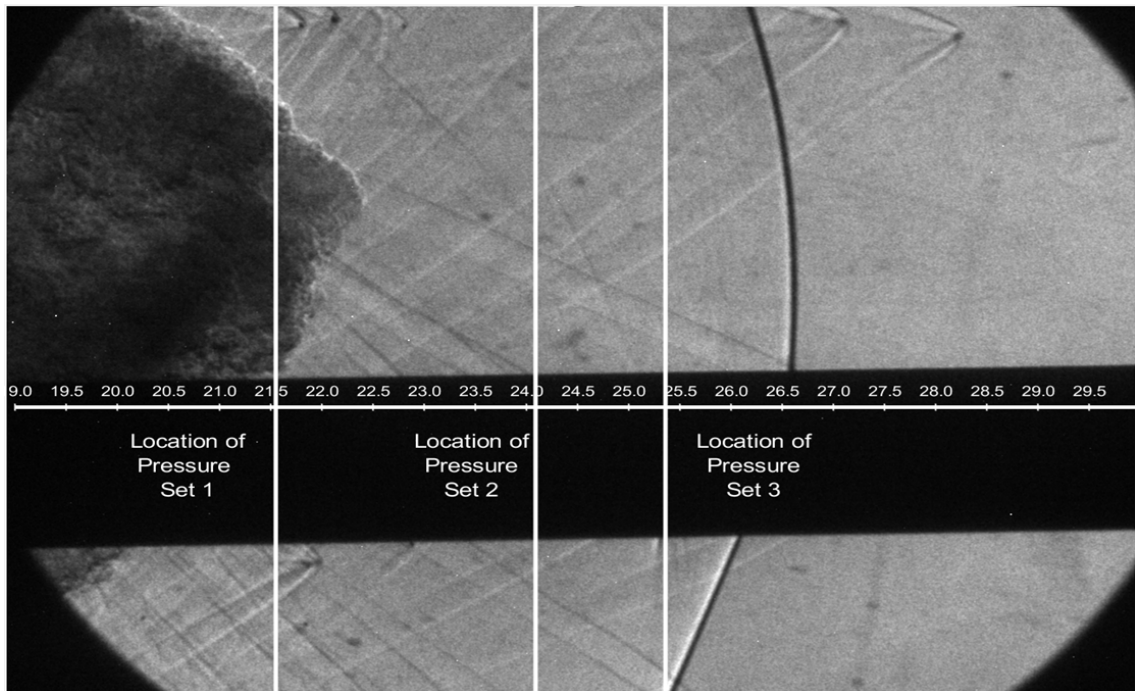


Figure 4.4: Shadowgraph image of the detonator shock showing the position of each pressure measurement. The center of the schlieren lenses is 25.4 cm (10 in) from the detonator holder. Scale bar shows the distance from where the detonator was set in cm.

CHAPTER 5

QUANTITATIVE SCHLIEREN DENSITY RECONSTRUCTION OF CONICAL PROJECTILE SHOCKS

Quantitative schlieren was applied to the shocks surrounding 10° half-angle cone projectiles ranging from Mach 2.09 to Mach 2.67. The Two-point Abel inversion method was found to best recreate the Taylor-Maccoll analytical shock solution out of the three Abel inversions attempted. A density field was successfully reconstructed for horizontal and vertical knife edges, bright and dark field analysis, and low resolution cameras. Four different sources of error were analyzed and deviations in background intensities was found to be the most prominent.

5.1 Determination of Mach Number from Projectile Images

Projectile velocities ranged between 750 and 900 m/s. Projectile Mach number M depends on both the projectile's velocity v and the ambient temperature T :

$$M = \frac{v}{\sqrt{\gamma RT}} \quad (5.1)$$

where γ is the ratio of specific heats and R is the specific gas constant, which are 1.4 and 287 J/(kg*K) for air, respectively. The SIMX framing camera captured fifteen images of each projectile at specific time intervals. The projectile's velocity was determined by measuring the distance traveled between frames, given the known time separation of the frame rate. Room temperature was recorded and used in Equation 5.1 to calculate the Mach number for each projectile.

The Mach number can also be determined from the shock wave angle for a known conical body. The angle of the shock wave cone is influenced by the Mach number, with higher Mach numbers corresponding to smaller angles, as illustrated in Figure 5.1. To account for any tilt, the shock angle was measured from the center-line of the projectile to the outer edge of the shock on both the top and bottom sides of the projectile and was used to estimate the projectile's speed using the conical shock relations outlined by Anderson [4, 31]. This shock-derived Mach number is compared to the Mach number calculated from the projectile's tracked positions in each visible frame, as shown in Table 5.1.

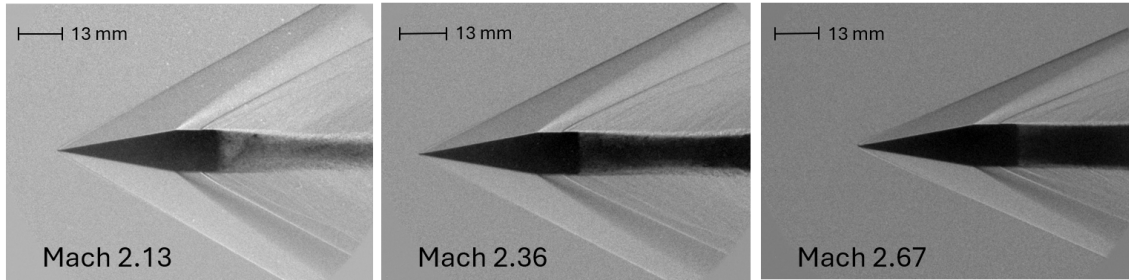


Figure 5.1: Three projectiles of varying speeds as noted on each image. The faster projectiles have a smaller shock wave angle.

Table 5.1: Comparison of The Different Methods for Calculating Projectile Velocity

IMR-7828 Propellant Mass	Shock Wave Angle $\pm 0.5^\circ$	Velocity from Shock Angle $\pm 13 \text{ m/s}$	Velocity $\pm 3 \text{ m/s}$	Mach ± 0.01
140 (grains)	29.4°	732 (m/s)	733 (m/s)	2.13
155 (grains)	26.6°	807 (m/s)	808 (m/s)	2.34
178 (grains)	23.8°	907 (m/s)	909 (m/s)	2.64

5.2 Density reconstruction from a high resolution image

To calculate the density in the flow field surrounding the projectile, a column of pixels is extracted, beginning at the centerline of the conical projectile, passing through the shock, and extending into the ambient atmosphere. The pixel intensities are converted to the light's refraction angle at each pixel using the best-fit line derived from the calibration lens, which relates pixel intensities to refraction angles based on the lens's focal length. An Abel inversion method is then applied to account for line-of-sight integration effects and calculate the index of refraction. The index of refraction is subsequently converted to density using Gladstone-Dale's Law. This process is repeated for each column of the shock cone, resulting in the complete density flow field shown in Figure 5.2. The Abel reconstruction is started from a distance of 200 pixels outside of the shock wave. Additional background shows low noise propagation through the desired flowfield and its surrounding areas. The ambient is observed in Figure 5.2 as the bright green color. The projectile was shot at an elevation of 1524 m, a temperature of 25.6° , 30 % humidity, and an atmospheric pressure of 85000 Pa.

A column of the flow field was isolated, and the density was plotted as a function of the distance from the surface of the cone. The location of the extracted column, positioned 3.3 cm from the tip of the conical projectile, is shown in Figure 5.4 as the red vertical line. The column was specifically chosen to be at the rear of the cone, where the resolution across the shock was greatest and the double shock structure from the slightly bent tip had fully merged. The two-point, three-point,

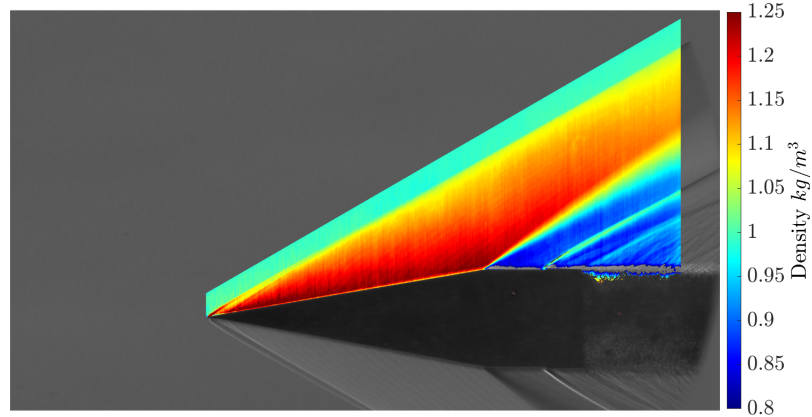


Figure 5.2: Density reconstruction of a projectile traveling at Mach 2.09, captured at a resolution of 2304x4096 pixels. The image was taken with a Phantom Nova R5-4k camera and corresponds with Figures 5.3, 5.4, 5.5, and 5.9

and ARAP Abel inversion methods were each used to analyze the data.

Figure 5.3 compares the density profiles obtained using the two-point, three-point, and ARAP Abel inversion methods, alongside the Taylor-Maccoll analytical solution (depicted in black). The Taylor-Maccoll profile was computed using the measured cone angle, shock angle, and Mach number [2, 3]. All Abel inversion methods reproduce nearly the same profile. This is expected if there are no sharp features for the three-point to smooth over [25, 37].

All Abel inversion methods show a dip in density at the surface of the cone before the profile rises to match the density predicted by the Taylor-Maccoll solution. This dip corresponds to a decrease in density and a subsequent rise in temperature near the cone's surface. This effect results from stagnation heating of the projectile and the growth of a boundary layer along its surface. The schlieren images clearly reveal the presence of this boundary layer, which here has been observed to increase the effective cone angle by approximately 0.67° . This increase in angle contributes to an overestimation of the shock angle and, if uncorrected, leads to an underestimation of the freestream Mach number in the Mach number by approximately 3% (Mach 0.06) here. This error is only present in the Taylor-Maccoll solution and not in quantitative schlieren. The identification of the boundary layer in schlieren imaging and its impact on flow properties is consistent with previous observations in high-speed flow diagnostics [14, 38].

The density profile shown in Figure 5.3 can be expected along nearly the entire length of the cone, assuming the camera resolution is sufficient. However, the tip of the cone behaves differently. A double shock phenomenon appears at the cone's tip, and the limited pixel resolution in this region is insufficient to accurately reconstruct the density field. This may be caused by slight damage to the projectile tip during launch which was observed in some of the testing. As a

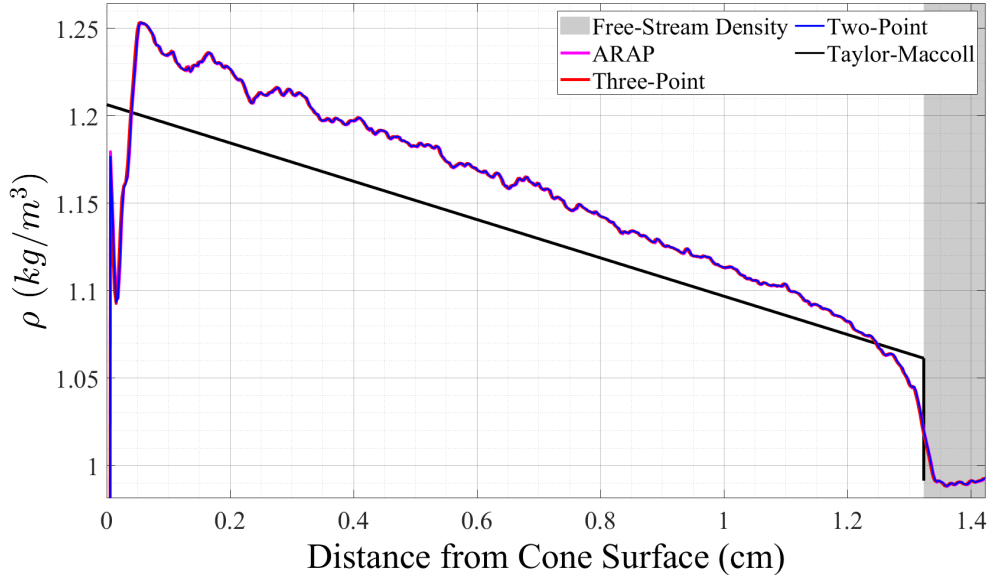


Figure 5.3: Air density starting from the surface of the cone, through the shock, and through to atmospheric air. Pixel data was extracted 3.3 cm from the tip of the projectile seen in Figure 5.4.

result, the tip of the cone is excluded from the following data analysis.

The regularly spaced Mach waves visible along the cone surface are attributed to machining marks. These generate small, periodic perturbations that produce weaker shock structures. While more prominent Mach lines appear as small rises along the line profile in the quantitative schlieren data, their overall impact on the Abel inversion is minimal.

To demonstrate the consistency of the density profile along the cone, columns were extracted from every column between the two solid white lines shown in Figure 5.4. Only the two-point Abel inversion method was used as it provides an accurate density calculations.

To analyze the reconstructed density field along the entire projectile, the radial distance from the cone is scaled by normalizing the local distance from the cone surface to the shock wave, using the angle of the shock wave for calculation. This scaling accounts for the shock's geometry. Figure 5.5 presents the density profile for pixel columns along the cone's surface as a function of this non-dimensionalized distance. In this scaled view, the Taylor-Maccoll solution is represented by a single line, as all points along the cone are assumed to converge to the same density, ignoring any boundary layer effects. The grayscale line profiles represent individual pixel columns. A gradient in shading visually indicates the variation in density along the projectile, with lighter shades corresponding to regions closer to the base, and darker shades representing areas near the tip of the projectile.

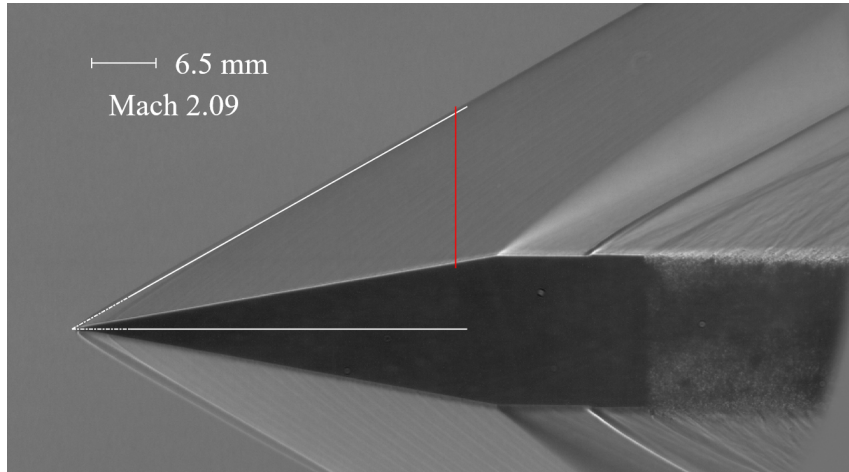


Figure 5.4: High-resolution image of a supersonic conical projectile. The red vertical line indicates the pixel column extracted to generate Figure 5.3. Columns extracted between the solid white lines are graphed in Figure 5.5. The dashed and solid horizontal lines represent the axis of rotation for each Abel inversion. This image was captured with a Photron Nova R5-4k.

Figure 5.5 demonstrates strong agreement between the density profiles from the middle and rear sections of the cone and the Taylor-Maccoll solution, confirming the reliability and repeatability of the quantitative schlieren method. Deviations observed in the profiles are attributed to errors, such as fluctuations in intensity relative to the background. In contrast, profiles closer to the tip of the projectile show the effects of the double shock phenomenon and the limitations imposed by low resolution.

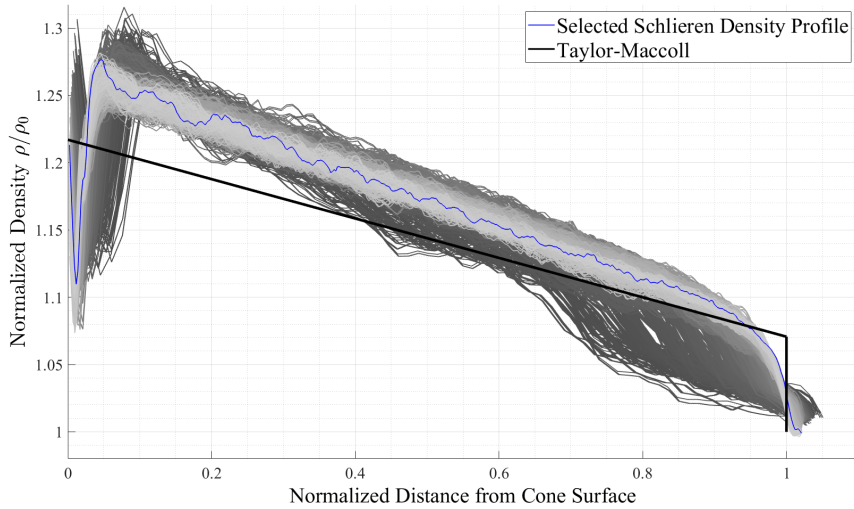


Figure 5.5: Density was calculated along the shock surrounding the cone. The distance from the cone surface was normalized relative to the shock radius for each analyzed column. The selected schlieren density profile, shown in blue, is the same profile displayed in Figure 5.3, extracted using the two-point Abel inversion at a distance of 3.3 cm from the tip of the cone. Darker gray lines are closer to the tip and lighter gray lines are closer to the base of the projectile.

5.3 Density of the conical shock under non-ideal conditions

Quantitative schlieren was used to analyze a conical projectile traveling at Mach 2.09. Two synchronous images were captured using horizontal and vertical knife edges. From these images, line profiles were extracted, starting from the cone's surface and extending through the shock. An additional profile was taken from the opposite side of the cone in the horizontal knife-edge image to show the density calculated from the bright field. Figure 5.6 presents the density maps obtained from all three methods, with the extracted profiles indicated by white lines. These density profiles are compared to the analytical Taylor-Maccoll solution in Figure 5.7 [2, 3].

Density measurements with a horizontal cutoff, as shown in Figure 5.6, more reliably capture the full density distribution and align with the Taylor-Maccoll solution across both dark and bright flow regions along the entire shock. In contrast, the vertical cutoff agrees well with the Taylor-Maccoll density in the rear of the cone but deviates progressively toward the tip. This is likely due to pixel resolution across the shock decreasing while approaching the tip. The refractive angle field of the vertical cutoff has a more limited range than that of the horizontal cutoff, making it more susceptible to error. With a clean image, effective background subtraction, and high resolution, vertical cutoff measurements of conical shocks can still be accurate, particularly in the cone's rear, as shown in

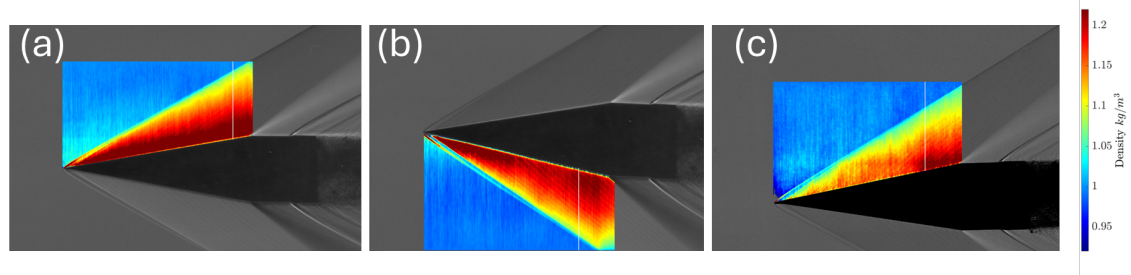


Figure 5.6: Quantitative schlieren density maps of the same projectile using three methods: (a) horizontal knife edge with the dark field, (b) horizontal knife edge with the bright field, and (c) vertical knife edge.

Figure 5.7. However, a horizontal knife edge is still preferred.

The bright and dark fields of the horizontal cutoff image should yield the same refractive angle field. However, there is a noticeable difference between the dark and bright quantitative schlieren density results. One consideration is the small bend on the projectile's tip creating a density differential under the cone and above it. This could have been caused due to mishandling the projectile before or during loading.

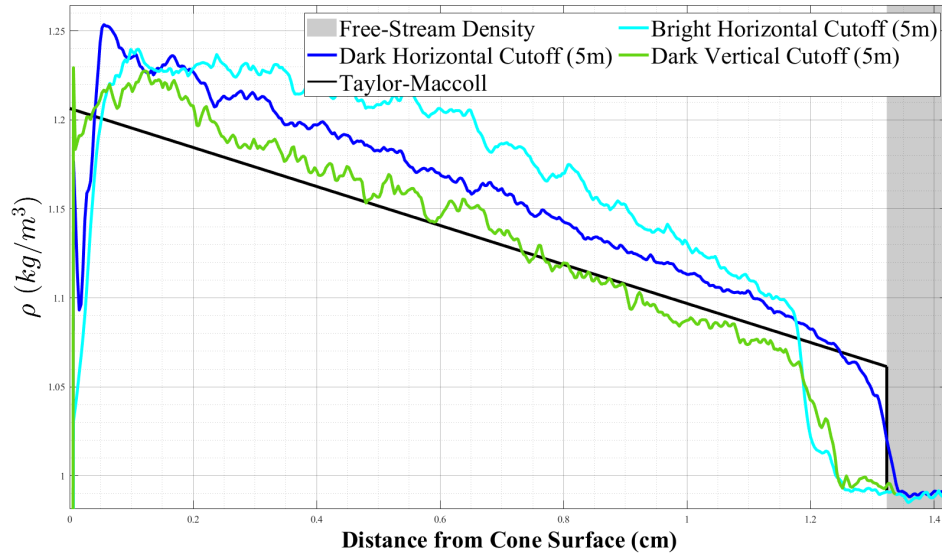


Figure 5.7: Comparison of quantitative schlieren using the dark and bright sides of a horizontal cutoff, a vertical cutoff, and the Taylor-Maccoll analytical solution. The calibration lens focal lengths used for each analysis are included in the legend.

5.4 Density reconstruction from a low resolution image

The Photron Nova R5-4k and Phantom VEO 990S cameras both offer high-speed, high-resolution images with 9.4 megapixels. These cameras allow for high-quality density reconstructions and accurate results in quantitative schlieren imaging, but have limited temporal resolutions. To investigate how quantitative schlieren performs with lower-resolution cameras, the SIMX framing camera, with a resolution of 1.2 megapixels, was used for comparison. In addition to its lower resolution, the SIMX camera introduces salt-and-pepper noise due to the sensor and gain settings. Density plots were generated for images captured with the SIMX camera, as shown in Figure 5.1. The resulting density reconstructions, presented in Figure 5.8, display a higher degree of deviation from the theoretical compared to those obtained with the higher-resolution cameras. Despite this, it remains possible to reconstruct the density across multiple Mach numbers, even with the increased noise and lower resolution.

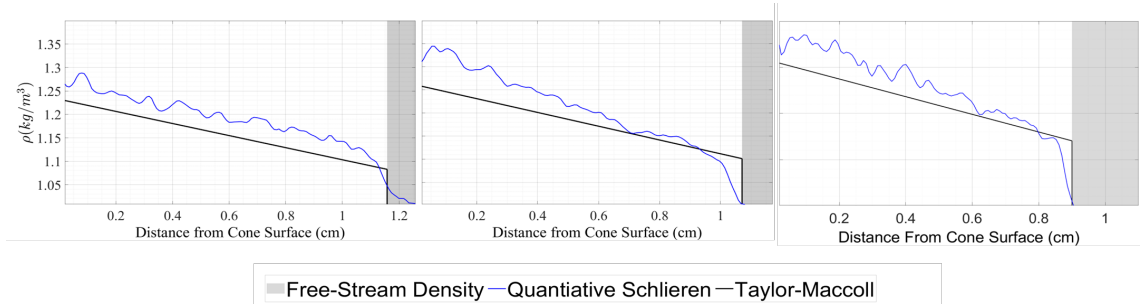


Figure 5.8: Density reconstruction for Mach 2.13, 2.36, and 2.67 projectiles, respectively, at a low resolution.

5.5 Uncertainty propagation of high resolution projectile images

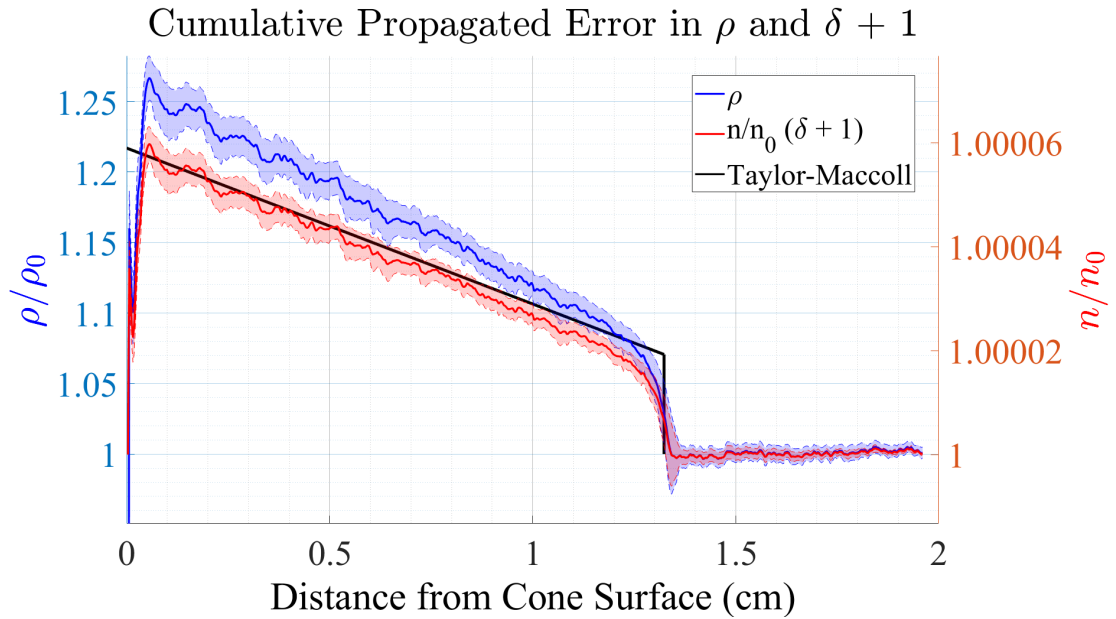


Figure 5.9: Full compilation of error propagation for the projectile image taken by the Photron Nova R5-4k. The bold lines represent the measured normalized density and the normalized index of refraction $\delta + 1$ along with one standard deviation error regions.

Error in the quantitative schlieren density measurements was estimated using the root-sum-square (RSS) method to propagate independent uncertainties through the analysis [39]. These uncertainties included deviations in pixel location, ambient pressure, ambient temperature, projectile tilt, and pixel intensity. Propagation of these uncertainties through the density reconstruction process produced the corresponding upper and lower bounds shown in Figure 5.9, rep-

representing one standard deviation. The independent contributions of each error source are illustrated separately in Figure 5.11.

Error in density is directly compared to the error in δ , the dimensionless quantity output from the Abel inversion, as shown in Figure 5.9. Up to the point of Abel inversion, the only relevant error sources are uncertainties in background intensity, projectile tilt, and the lens calibration process. This is because index of refraction is calculated from δ by multiplying by the atmospheric index of refraction, which is derived from density through the Gladstone-Dale law. Therefore, the final density field is influenced not only by background intensity and tilt errors, but also by uncertainties in ambient pressure and temperature measurements.

The primary source of error arises from variations in background intensity across the image, seen in Figure 5.10. Any deviation of a pixel, or group of local pixels, from the assumed background intensity causes a shift in the refractive angle. Factors such as misalignment of the knife edge with the focal point, dust on the lenses, and sensor noise contribute to these variations. These discrepancies introduce inaccuracies in the calculation of the refractive angle, which ultimately affects the reconstruction of the density. Large errors in background intensity are evident when the ambient density derived from quantitative schlieren deviates from the calculated ambient density based on measured temperature and pressure. Figure 5.11 demonstrates how a normalized intensity deviation of ± 0.003 (± 12 intensity values out of 4096 intensity levels for a 12 bit camera) alters the convergence of the quantitative schlieren ambient densities relative to the measured ambient density.

Projectile tilt introduces another significant source of error, particularly when measuring the shock angle. To ensure accuracy, the angle must be measured relative to the projectile's centerline rather than the image axes. In this study, all projectile tilts were measured as being less than $\pm 1.5^\circ$. To correct for tilt, the images were rotated so that the projectile's centerline aligned parallel with the image axis, reorienting the pixel columns to ensure they were perpendicular to the cone. Figure 5.4 shows the reorientation, while Figure 5.11 presents a comparison of the density profile taken from the original unrotated image and a rotated image. Error is shown for the rotated image profile based on a $\pm 0.3^\circ$ uncertainty for the cone's angle of tilt. In the experiments here the tilt is likely due to the camera being tilted relative to the projectile path, not the projectile actually traveling at an angle of attack. Note that these high resolution images were found to have sufficient resolution to allow image rotation of these small amounts without causing significant interpolation or averaging errors in the intensity field.

Uncertainty in an object's location within the image pixels, due to camera resolution, introduces spatial uncertainty. This includes challenges in accurately identifying the start of the projectile, the cone's centerline, the shock location, and calibrating pixel-to-length measurements. Higher camera resolution reduces these spatial uncertainties. Figure 5.11 shows how assuming different pixel locations would influence error.

Lastly, ambient pressure and temperature uncertainties further impact the

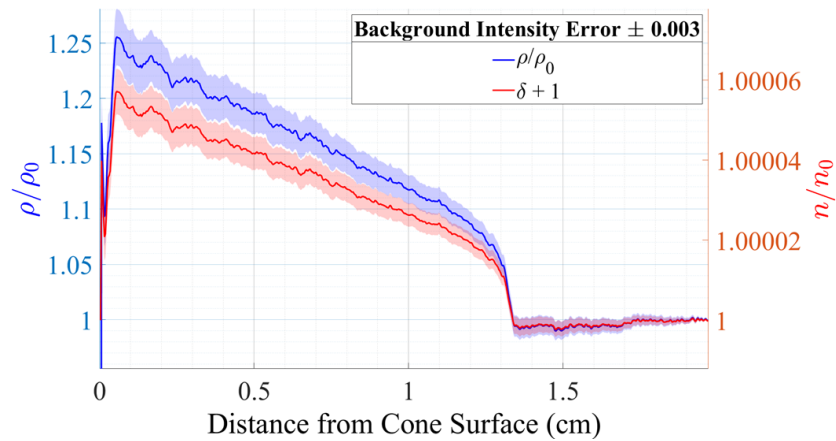


Figure 5.10: Intensity deviations from the background is the primary contributor to error.

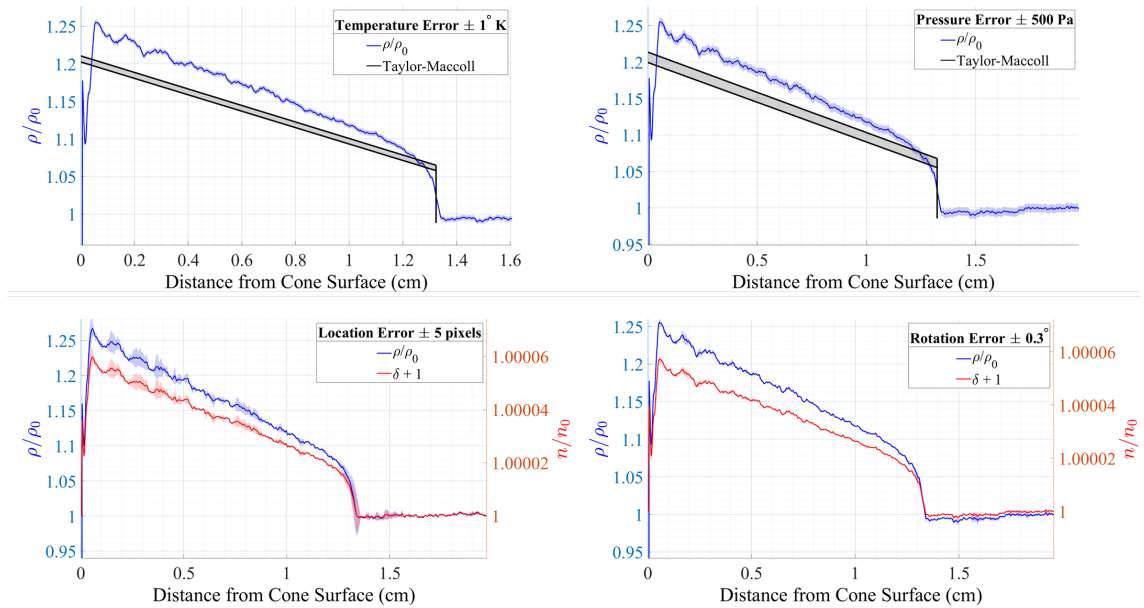


Figure 5.11: Breakdown of error contributions for projectile tilt, spacial uncertainty due to pixel location, and pressure and temperature.

analysis. Deviations in these measurements shift the entire density profile, as well as the Taylor-Maccoll analytical solution, uniformly upward or downward. Temperature and pressure were measured with a certainty of ± 1 K and ± 500 Pa respectively.

5.6 Discussion on Using Quantitative Schlieren to Measure Density Inside a Conical Shock

Quantitative schlieren proves to be an effective method for accurately measuring air density around axisymmetric supersonic conical projectiles, providing a non-intrusive way to capture the full flow field. Experimental measurements were compared to the theoretical density solution from Taylor and Maccoll, showing agreement to better than 5% across the entire flow field when reconstructed using the two-point Abel inversion. The primary source of error is attributed to variations in intensity relative to the background. The two-point Abel inversion method demonstrated its suitability for resolving conical shocks, applying minimal smoothing while accurately capturing density variations. The technique was successful in calculating density for supersonic projectiles ranging from Mach 2.09 to Mach 2.67. Based on these results, quantitative schlieren is suitable for use with supersonic projectiles. However, further studies are needed to assess its ability to reconstruct the density of more complex axisymmetric shock interactions to the same degree of accuracy. Asymmetric cases would likely require more advanced three-dimensional deconvolution techniques, such as Radon inversion or Fourier transform methods [18]. A complete tomographic reconstruction would also require multiple cameras capturing the flow from various angles.

CHAPTER 6

EXPERIMENTAL DENSITY RECONSTRUCTION OF EXPLOSIVELY DRIVEN SHOCKS

Quantitative schlieren was applied to an explosively driven shock. Simultaneous schlieren images were captured using horizontal and vertical knife edges. These results are compared to pressure data measured with a pressure probe and converted into density using compressible flow relationships. Both methods of quantitative schlieren reconstruction produced density profiles within the expected deviation of the pressure probe data.

6.1 Characterization of detonators using pressure probes

Three sets of measurements were taken at different distances from the detonator to assess the consistency of the detonators. Figure 6.1 shows the initial pressure measurements recorded from the pressure probes. The shock waves varied significantly, including differences in the distance between the shock front and the product gas cloud, the amount of fragmentation present in the shock, and the time required for the shock to reach the same location in different trials, as seen in Figure 6.2. A detonator is designed to be highly repeatable, but here there were variations in the shock's time of arrival, its shape, and the presence of shrapnel. More than likely, changes in the placement of the detonator in its holder, the detonator holder itself moving, and even differences in the holder's print material and density caused the differences from shot to shot. A more ideal shock might come from a spherical explosive charge with a less intrusive holder and repeatable distancing.

The 15 frames of the shock passing over the pressure sensor were recorded using the SIMX framing camera, which began recording as the shock first passed over the pressure probe sensor. By measuring the shock's displacement between frames, velocity and Mach number were calculated for each interval. However, the low resolution of the SIMX camera and uncertainty in pinpointing the shock's exact position within the pixels led to high errors in the calculated velocity and Mach numbers. To reduce this uncertainty, Mach numbers were averaged over the three nearest frames. Additionally, the Mach numbers were averaged across

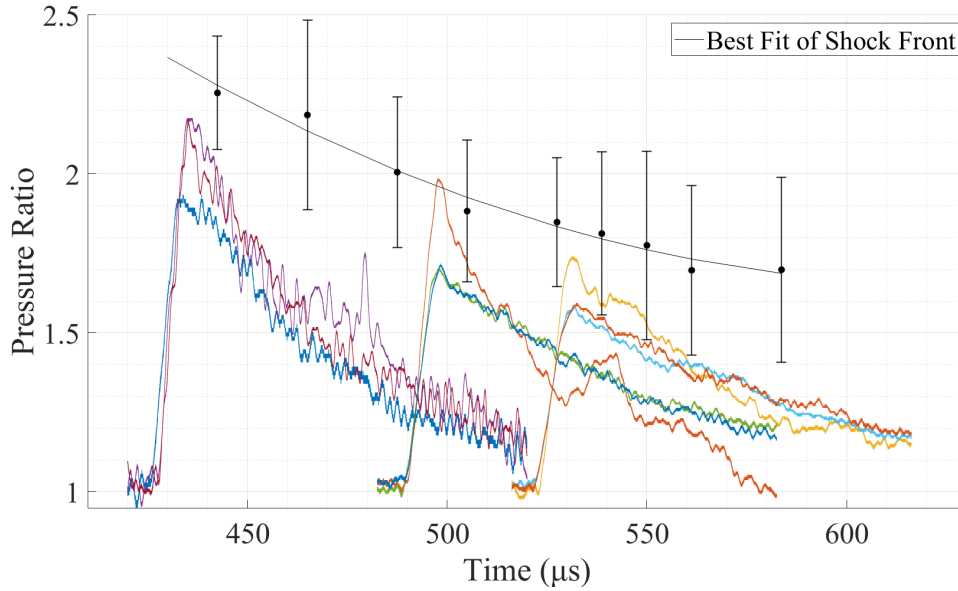


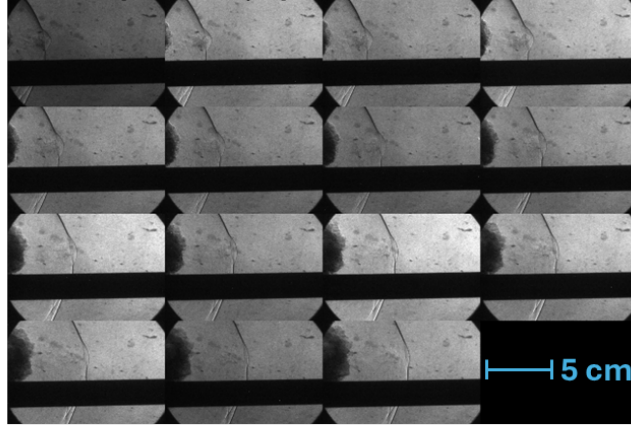
Figure 6.1: Three sets of pressure ratio measurements taken at three different locations in the schlieren lenses. Best fit of the shock front shows the decay of the shock front’s pressure ratio as it travels further from the detonator.

the three data sets. These values were then converted to pressure using the normal shock compressible flow equation 3.5 and plotted in Figure 6.1 as the uppermost data points, with a solid fitted line representing the trend.

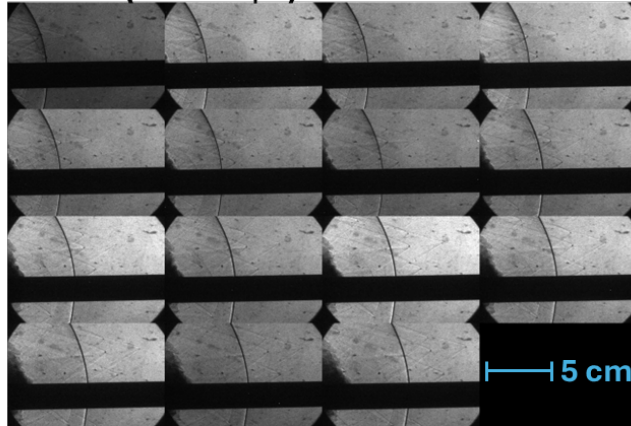
Figure 6.1 illustrates how pressure, and therefore density, decreases inside the shock as it passes over the pressure probe, as well as how the maximum shock front pressure diminishes with increasing distance from the detonation center [21]. The pressure values derived from camera measurements indicate the expected peak pressure at any given distance from the detonator blast. These values are notably higher than the peak pressures recorded by the pressure gauges. This discrepancy could be attributed to a systematic error, as the pressures measured by the gauges fall within the error margins of the camera measurement. Alternatively, the camera may be capturing the peak pressure more precisely than the pressure gauges, potentially due to lag in the response time of the gauges. Since the shock front is nearly instantaneous, the pressure gauge cannot sample quickly enough to capture such a rapid event.

Accurately measuring the distance between the schlieren lens center and the detonator was challenging due to the difficulty of maintaining a stable reference point during measurement. The detonator’s placement was fixed in position using a designated holder and alignment marks. The shock’s position in the schlieren images provided a reliable reference for correlating its location with pressure probe measurements. By identifying which of the 15 recorded frames the shock front appeared between, its approximate time of arrival within the

Set 1: ($t = 430 \mu\text{s}$)



Set 2: ($t = 492 \mu\text{s}$)



Set 3: ($t = 529 \mu\text{s}$)

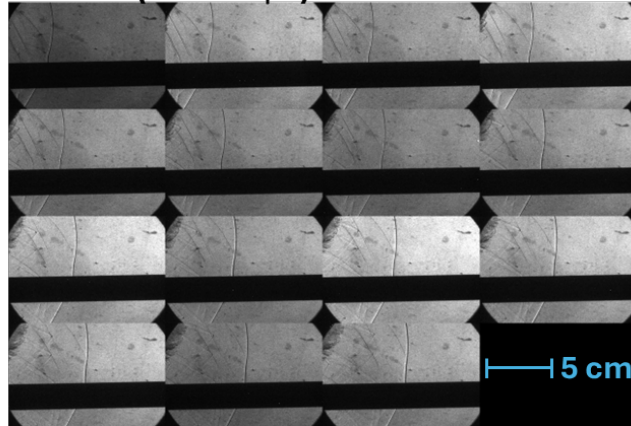


Figure 6.2: Three sets of images taken one after the other of the 15 frames captured using the SIMX Framing camera. Shocks vary despite detonators being placed in the same place for every test.

schlieren field of view could be estimated with reasonable accuracy, as illustrated in Figure 4.4.

The shock front and pressure ratios were converted to density ratios. The shock front Mach numbers measured directly from the images were converted to density ratio across the shock using the normal shock relationship for density (eq. 3.7). The pressure ratios were converted to density using the ideal gas law which was converted to a density ratio by dividing by the atmospheric density. A linear variation was used to assume temperature. The maximum temperature was computed two ways. The first method chose a mean Mach number from those calculated for the shock front and used the normal shock equation (eq. 3.6) to determine a temperature ratio. The second method took the maximum pressure recorded by the pressure probe, divided by atmospheric pressure to get a pressure ratio, and used normal shock equations 3.5 and 3.6 to determine a temperature ratio. Each temperature ratio was multiplied by atmospheric temperature to find the maximum temperature across the shock. A temperature was linearly assigned to each data point ranging from the maximum temperature at the shock down to atmospheric temperature where the pressure/density profile is first at atmospheric conditions again. Data points preceding the shock were calculated using atmospheric density. A comparison of the two methods shows very little difference in the resulting density ratios, as seen in Figure 6.3.

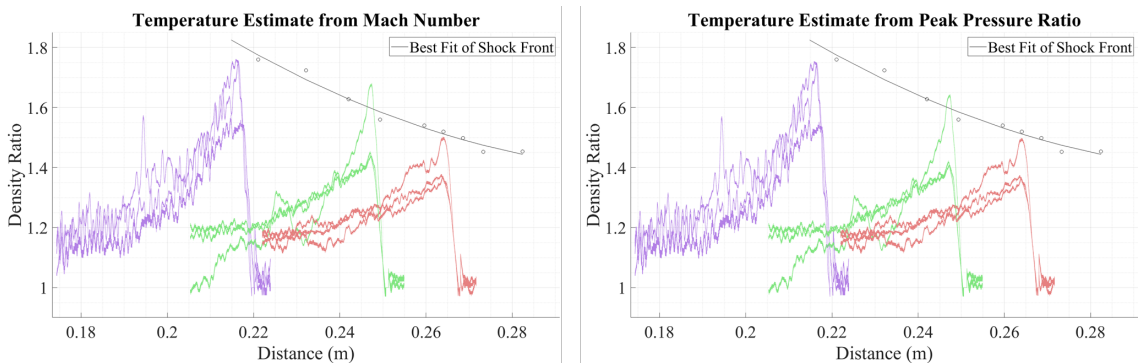


Figure 6.3: The difference between the density when using the Mach number from the inter-frame velocity or the pressure ratio from the PCB probe to compute an assumed temperature is negligible.

Figure 6.1 shows the pressure as a function of time. However, quantitative schlieren gives density as a snapshot of time and a function of distance. In Figure 6.3, the time axis was converted into a distance axis by multiplying the measured inter-frame velocity to show the distance from the detonator's origin. The density profiles were then flipped about their maximum density ratio.

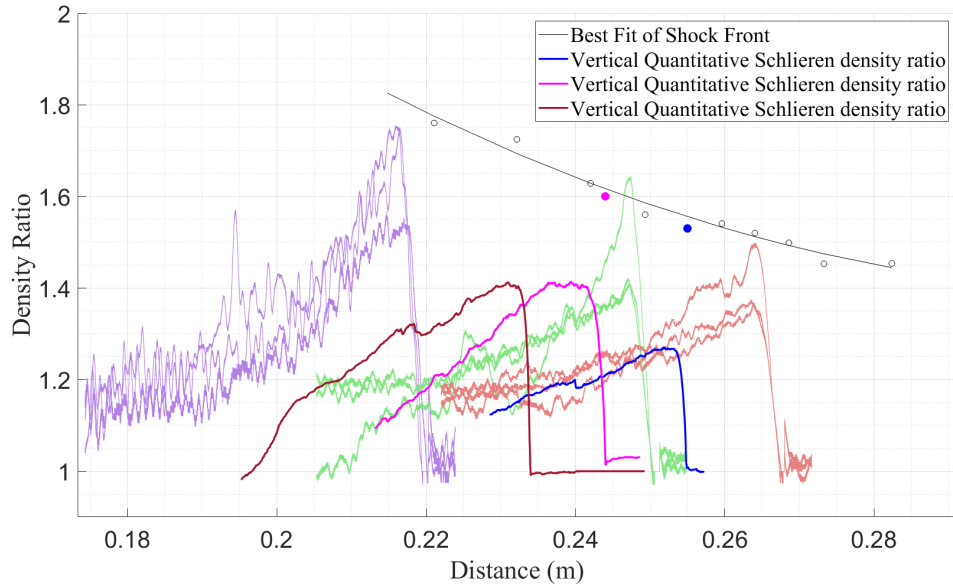


Figure 6.4: Three quantitative schlieren measurements are overlaid onto the density plot in Figure 6.3, using the inter-frame Mach number to estimate temperature. The solid lines represent quantitative schlieren data obtained with a vertical knife edge. The peak densities from two corresponding horizontal knife edge schlieren measurements are shown as points.

6.2 Quantitative schlieren analysis of explosively driven shocks

As with the conical projectiles, both horizontal and vertical knife-edge cutoffs were used to capture synchronous images of the explosively driven shock. The images obtained with the horizontal knife-edge cutoff were analyzed using a horizontal axis of rotation, while the vertical knife-edge schlieren images were analyzed using a vertical axis of rotation. The quantitative schlieren results were then compared to the densities obtained from the pressure probe data. The vertical cutoff schlieren and pressure probe data, which were taken along the same path, are both plotted in Figure 6.4. The maximum density from the horizontal cutoff quantitative schlieren, synchronized with two of the vertical cutoff schlieren profiles, is provided as points, with colors corresponding to their vertical matches. The third horizontal schlieren maximum density ratio is not included. Despite being measurements of the same shock, there is a large difference in the peak vertical and horizontal quantitative schlieren density ratios. However, both fall within the expected deviation from the detonators. Future work should investigate the cause of this discrepancy between the two schlieren methods and determine which one more accurately reflects the true density of the detonator.

Additional pixels were added to the vertical cutoff image to simulate the

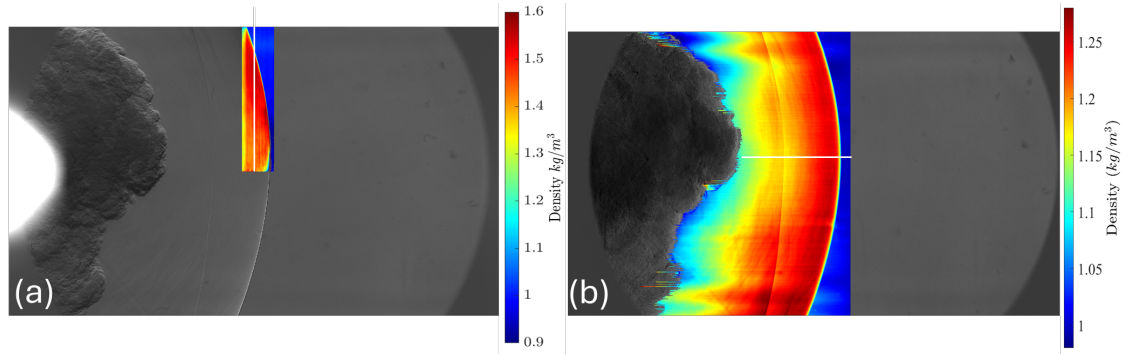


Figure 6.5: Quantitative schlieren of an explosively driven shock: (a) Density map using a horizontal knife-edge cutoff, (b) density map using a vertical knife-edge cutoff

distance between the camera frame edge and the location of the detonator as required for the Abel analysis. For the vertical cutoff case, the Abel inversion was performed using an axis of rotation positioned at the detonator's original location, 24.1 cm from the detonator. The density is underestimated compared to what would be expected from the probe density. This could be due to the Abel inversion smoothing the peak of the shock. Another possibility is that the explosively driven shock from the detonator is not spherical enough to assume axisymmetry over the entire volume. The PETN cylinders exploding in [40] exhibit this asymmetry as the shock assumes a multi-lobed shape, which closely resembles the shock pattern produced by the RP-80 detonators. To mitigate these, a different tomographic technique would be valuable in future work. A way to mitigate the effects while still using Abel inversion would be to measure the local geometric figures in the image to estimate a more precise location for the origin and axis of rotation.

Figure 6.6 presents a comparison of density maps obtained from both horizontal and vertical quantitative schlieren orientations. A white line is overlaid on each density map in Figure 6.5 to indicate the locations where line profiles were extracted. The density profiles originate from the axis of rotation taken at the center of the blast, follow the designated white lines, and extend into the ambient atmosphere. For the vertical cutoff, only values beyond the explosive product gas are included in the density profile.

The density measured using the horizontal knife edge overestimate the density ratio compared to the probe's density measurement. In the horizontal density map, the axis of rotation limits the regions available for analysis, as proper reconstruction requires imaging both the shock front and a portion of the surrounding ambient air. Since the Abel inversion integrates data from the outermost pixel inward, meaningful density reconstructions can only be obtained in columns that extend into the atmosphere, as seen in Figure 6.6. The right most part of the shock in the figure is also cutoff. This is due to the limited intensity range and resolution compared to the rest of the image as the pixels extracted are only the shock

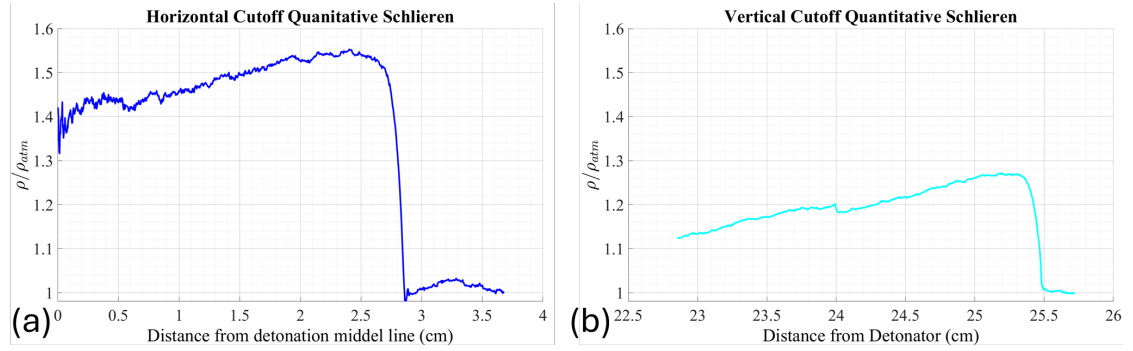


Figure 6.6: (a) density profile along the white line from the horizontal cutoff image, and (b) density profile along the white line from the vertical cutoff image. In (b), the vertical axis.

front. Another limitation of the horizontal cutoff is the artificial density spike at the centerline, caused by the unbounded nature of the axis of rotation. This artifact results from the inversion process, which relies on preceding pixel data to compute density values accurately. Without a well-defined boundary, the inversion introduces errors at the centerline, affecting the final density reconstruction.

The density measured using a vertical cutoff is compared to the density measured with a horizontal cutoff. A column of densities was extracted from the vertical cutoff image at the same place as a line profile quantitative schlieren was extracted from the horizontal cutoff image. This allowed for the most direct comparison between the two without cutting off parts of the shock due to insufficient resolution in the horizontal image and allow a direct comparison. The comparison is shown in Figure 6.7.

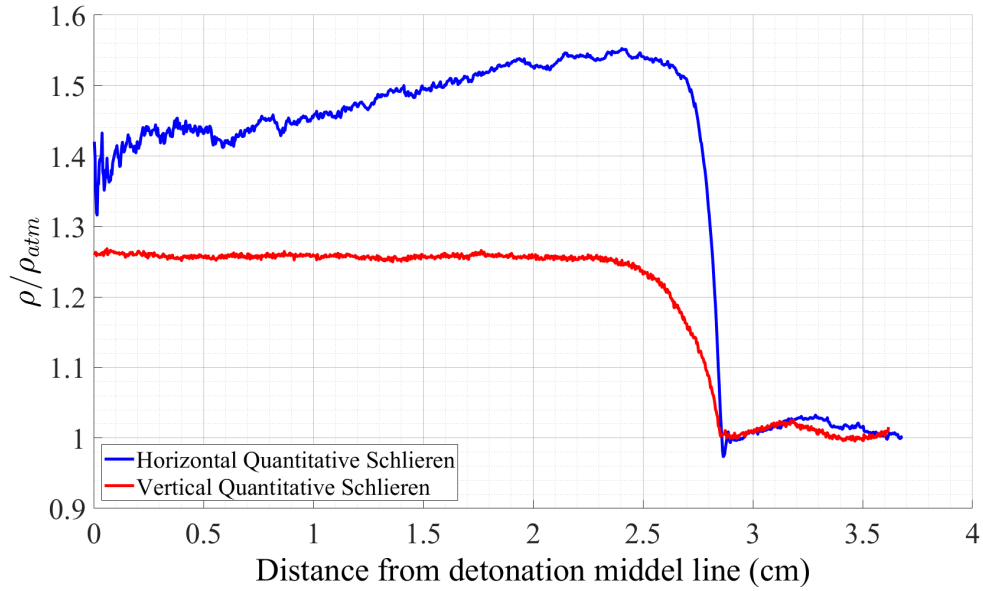


Figure 6.7: Comparison of two quantitative schlieren density profiles: one with a vertical cutoff and one with a horizontal cutoff.

6.2.1 Lens distortion

Error in quantitative schlieren usually comes from deviations in individual pixel intensities due to dust on the lenses, ambient light from the room, and sensor noise. These problems are solved with a background subtraction. Outside of errors associated with intensities, pressure, and temperature measurements, there is a spatial discretization error.

The shock, while theoretically only a few molecules thick, spreads across multiple pixels in the image due to the refractive index change across it. Even if it were only inside one pixel, it is uncertain where in that pixel the shock actually is. This is why when measuring the distance a shock travels between pictures there is such a large error, as seen in Figure 6.1.

This measurement was performed to ensure accurate measurements throughout the field of view by accounting for lens distortion, specifically by determining the distance from the local geometric axis of symmetry for the shock's arc in the case of the vertical cutoff detonators. Quantitative schlieren assumes that the lenses do not distort the image or alter the curvature of the shock. To quantify the extent of lens distortion, a uniform grid was placed in the schlieren test section, and the full lens distortion was mapped. Figure 6.8 illustrates the lens distortion across the schlieren field of view.

Figure 6.8 visualizes how much each point in the mesh moves relative to where the point should be in the case of no distortion. It's worth noting the camera used here is a Photron Nova S12 which has a lower resolution than the Nova

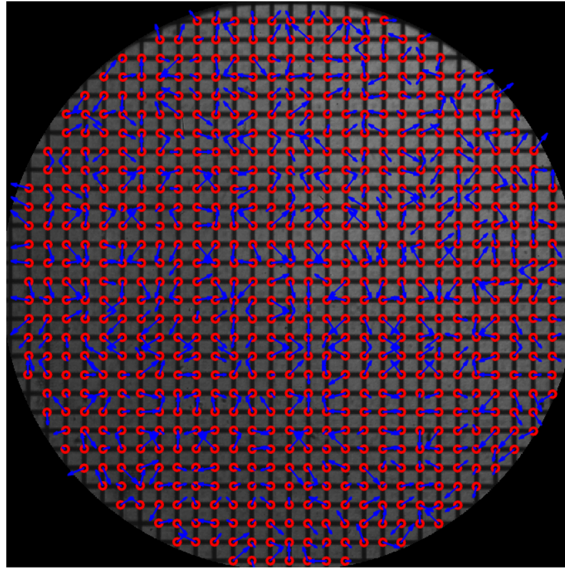


Figure 6.8: Vectors showing how each point in the mesh shifts relative to the location the point would be without distortion.

R5. Because of this, some of the smaller distortions are lost. At most, distortions in the lens shift points by two pixel diagonally and one pixel laterally. There is no noticeable trend that shows the lens distorting more in one part of the lens than any other. A histogram shows what frequency determined pixels shift in Figure 6.9.

For large measurements in the lens, such as measuring the arc length of the explosively driven shock, the error from lens distortion is the same as the error expected from measuring the distance in a lens. Error from lens distortion will lower or raise the peak density of the explosively driven shock of only about 0.25 % or 0.002 kg/m^3 .

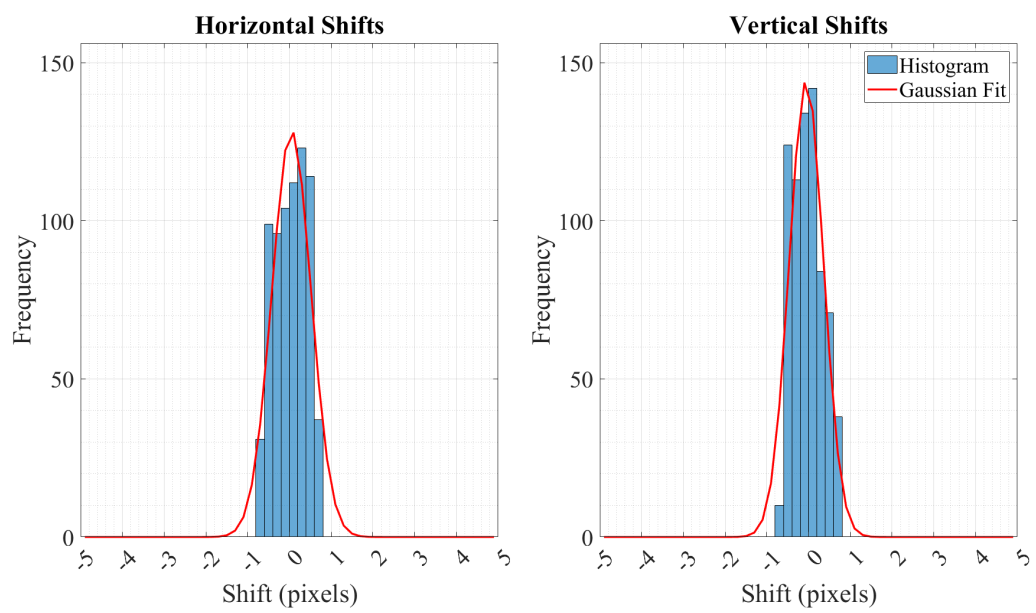


Figure 6.9: Histogram showing the frequency horizontal and vertical pixels are distorted and to what magnitude.

CHAPTER 7

QUANTITATIVE SCHLIEREN DENSITY RECONSTRUCTION OF INTERACTING CONICAL AND EXPLOSIVELY DRIVEN SHOCKS

When the conical projectile intersects the explosively driven shock from the detonator, it creates multiple interacting shock regions. These regions include: (a) atmosphere, (b) the shock formed as air transitions from the atmosphere to the conical projectile's shock, (c) the shock created as air moves from the atmosphere across the explosively driven shock, (d) the interaction between the conical shock and the explosively driven shock, and (e) a reflected shock off the cone's surface. Figure 7.1 illustrates these interactions. Density fields are analyzed using compressible flow relationships for each of these regions.

7.1 Quantitative schlieren of intersecting shocks

Both horizontal and vertical knife edge cutoff images of the event were taken simultaneously, which are shown in Figure 7.3. Quantitative schlieren was applied to the horizontal cutoff's quantitative schlieren and the resulting density maps are shown in Figure 7.4.

The projectile limits the axis of rotation about its axis for both the horizontal and vertical knife edges. For the vertical cutoff, the refractive angle field is misaligned with the axis of rotation of the explosively driven shock. This may be the cause as to why there are sections of the refractive angle field that do not correctly represent the expected flow patterns, the density reconstruction to be greatly overestimated in the vertical case, density is not a jump discontinuity. There may be other reasons as to why the density in the vertical case is not reconstructed properly. In contrast, the horizontal knife edge cutoff's axis of rotation around the center of the projectile is well suited as the light refracts in the same direction. Figure 7.4 compares the resulting density fields of the two knife edge cutoffs using quantitative schlieren.

A line profile was taken from the cone surface through region a, which is atmosphere of the image of the horizontal knife edge cutoff and plotted in Figure 7.5. The extracted profile is along the white line in Figure 7.4. Here, the measured quantitative schlieren was compared against compressible shock relationships.

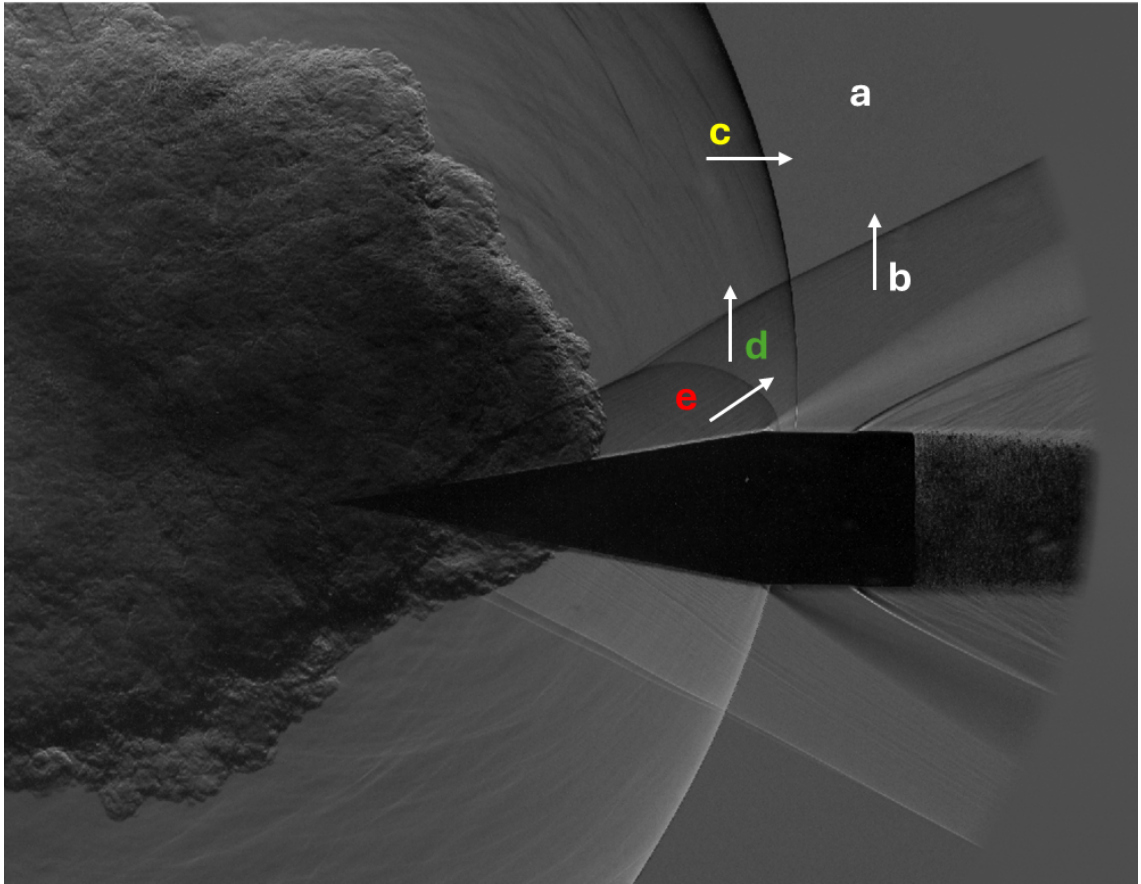


Figure 7.1: Shock features formed from the intersecting shocks: (a) atmosphere, (b) conical shock from atmosphere, (c) explosively driven shock (d) conical shock from the explosively driven shock, (e) reflection shock off the conical projectile

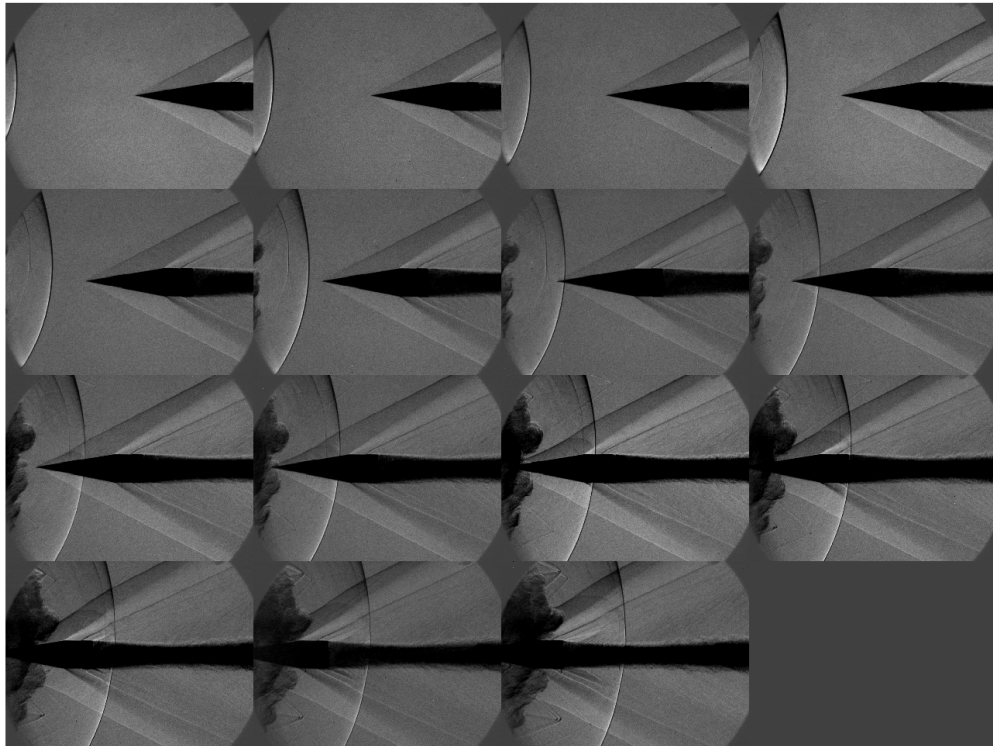


Figure 7.2: Progression of the shocks intersecting over 15 frames taken with the SIMX framing camera.

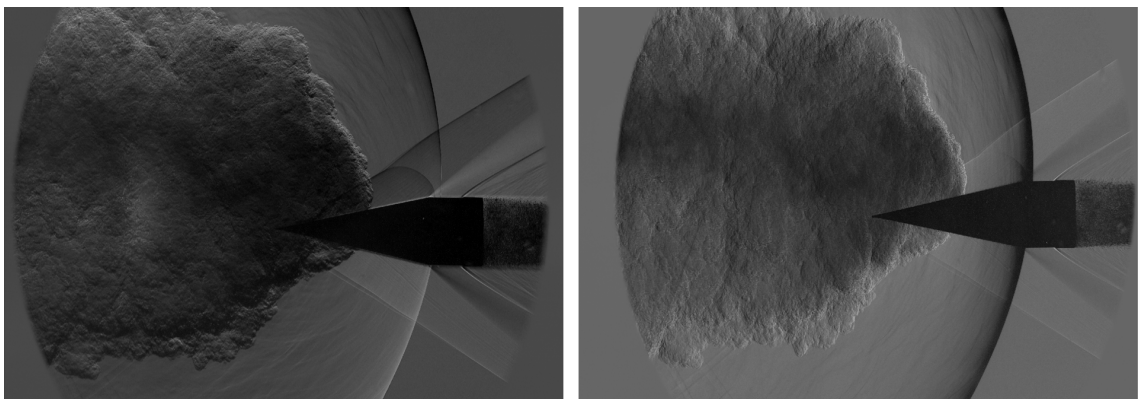


Figure 7.3: Projectile flying through an explosively driven shock. (a) horizontal cutoff schlieren image and (b) vertical cutoff schlieren image

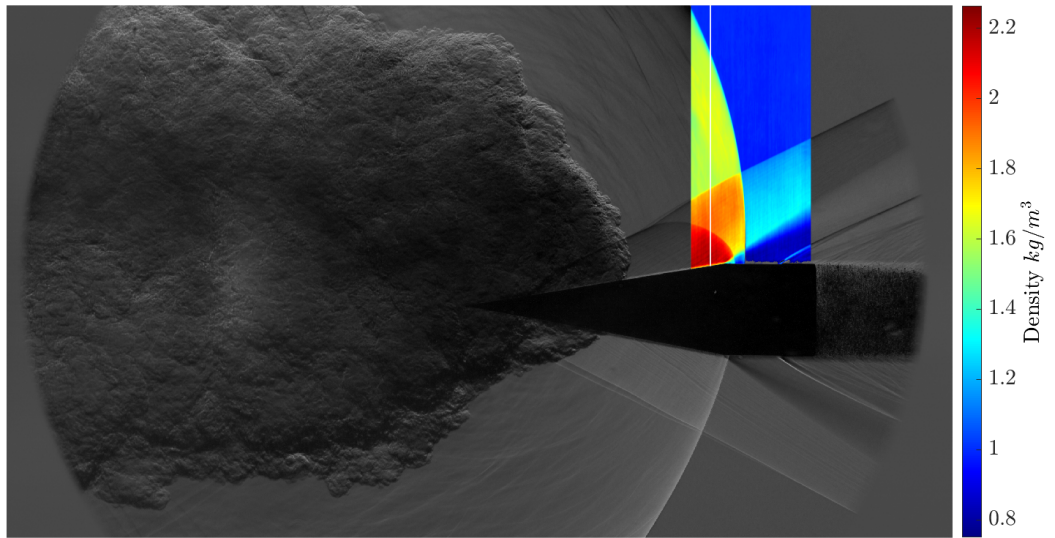


Figure 7.4: Quantitative schlieren density map using a horizontal knife edge cut-off.

The reflection and explosively driven shocks are shown as lines while the conical overlap shock is shown as a region where the bottom of the region is the expected density across the shock and the top is the expected density at the cone's surface.

Calculating the full density field of the intersecting shocks, whether analytically or using the experimental approach, presents significant challenges due to the complex variation of density throughout the entire flow field. In the case of the conical projectile, density varies radially from the conical projectile, but is constant along the rays of the projectile [2, 3]. The density profile of the explosively driven shock decreases radially from the center of the charge and can be measured experimentally using a pressure probe. By assuming that this radial density distribution remains consistent at all positions, the entire flow field can be estimated. However, in the case of overlapping shocks, the interaction between these shocks creates a highly dynamic flow field, where each point is influenced by the combined effects of the conical shock, the explosively driven shock, and the reflection shock and is a unique solution for each point.

Rather than calculate an exact solution, the density was estimated using Taylor-Maccoll's solution, oblique shock relationships, and normal shock relationships. Regions b and d in Figure 7.1 are both conical shocks and can be analytically solved using the Taylor-Maccoll solution. The shock wave angle was measured directly from the image for both regions to find the Mach number and density ratios. Region c needs normal shock relationships to solve. The reflection shock in region e was solved using oblique and normal shock relationships.

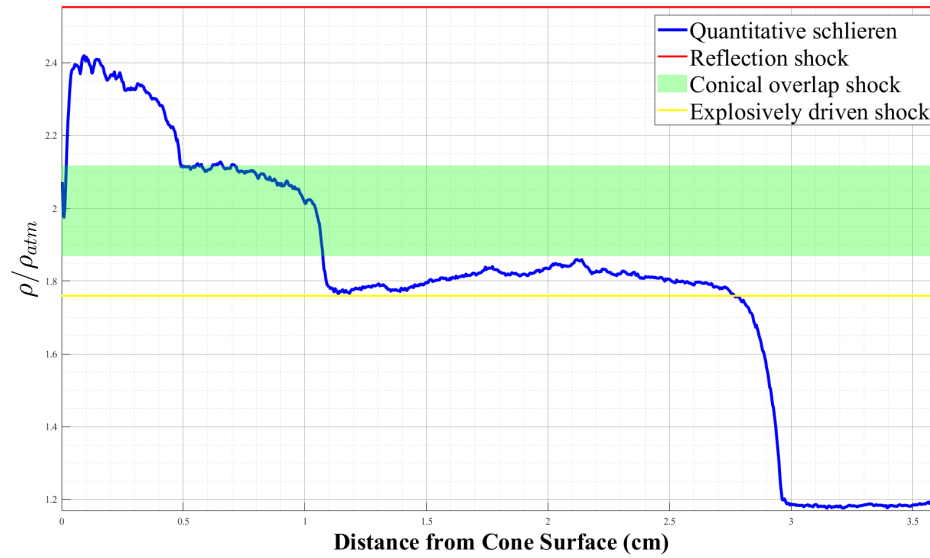


Figure 7.5: Density measured with quantitative schlieren compared to compressible shock relationships.

Region (a) is the first region to analyze, or in this case measure. Atmospheric pressure and temperature were both measured right before the shot. Atmospheric density was then calculated through the ideal gas law (eq. 3.8).

Region (b) requires the Taylor-Maccoll analytical solution. To solve the Taylor-Maccoll, a turn angle and wave angle are needed. The turn angle (δ) is the half-angle of the cone, in this case 10° . The wave angle (β_b) can be measured directly from the image. The full Taylor-Maccoll solution cannot be applied all the way to the cone surface because a boundary layer exists and which can be observed in the images. The Mach number can be determined iteratively from these two values along with the density ratio. To get the density across the shock, it's the density ratio multiplied by the atmospheric density.

Region (c) is the explosively driven shock which is solved using normal shock relationships. The location of the explosively driven shock was analyzed in this image and matched to a Mach number based on it's position in the schlieren lenses. The half-way point in the schlieren lenses is about 25.4 cm from the detonator. Any additional distance between the shock and the center of the lenses can be calculated using a known length to pixel conversion. The Mach number in these images is estimated to be 1.28.

Once the Mach number is known, the density ratio can be determined using a normal shock relationship (eq. 3.7). Like the density in region (b), the density across the shock is found by multiplying atmospheric density to the ratio.

Region (d) is another conical flow that steps across the shock from the com-

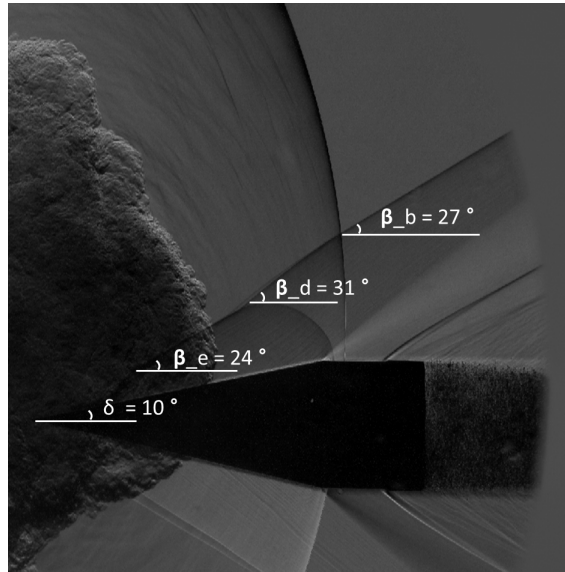


Figure 7.6: Angles can be measured for sections of the flow.

pressed air of the explosively driven shock in region (c). This is unlike regions (b) and (c) which started from atmosphere. The shocked air from the detonator changes the temperature, pressure, and Mach number of this overlapping region. The Taylor-Maccoll solution can be applied here exactly as it was in region (b) to measure the shock angle (β_2) and calculate the density ratio at the shock. Here, the ratio is multiplied by the density just outside of the shock, in this case the density of region (c). Density relaxes the further away it is from the shock front it is. Here, that relaxation is neglected and the density across the explosively driven shock was used. The compressed air of region (d) is conical flow and it will increase in density the closer to the cone's surface is being analyzed. Figure 7.5 shows the density increasing for this region as a green band which marks the density across the shock to the density at the cone's surface. It's important to note that this region of flow does not make it up to the cones surface and therefore it would not reach the maximum density for this region at the top of the green band.

Lastly is region (e) which is a reflection shock. It is unknown if here it can be approximated as conical flow. Instead oblique and normal shock relationships will be used to find the density. Starting from the explosively driven region, and use the position in the schlieren lenses is used to estimate the local density. The estimated density ratio in region (c) is 1.2 which is converted to density by multiplying by atmospheric density. The shock wave angle (β_3) is measured and plugged into the θ - β - M relationship (eq. 3.2) with the wave angle to iteratively find the Mach number. Once found, the flow Mach number must be reoriented to the flow using eq. 3.9. Once the normal Mach component of the flow is found, it can be plugged into the normal shock equations to determine the density ratio and multiplied by the estimated density of region (c). Using β_3 instead in the Taylor-Maccoll would underestimate the density by 30 %.

CHAPTER 8

CONCLUSION AND RECOMMENDATION ON FUTURE WORK

8.1 Conclusion

Quantitative schlieren proves to be an effective method for accurately measuring air density around axisymmetric supersonic conical projectiles, providing a non-intrusive way to capture the full flow field. Quantitative schlieren successfully measured the density fields of conical shocks using both horizontal and vertical knife-edge cutoffs in bright and dark field configurations. Experimental measurements were compared to the theoretical density solution from Taylor and Maccoll, showing agreement to better than 5 % across the entire flow field when reconstructed using the two-point Abel inversion. The primary source of error is attributed to variations in intensity relative to the background. All three Abel inversion methods demonstrate their suitability for resolving conical shocks, applying minimal smoothing while accurately capturing density variations. The technique was successful in calculating density for supersonic projectiles ranging from Mach 2.09 to Mach 2.67. Based on these results, quantitative schlieren is suitable for use with supersonic projectiles.

The measured densities of an explosively driven shock from a detonator varied depending on the measurement method used. The vertical quantitative schlieren reproduced the same profile as the pressure probe measurements. However, both the horizontal and vertical quantitative schlieren produced peak densities that differed significantly, though both were within the expected range of variation for detonator-driven shocks. The intersecting shocks generated by a conical projectile and an explosively driven shock could only be analyzed using a horizontal knife-edge cutoff, which is comparable to the peak density calculated from compressible flow relationships.

8.2 Recommendations for future work

Future work should explore alternative tomographic reconstruction techniques for quantitative schlieren to improve the resolution of complex shock interactions. Asymmetric cases, in particular, would likely require more advanced

three-dimensional deconvolution techniques, such as Radon inversion or Fourier transform methods [18]. A complete tomographic reconstruction would also necessitate multiple cameras capturing the flow from various angles.

Additional measurement methods may be required to better capture the full density increase across the shock front. Furthermore, quantitative schlieren should be systematically compared to other flow measurement techniques to further assess its accuracy and limitations in high-speed flow environments.

Computational fluid dynamics (CFD) simulations should be compared to the experimental results in regions where overlapping shock waves are observed. Additionally, further investigation is needed to interpret qualitative schlieren images obtained using horizontal versus vertical knife-edge orientations.

REFERENCES

- [1] Jason Michael Falls. High-speed quantitative schlieren measurement of density fields around conical supersonic projectiles. Master's thesis, New Mexico Institute of Mining and Technology, 2022.
- [2] Geoffrey Ingram Taylor and J. W. Maccoll. The air pressure on a cone moving at high speeds. *Proceedings of the Royal Society of London. Series A, Containing Papers of a Mathematical and Physical Character*, 139(838):278–297, 1933.
- [3] J. W. Maccoll. The conical shock wave formed by a cone moving at a high speed. *Proceedings of the Royal Society of London. Series A - Mathematical and Physical Sciences*, 159(898):459–472, 1937.
- [4] Jr. Anderson, John D. *Modern Compressible Flow With Historical Perspective*. McGraw-Hill Higher Education, New York, USA, 2020.
- [5] T B Fisher, M K Quinn, and K L Smith. An experimental sensitivity comparison of the schlieren and background-oriented schlieren techniques applied to hypersonic flow. *Measurement Science and Technology*, 30(6):065202, 2019.
- [6] Fulvio Scarano Christian J. Kähler Steve T. Wereley Jürgen Kompenhans Markus Raffel, Christian E. Willert. *Particle Image Velocimetry: A Practical Guide*. Springer, New York, USA, 3rd edition, 2018.
- [7] Steve T. Wereley Jürgen Kompenhans Markus Raffel, Christian E. Willert. *Particle Image Velocimetry*. Springer Berlin, Heidelberg, New York, USA, 2007.
- [8] Paul W. Cooper. *Explosives Engineering*. Wiley-VCH, New York, USA, 1996.
- [9] Gilbert Ford Kinney and Kenneth Judson Graham. *Explosive Shocks in Air*. Springer Berlin, Heidelberg, New York, USA, 2 edition, 1985. Originally published by Macmillan Publishers, 1962.
- [10] R. J. Goldstein, editor. *Fluid Mechanics Measurements*. Taylor & Francis, New York, USA, 2nd edition, 1996.
- [11] David Estruch, Nicholas J. Lawson, and Kevin P. Garry. Application of optical measurement techniques to supersonic and hypersonic aerospace flows. *Journal of Aerospace Engineering*, 22(4):383–395, 2009.

- [12] Scott A. Berry, Scott Nowlin, Daniel S. Thompson, and Brian R. Hollis. Non-intrusive measurement techniques for flow characterization of hypersonic wind tunnels. Technical Report NASA/TM-2019-220312, NASA Langley Research Center, 2019.
- [13] Dana Dabiri and Charles Pecora. *Particle Tracking Velocimetry*. IOP Publishing, New York, USA, 2019.
- [14] G. S. Settles. *Schlieren and shadowgraph techniques: Visualizing phenomena in transparent media*. Springer-Verlag, New York, USA, 2001.
- [15] Michael J. Hargather and Gary S. Settles. A comparison of three quantitative schlieren techniques. *Optics and Lasers in Engineering*, 50(1):8–17, January 2012.
- [16] Gary S Settles and Michael J Hargather. A review of recent developments in schlieren and shadowgraph techniques. *Measurement Science and Technology*, 28(4):042001, February 2017.
- [17] Per Christian Hansen, Jakob Sauer Jørgensen, and William R. B. Lionheart, editors. *Computed Tomography: Algorithms, Insight, and Just Enough Theory*. Society for Industrial and Applied Mathematics, New York, USA, 2021.
- [18] Masanori Ota, Kenta Hamada, Ryusuke Noda, Hiroko Kato, and Kazuo Maeno. Three-dimensional ct measurement of supersonic flow field around an asymmetric body by background oriented schlieren (BOS) technique. *Journal of the Japan Society for Aeronautical and Space Sciences*, 59(689):154–159, 2011.
- [19] D. Raparia. The algebraic reconstruction technique (art) applied to tomography in fluid flows. *Review of Scientific Instruments*, 63(4):2340–2347, 1992.
- [20] Bernd R. Noack. *Proper Orthogonal Decomposition: Theory and Reduced-Order Modelling*. Springer Vieweg, New York, USA, 2015.
- [21] Jesse D. Tobin and Michael J. Hargather. Quantitative schlieren measurement of explosively-driven shock wave density, temperature, and pressure profiles. *Propellants, Explosives, Pyrotechnics*, 41(6):1050–1059, 2016.
- [22] Cameron J. Dasch. One-dimensional tomography: a comparison of Abel, onion-peeling, and filtered backprojection methods. *Applied Optics*, 31(8):1146, 1992.
- [23] Sigurdur Helgason. The Abel, Fourier and Radon transforms on symmetric spaces. *Indagationes Mathematicae*, 16(3):531–551, 2005.
- [24] S. Dash, M. H. Heidmann, and J. H. Miller. Application of abel inversion techniques to supersonic flow fields. *AIAA Journal*, 31(10):1801–1808, 1993.
- [25] Samuel Grauer and Timothy Sipkens. New transform to project axisymmetric deflection fields along arbitrary rays. *Optics Letters*, 46(24):6077–6080, 2021.

- [26] Pankaj S. Kolhe and Ajay K. Agrawal. Abel inversion of deflectometric data: comparison of accuracy and noise propagation of existing techniques. *Applied Optics*, 48(20):3894, 2009.
- [27] Frédéric Champagnat, Aurélien Plyer, Olivier Léon, Philippe Cornic, David Donjat, and François Nicolas. Abel inversion from central-projection background oriented schlieren observations for reconstruction of axisymmetric refractive media. *Applied Optics*, 64(2):350, January 2025.
- [28] Bryan E. Schmidt, Wayne E. Page, and Jeffrey A. Sutton. On the application of the abel transformation in statistically axisymmetric turbulent flows. *AIAA Journal*, 60(4):2169–2177, 2022.
- [29] J. D. Tobin. Quantitative schlieren measurement of explosively-driven shock wave density, temperature, and pressure profiles. Ms thesis, New Mexico Institute of Mining and Technology, 2014.
- [30] R. Buchanan, D. L. Frost, and A. J. Higgins. On the symmetry of shock waves from detonators. *Shock Waves*, 30(6):617–631, 2020.
- [31] Ames Research Staff. Equations, tables, and charts for compressible flow. Technical Report 1135, National Advisory Committee for Aeronautics, 1953.
- [32] Julian H. Allen and A. J. Eggers. A study of the motion and aerodynamic heating of missiles entering the earth’s atmosphere at high supersonic speeds. Technical Report NACA TN 907, National Advisory Committee for Aeronautics (NACA), 1944.
- [33] Ascher H. Shapiro. *The Dynamics and Thermodynamics of Compressible Fluid Flow*. The Ronald Press Company, New York, USA, 1953.
- [34] William J. Devenport. Aoe 3114 aerodynamics: Calculator page, n.d. <https://devenport.aoe.vt.edu/aoe3114/calc.html>.
- [35] NASA Glenn Research Center. Normal shock relations, 2024. <https://www.grc.nasa.gov/www/k-12/airplane/normal.html>.
- [36] Hans W. Liepmann and Anatol Roshko. *Elements of Gasdynamics*. John Wiley & Sons, New York, USA, 1957.
- [37] Daniel D. Hickstein, Stephen T. Gibson, Roman Yurchak, Dhruvajyoti D. Das, and Mikhail Ryazanov. A direct comparison of high-speed methods for the numerical Abel transform. *Review of Scientific Instruments*, 90(6), 2019.
- [38] Ponnampalam Balakumar and Lewis Owens. Stability of hypersonic boundary layers on a cone at an angle of attack. In *48th AIAA Aerospace Sciences Meeting Including the New Horizons Forum and Aerospace Exposition*, 2010.
- [39] John R. Taylor. *An Introduction to Error Analysis: The Study of Uncertainties in Physical Measurements*. University Science Books, Sausalito, CA, 2nd edition, 1997.

- [40] Michael J. Hargather and Gary S. Settles. Optical measurement and scaling of blasts from gram-range explosive charges. *Shock Waves*, 17(4):215–223, 2007.

APPENDIX A

1ST APP TITLE

A.1 Appendix A: Conical projectile and detonator test plan



1001 South Road • Socorro • NM • 87801 • telephone: 575.835.5312 • facsimile: 575.835.5630 • www.emrtc.nmt.edu

EMRTC - Committed to Excellence in the Fields of Energetic Materials Research, Testing and Training since 1947.

TEST PLAN

TP-23-C-37

High Velocity Conical Projectile Testing for Optical Density Characterization using Universal Receiver and Commercial Barrels

New Mexico Tech Mech. Eng.
Dr. Michael Hargather
Michael.Hargather@nmt.edu

Author: Jessica Cooke
(505)- 500-7532

Fund: MQOS15

Revised: March 18, 2024

1. Purpose:

The Shock and Gas Dynamics Laboratory (SGDL) is studying the density variation around ballistically launched projectiles of varying geometries. The purpose of the testing described here is to visualize and perform quantitative measurements using schlieren photography for density variation characterization. Some experiments will investigate the shock shock interactions between the shock of the projectile interacting with the shock produced from a detonator.

2. Test Overview/ Summary:

High velocity ballistic experiments will be performed using projectiles of various sizes, shape, and composition. The projectiles will be launched into a sand catch. High speed schlieren imaging will leverage the Specialized Imaging SI-LUX 640 spoiled coherence laser illumination source. The launching of the projectiles will be performed using SGDL's universal receiver (UR) and various powder gun barrels located at the Ballistics Sciences Laboratory (BSL). A cut-down 50 BMG brass cartridge will be used to hold the powder charge and percussion primer when using 50, 55, 65, and 75 caliber systems. Other commercial cases will be used where appropriate. Commercial smokeless powders will be used for these powder charges. The IBHVG2 program will be used for predicting gun performance before a powder load is utilized to ensure developed gas pressure remains within the gun system, projectile, and sabot design specifications. The maximum allowable breech pressure for the 50 BMG barrel is 65 ksi, the expected breech pressure from IBHVG2 must be lower than this value. Testing at the BSL and operation of the gun system will be in accordance with the procedures in this document (attachment 5 and 6 respectively). In experiments with a detonator being used in combinations with the conical projectiles, attachment 9 (procedure for use of RP-80 detonators with Conical Projectiles) procedures and protocols will be followed.

3. Location of Testing

- All testing will be conducted at the Torres Ballistic Science Laboratory (BSL).
- Projectile fabrication will be performed offsite at the SGDL research lab L4 (EMRTC chemistry lab) and/or at the NMT machine shop.

4. Sequence of Steps**4.1 General**

The SGDL will launch conical projectiles of various lengths, diameters, geometries, and compositions. Where applicable, projectiles will be held in 3D printed or machined sabots and launched at velocities up to 2km/s. These projectiles and sabots will be prepared by the SGDL. The number of shots will vary as dictated by the research requirements of the SGDL. The type of testing and instrumentation will vary as dictated by the research requirements. Set up and tear down of the experimental setup will be the responsibility of SGDL personnel.

4.2 Required Personnel and Training

- Operation of the SGDL's universal receiver (UR) gun system requires a minimum of two personnel (Gun Operator and Safety).
- Ordnance personnel are required for operations involving RP-80 detonators
- SGDL personnel may fill the role of Test Engineer, Gun Operator, and/or Safety.
- At least one EMRTC employee or Dr. Michael Hargather must be present during gun operation as either the Test Engineer, Gun Operator, or Safety. The present EMRTC employee must be either an Ordnance Gunner, Engineer 1, or higher.
- Personnel Limits – A maximum of five essential personnel may be present in the fire booth during testing, but personnel should be limited.
- All non-essential personnel will be located in the Visitors and Instrumentation Observation Loft during operation of the gun system unless prior approval has been granted by the Safety Office.
- SGDL students may be certified to operate the gun system as the Gun Operator. These personnel will have completed the SGDL Gun Operator Training program to certify them for operation of the SGDL gun system. This training program is designed to ensure that personnel are trained and certified by satisfactorily demonstrating the ability to safely perform all required tasks involving the operations of powder guns at the BSL.

4.3 Test Preparation

- For instrumentation, high-speed optical imaging systems supplied by the SGDL will be deployed for all tests. These optical systems may or may not use laser illumination. These imaging systems will generally be placed perpendicular to the trajectory of the specimen and positioned to look at the projectiles inflight and/or impact of specimens with engineering controls in place to protect against specimen/fragment impingement on the equipment. Placement of instrumentation will be directed by the Test Engineer or appropriate SGDL representative prior to testing.
- For all tests, a projectile stop will be in place down range to restrict potential projectile/fragment fly out. For open air testing, the primary projectile stop is installed down range of the powder gun system at the north end of the BSL building. This stop is a steel box, constructed from ½" A36 steel plate with an AR500 ½" steel plate installed at the rear, that is nominally 24" high by 24" wide by 36" deep, and filled with dry sand. The stop may contain a solid fill of dry sand or a minimum of three layers of sandbags stacked three sandbags high. The primary stop will be no more than 5 meters (15 feet) from the muzzle of the UR gun to minimize the possibility of a projectile missing the stop due to vertical or horizontal drift during flight. This projectile stop will be inspected after every shot to verify that the steel box is undamaged and determine if any sandbags that no longer hold their shape or are freely leaking sand need to be replaced.
- The IBHVG2 program will be used for predicting gun performance for a specific projectile before a powder load is utilized to ensure developed gas pressure remains within the gun system and sabot design specifications. A cut-down 50 BMG brass cartridge will be used to hold the powder charge and percussion primer. Commercial smokeless powders will be used for these powder charges.

4.4 Pre-test Checkouts

Checkouts to be performed prior to testing are detailed in Gun Start of Day (attachment 5) and Operational Procedures (attachment 6) attached at the end of this document.

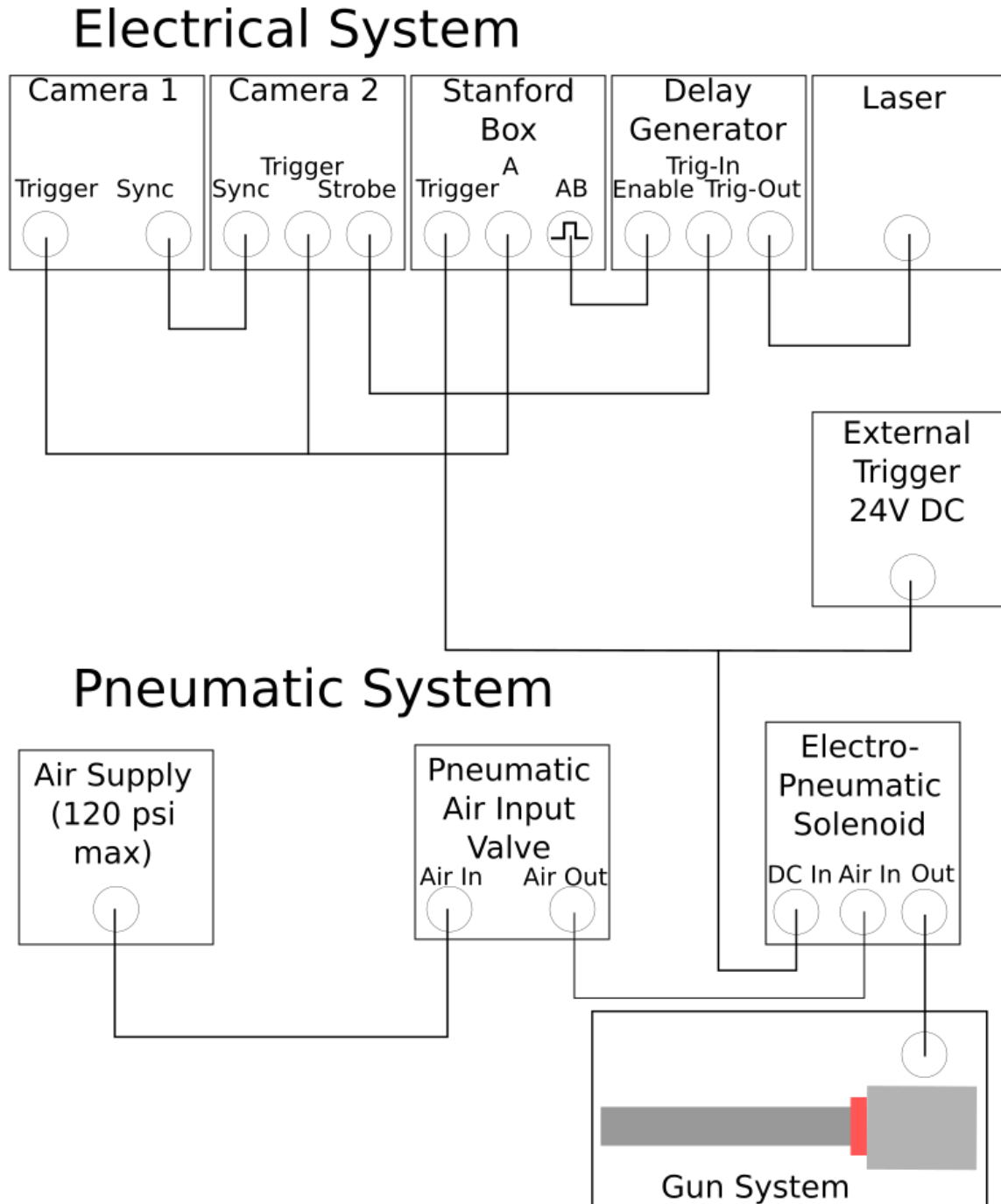
4.5 Testing

- Testing will encompass a variety of conical projectiles at varied velocities.
- Velocity of specimens, specimen composition and geometry, use of RP-80 detonators, and instrumentation will vary as dictated by the research requirements but will remain in the scope described in this test plan.
- Testing at the BSL and operation of the gun system will be in accordance with the Gun Start of Day (attachment 5) and Operational Procedures (attachment 6) attached at the end of this document.

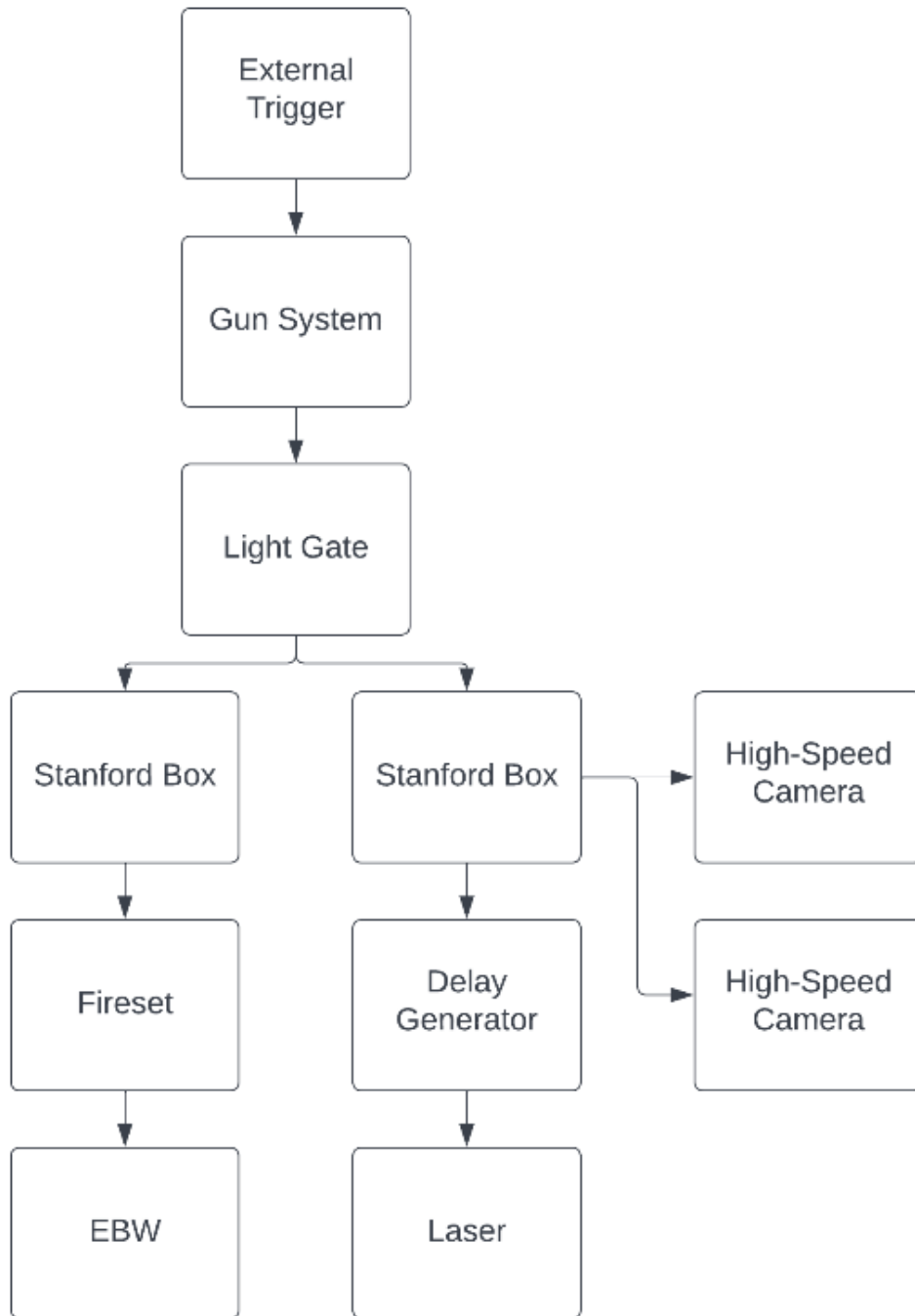
5. Test Matrix

The SGDL will launch a variety of conical projectiles over the duration of this work. The number of shots, launch velocity, and testing type will vary as dictated by the research requirements of the SGDL. A test matrix will be submitted to the Safety Office and on file at the BSL prior to the start of each day of testing. A test matrix is included here detailing the baseline shots already performed in previous testing (see attachment 9).

6. Firing Detailed Schematic



Schematic 1: Firing and instrumentation systems with laser illumination



Schematic 2: Firing and instrumentation systems with laser illumination and detonators

7. Energetic Materials, Chemicals, or Hazardous Materials Involved:

- Commercial smokeless powders
- 50 BMG CCI #35 primers
- RP-80 open-faced detonators

8. Instrumentation:

- High-speed optical imaging systems (SGDL supplied)
- Pressure transducers and oscilloscopes (SGDL supplied)

9. Specific Tools and Equipment

- Universal receiver gun system
- 0.50-inch and 0.55-inch barrels
- Gun system fireset
- Reloading press
- Scale with tenth of a grain resolution (milligram resolution)
- Working ventilation system
- Fire Extinguishers. Minimum requirements: One Class ABC fire extinguisher
 - It will be noted that in the event of a fire all personnel are to evacuate the BSL and contact campus police.
- Instrumentation and diagnostics as needed, provided by the SGDL.

10. Documentation

SGDL will provide technical data to include high-speed images and any other specific technical data as needed.

11. Instructions for Spill Cleanup and Disposal of any Scrap and Waste A&E:

- See attachment 2.
- Any spilled smokeless powder will be collected, and determination made if still usable:
 - If powder is still usable, it is not considered waste and will be used or stored as applicable and per regulatory requirements.
 - Powder deemed not suitable for use in the gun system will be properly containerized in a designated container and stored as applicable and per regulatory requirements. NO disposal of powder is required for this testing.

12. Specific Hazards:

- Explosive Hazards
- Fragmentation Hazards
- Inhalation Hazards (Smokeless powder)
- Laser Illumination Source Hazards

13. PPE Required

- Safety glasses and hearing protection will be worn by all personnel present during loading and firing of the gun system.

- Appropriate laser safety goggles will be used if laser diagnostics are employed during testing:
 - Laser safety glasses rated at OD5 or greater for 640 nm. These laser glasses are required within the building whenever the laser key is inserted.
- Steel toe shoes will be required for personnel participating in cleaning of the sand catch as described in attachment 7.

14. Emergency Procedures:

See Attachment 2.

15. Proposed Test Schedule

Testing may take place anytime Monday through Friday during normal EMRTC Field Lab operation hours. Planned testing dates will be placed on the EMRTC schedule prior to testing.

16. References

- SOP 101, Health and Safety
- SOP 102, Field Laboratory Safety
- SOP 103, Industrial Safety
- SOP 201, Grounding Procedures
- SOP 202, Initiation of Energetic Materials
- SOP 203, Arms, Ammunition and Explosives Procedures
- SOP 204, General Gun Firing Procedures
- SOP 402, Emergency Action Plan
- SOP 403, Risk Management
- SOP 404, Hazardous Waste

17. Attachments

- Job Hazard Analysis
- Safety and General Requirements
- Site Closure Map
- Tailgate Briefing Form
- Gun Start of Day Log
- Gun Operational Procedures
- Sand Catch Cleaning Procedures
- Safety Data Sheets
- Test Matrix

Reviewed and Accepted List

Engineer/Project Manager	Print Name Signature	Date
Safety	Print Name Signature	Date
Ordnance	Print Name Signature	Date
Instrumentation	Print Name Signature	Date
Field Supervisor	Print Name Signature	Date
Quality Control Engineer	Print Name Signature	Date
Associate Director	Print Name Signature	Date
Director	Print Name Signature	Date

Test Plan Revision

Reason for revision:											
Engineer Signature:											
Date:											
Safety:		Ord:		Inst:		Field:		QA:		Dir:	
Reason for revision:											
Engineer Signature:											
Date:											
Safety:		Ord:		Inst:		Field:		QA:		Dir:	
Reason for revision:											
Engineer Signature:											
Date:											
Safety:		Ord:		Inst:		Field:		QA:		Dir:	
Reason for revision:											
Engineer Signature:											
Date:											
Safety:		Ord:		Inst:		Field:		QA:		Dir:	

Attachment 1

Job Hazard Analysis

Attachment 2

Safety and General Requirements

Fire Sets:

- The fire set will have a positive interlock (e.g., key/shorting device) which will prevent the inadvertent firing of the system when removed.
- The Ordnance Technician/Gunner will keep the key/shorting device on their person at all times.
- No duplicate keys or shorting devices will be allowed on site at any time.

Hazardous Waste:

- The use, recovery, collection, transport, and storage of military munitions for Research, Development, Testing and Evaluation (RDT&E) (e.g. safety, developmental testing, surveillance function testing, static fire, or quality control or assurance testing) is considered use for intended purpose and not subject to regulation under Resource Conservation and Recovery Act (RCRA). (Military Munitions Rule (MMR) paragraph 3.B.2.b.)
- As long as all excess energetic material is destroyed on site, and not removed from the test range, it is not considered waste and does not fall under RCRA. (MMR paragraph 10.C.3.)
- Any spilled loose material will be completely gathered up and determined if the material is still usable.
- If the material is still usable, it is not considered waste and should be used or stored as applicable.
- Spilled material deemed unusable will be properly containerized, labeled, and stored for later disposal in accordance with local policies and procedures.

Misfire Procedures:

The following steps are to be performed only by the Gun Operator. Eye and ear protection is to be worn by all personnel during these steps

There are two misfire procedures depending on the use of detonators. Wait time for gun or detonators will increase to 30 minutes when detonators are in use. See attachment 6 for further details.

Gun Misfire Procedure if Detonators are Not in Use

- In the case of a gun system misfire, verbally announce “MISFIRE” to all personnel, disconnect power to the firebox and lock the firebox, and begin a 30 second count
- After 30 seconds, attempt to fire the gun again repeating the verbal “MISFIRE” announcement, disconnecting and closing the firebox, and allowing for a 30 second count for each failed attempt. Make up to **three attempts** before moving onto the following misfire procedures
- Make sure the firebox is disconnected, locked, and the firebox key is with the gun operator before approaching the gun. If using detonators, disconnect the FS-17.
- Approach the gun from rear and turn Air Input Valve to “SAFE”
- If cocking lever has not been pulled, disconnect cocking lever from bolt. Lower the bolt and use extraction tool to remove loaded case
- Return loaded case to loading bench
- Disarm SI-LUX laser announcing “LASER DISARMED” and “LASER OFF”, the gun operator retains the SI-LUX ARM KEY

- Inspect the gun system to determine the cause of the misfire
 - If the misfire occurred due to a failure of the firing system (failure to trigger, broken firing pin, etc), make the necessary repairs to the firing system. After repairs are made to the system, the loaded case can be used.
 - If the firing system was observed to operate and a primer indentation is found on the loaded case, return loaded case to loading bench, remove foam wadding, and pour powder into weigh boat. Leave powder and set misfired primed case to the side. Return to beginning of firing procedure to proceed forward reloading a new case
- If another misfire is observed with a newly primed case, suspend testing until the misfire cause has been identified and rectified. Powder should be returned to source container and impacted primer to the lock box for later removal by EMRTC personnel
- During the wait time, the engineer/test manager and the ordnance technician will contact the Ordnance Supervisor, Safety Officer and the Associate Director or their designated representatives, to inform them of the misfire and to discuss troubleshooting options.

Detonator Misfire Procedure if Detonators are in Use

- If there are no indications that the detonator, ignitor, etc., initiated, all connections will be checked (in the bunker or personnel shelter only) to ensure they are connected correctly. If instrumentation does not need to be reset, then another attempt to fire may be made. The engineer/test manager will be consulted prior to attempting to fire again.
- If there is still no indication that the detonator or ignitor initiated, begin the applicable wait time as stated below:
 - All electric misfires will include a 15-minute wait time before personnel are permitted to approach the test article, unless determined to be otherwise.
 - All non-electric misfires will include a 30-minute wait time before personnel are permitted to approach the test article, unless determined to be otherwise.
- During the wait time, the engineer/test manager and the ordnance technician will contact the Ordnance Supervisor, Safety Officer and the Associate Director or their designated representatives, to inform them of the misfire and to discuss troubleshooting options.

Emergency Procedures:

- Lightning: (reference procedures in SOP 104)
- Fire:
 - If there is a fire on or near the test pad, all personnel will evacuate to the personnel shelter immediately (or further depending on the severity of the fire) and the safety office will be notified.

WARNING
Personnel WILL NOT fight a fire that could have any remote possibility of involving explosives.

WARNING
Personnel WILL NOT fight a fire that is located off of the test pad. There is a strong possibility of unexploded ordnance being present off of the test pad.

- Unexpected Explosion:
 - All personnel will immediately assemble at the personnel shelter (or other previously identified location) and all personnel accounted for.
 - All personnel will be checked for possible injuries, first aid applied as needed, and the area inspected for remaining hazards by ordnance personnel.
 - Emergency Medical Services will be called for assistance, if needed.
 - The safety office will then be notified immediately.

WARNING
If an explosion involves the Ordnance Technician (or any other personnel) on the test pad, personnel in the personnel shelter must make a determination whether or not it is safe to attempt to treat or assist the individual on the test pad.

Personnel and AA&E Limits:

- Limit exposure to a minimum number of personnel, for a minimum amount of time, to the minimum amount of hazardous material consistent with safe and efficient operations.
- Personnel Limits – All non-essential personnel will be located in the personnel shelter during all operations involving the handling of energetic material unless prior approval has been granted from the Safety Office.
- Explosive Limits – Only explosives needed for a single test will be allowed on the test pad at any one time.

Indicators for Identifying Abnormal Process Conditions:

- Damage to projectile catch box.
 - Damage to vacuum chamber.
- Failed gun or instrumentation checkouts.

Attachment 3

Site Closure



Site Closure

The following site closure shown in the map above will be observed:

1. Two Ton and the Torres facility magazine north west of the BSL building will be cleared and closed to personnel during testing
2. West Lab, East Lab, Vacuum Stability and the Torres facility magazine north of the BSL building will be open to personnel, but the personnel will remain behind the closure gate during testing. The Gun Operator is responsible for ensuring personnel at the listed facilities understand the closure and is responsible for providing these personnel clearance to enter or exit
3. The gate to East and West Labs will be closed.
4. The chain gate at the start of the access road leading to the BSL and lower Torres facilities will be closed
5. A Z-sign will be placed in front of the chain gate at the start of the access road leading to the BSL and lower Torres facilities as shown
6. A Z-sign will be placed at the top of the exterior staircase connecting the main Torres building to the BSL building
7. Personnel may work in the main Torres building during testing

Surface Danger Zone (SDZ)

The powder gun system is mounted in a fixed position with the barrel axis horizontal to the ground plane and the barrel bore 1.23 meters (48.5 inches) above the ground surface. A 50 caliber conical projectile travelling at 2km/s (6600ft/s) was found to demonstrate the farthest fly out distance of the projectile shapes and sizes to be tested at the maximum theoretical muzzle velocity. This maximum fly out distance was calculated to be 770 meters (2530 feet) for the fixed horizontal orientation of the gun barrel. With the applied engineering controls, the surface danger zone (SDZ) for testing at the BSL with the powder gun system is reduced to a 100 meters (330 feet) radius with a 30-degree arc as shown in the site closure map above. The applied engineering controls to reduce the SDZ are as follows:

1. The powder gun is fixed to a test stand. This test stand ensures the gun's axis is horizontal to the ground to mitigate over shoot of projectile stops and the gun's axis is oriented parallel to the building NW centerline to minimize risk of projectiles missing projectile stops
2. Two primary projectile stops are employed to restrict potential projectile fly out to no more than 100 meters (330 feet):
 - a. The primary projectile stop is installed down range of the gun system at the NW end of the BSL building. This stop is nominally 24" high by 24" wide by 36" deep and consists of a solid fill of dry sand. The primary stop will be no more than 15.15 meters (50 feet) from the muzzle of the gun system to minimize the possibility of a projectile missing the stop due to vertical or horizontal drift during flight
 - b. The secondary projectile stop is the earthen hill directly behind the primary projectile stop. This hill starts approximately 57.6 meters (190 feet) from the gun emplacement and rises approximately 45.5 meters (140 feet) above the gun emplacement. This secondary stop ensures any projectiles that miss the primary projectile stop due to vertical or horizontal drift are restricted to a horizontal fly out of no more than 100 meters (330 feet)

Attachment 4

Tailgate Briefing Form

Attachment 5

Gun System Start of Day Log

START OF DAY LOG SHEET FOR GUN SYSTEM

(If already completed for the day of testing, go to operation procedures)

1.1. Testing Conditions and Test Matrix:

- 1.1.1. Test Engineer: _____
- 1.1.2. Gun Operator: _____
- 1.1.3. Safety: _____
- 1.1.4. Note date/time: _____
- 1.1.5. Barometric pressure (inHg): _____
- 1.1.6. BSL inside temperature: _____
- 1.1.7. Number of planned gun tests: _____
- 1.1.8. Test matrix with powder loads to be used is attached
Test Engineer Signature: _____
- 1.1.9. File Start of Day Log Sheet in designated folder at BSL
- 1.1.10. File Tailgate Briefing Form in designated folder at BSL
- 1.1.11. Pre-Test walkthrough completed with Dr. Hargather or EMRTC
representative:

Attachment 6

Gun System Operational Procedures

The following operational procedures apply when using the SI-LUX 640 spoiled coherence 640nm laser illumination source for high speed imaging (henceforth referred to as “laser illumination source”, “laser”, or “SI-LUX”). The following modifications to test procedures apply to all projectiles.

1. GUN PRETEST PROCEDURES

(If already completed and start of new test, go to 2)

1.1. Start of Day

- 1.1.1. Ensure Start of day log has been filled and filed with a copy of test matrix at BSL
- 1.1.2. Ensure Tailgate Briefing has been performed and form filed at BSL. Repeat if any new personnel arrive on site during testing. Gun Operator performs this review
- 1.1.3. Check that a Z-sign is on entry road to Torres facility and a Z-sign is in place at the start of the stairs to the Ballistics Science Building (BSL) according to site closure map
- 1.1.4. Check the Torres Main Building. If non-test related personnel are to be present in the Torres Main Building, inform them of testing to be performed in the BSL. Personnel may enter or exit Torres Main Building at will during testing in BSL.
- 1.1.5. Ensure Torres facilities North of BSL, labeled in red in the Site Closure figure are clear of personnel.
- 1.1.6. Check that the closure gate is closed according to the site closure map. Ensure personnel at West Lab, East Lab, Vacuum Stability and the Torres facility magazine north of the BSL building are aware that they are to remain behind the closure gate during testing and must obtain clearance from the Gun Operator to enter or leave the area
- 1.1.7. Review fire procedures with all personnel to be present during testing. Repeat if any new personnel arrive on site during testing. Gun Operator performs this review
- 1.1.8. Distribute PPE (hearing protection, laser safety goggles, and safety glasses) to all personnel to be present during testing

1.2. System Hardware Checkouts (Firebooth, gun system, sabot stripper (where applicable), and ventilation system)

- 1.2.1. Ensure power is off to Firebox (No green or red light) by disconnecting the power supply
- 1.2.2. Ensure Firebox cage is locked
- 1.2.3. Approach gun from rear and switch Air Input Valve on air cylinder to “SAFE”
- 1.2.4. Visually confirm breech and barrel are clear. As required to conduct visual inspection, disconnect cocking gear, open breech, and/or remove Chamber Flag
- 1.2.5. Insert Chamber Flag into breech
- 1.2.6. Check lateral play in recoil carriage. If play in the assembly is found, discontinue testing until recoil carriage has been disassembled and all fasteners checked and appropriately tightened
- 1.2.7. Check that red barrel retainer nut is tight
- 1.2.8. Check play in the bolt handle assembly. If play in the bolt assembly is found, discontinue testing until all fasteners have been checked and appropriately tightened
- 1.2.9. Connect yellow airline to compressor or suitable compressed air supply (120psi main supply maximum)
- 1.2.10. Set regulator pressure on compressor or air supply between 80 and 120psi
- 1.2.11. Visually inspect sabot stripper for damage which could degrade operation and ensure sandbags are in place on bottom tray
- 1.2.12. Situate ventilation duct perpendicular to muzzle of barrel. Duct opening should be two feet from barrel exit. Turn on ventilation system
- 1.2.13. Visually inspect BSL building to ensure no equipment/hardware are in the line of fire of the gun system that is not designed to be so. Ensure all cleaning supplies and any flammables are safely stored behind the firing line

1.3. Fire System Checkout

- 1.3.1. Ensure that laser warning signs are posted on the East and West doors to BSL, place the door barricades across the East and West doors, note the laser operator as the gun operator
- 1.3.2. Ensure power to Firebox is disconnected, Firebox cage is locked, breech is open, Air Input Valve is set to “SAFE”, and Chamber Flag is inserted in breech
- 1.3.3. Pull air cylinder rod up to extend. Extend rod until it stops
- 1.3.4. Turn Air Input Valve to “ARM”
- 1.3.5. Return to Firebooth
- 1.3.6. Obtain CAGE KEY and FIRE KEY from lockbox
- 1.3.7. Obtain SI-LUX ARM KEY from instrumentation
- 1.3.8. Confirm all persons present during testing are ready for a trigger check, announce LASER GOGGLES ON
- 1.3.9. Arm the laser using SI-LUX software announcing ARMING LASER and LASER ARMED when the laser illumination source is being armed and is armed
- 1.3.10. Using the SI-LUX ARM KEY arm the laser announcing LASER ARMED when the laser is ARMED
- 1.3.11. Return to the Firebooth
- 1.3.12. Open Firebox Cage
- 1.3.13. Connect power supply to Firebox and ensure power is supplied (Green light on)
- 1.3.14. Insert FIRE KEY into Firebox, turn to arm system (Red light on), and press fire button
- 1.3.15. Disconnect power from Firebox (no green or red light) and close and lock Firebox Cage. Gun Operator retains CAGE KEY and FIRE KEY for all following steps
- 1.3.16. Approach gun system and turn Air Input Valve to “SAFE”. Visually confirm air cylinder rod has retracted
- 1.3.17. When the gun system has been Safed approach the laser illumination source, check that the laser has been disarmed. disarm the SI-LUX if necessary announcing LASER DISARMED
- 1.3.18. Turn off the laser illumination source and keep the SI-LUX ARM KEY announcing LASER OFF when clear
- 1.3.19. If air cylinder rod retracts and system operates as expected, the gun system is ready for operation.
- 1.3.20. If the air cylinder fails to retract, Gun Operator should repeat steps 1.3.2 through 1.3.13 after checking the following:
 - Air Input Valve is set to “ARM”
 - Air is supplied to control solenoid
 - Trigger line from Firebox to control solenoid is undamaged
 - Firebox outputs power when fire button is depressed

2. GUN FIRING PROCEDURE

(May only begin if Start of Day Pretest Sheet and all system checkouts have been performed. Perform for each test firing of the gun system)

2.1. System Alignment

- 2.1.1. Ensure power to Firebox is disconnected, Firebox cage is locked, breech is open, Air Input Valve is set to “SAFE”, and Chamber Flag is inserted in breech
- 2.1.2. Remove Chamber Flag and insert laser bore sight
- 2.1.3. Align target/gun for desired impact point
- 2.1.4. Visually inspect sabot stripper for damage which could degrade operation and ensure sandbags are in place on bottom tray
- 2.1.5. Align sabot stripper to ensure projectile will not impact stripper plate
- 2.1.6. When alignment complete, remove bore sight and insert Chamber Flag

2.2. Cartridge Loading

- 2.2.1. Ensure power to Firebox is disconnected, Firebox cage is locked, breech is open, Air Input Valve is set to “SAFE”, and Chamber Flag is inserted in breech
- 2.2.2. Clear BSL ground floor of all non-essential personnel. Non-essential personnel are to remain in the Visitors and Instrumentation Observation Loft during loading and firing of the gun system. The Firebooth is restricted to a maximum of five essential personnel only. The Test Engineer, Gun Operator, and Safety are the personnel considered essential
- 2.2.3. Turn on ventilation fan. Ventilation fan is to remove combustion gases from BSL whenever necessary

The following steps are to be conducted by the Gun Operator only. Eye protection is required for all steps for all personnel, hearing protection is required for the gun operator from Step 2.2.9 and from Step 2.2.14 for all other personnel until the gun has been cleared. The CAGE KEY FIRE KEY and SI-LUX ARM KEY are to remain on the Gun Operator’s person at all times unless inserted in the Firebox Cage lock, Firebox, or SI-LUX laser unit, respectively.

- 2.2.4. Obtain propellant to be used for testing from the back room and bring to the loading bench. ONLY ONE powder may be on the loading bench at any given time
- 2.2.5. Install resizing dies on 50 BMG reloading press on loading bench
- 2.2.6. Deprime and resize propellant case (cutdown 50 BMG case)
- 2.2.7. If case originally had a crimped primer, deburr primer pocket
- 2.2.8. Use rotary scraper to remove carbon deposits
- 2.2.9. If removed primer was impacted, but did not initiate, return impacted primer to the lock box for later removal by EMRTC personnel

- 2.2.10. Remove resizing dies and install primer installing tool on 50 BMG reloading press
- 2.2.11. Insert No. 35 50 BMG primer, open end up, into tool and resized case into holder. Fully press primer into case (press until tool stops at preset depth). Check that primer face is recessed (~0.005") below surface of the case base
- 2.2.12. Weigh out desired powder load for test using weigh boat on scale
- 2.2.13. Pour powder that has been weighed out into case using funnel. Press floral foam into case to fill empty volume and ensure powder is retained against primer
- 2.2.14. Place the projectile and loaded cartridge onto opposing sides of the gun stand and approach the laser illumination source
- 2.2.15. Announce LASER GOGGLES ON, arm laser announcing ARMING LASER and LASER ARMED when each step is completed
- 2.2.16. Turn on the laser illumination source using the SI-LUX ARM KEY announcing LASER ON
- 2.2.17. Return to gun and load projectile using depth gauge to achieve desired insertion depth in breech
- 2.2.18. Verbally announce "EARS ON, LOADING GUN" to all personnel. Insert loaded case into breech and close bolt
- 2.2.19. Engage cocking lever, then move to rear of gun and turn Air Input Valve to "ARM"
- 2.2.20. Return to Firebooth
- 2.2.21. Ensure non-essential personnel are behind barricades in the loft. Ensure essential personnel are behind Firebooth barricades
- 2.2.22. Open Firebox Cage and connect power to Firebox (Green light on)
- 2.2.23. Verbally announce "KEY IN" to all personnel and insert FIRE KEY into Firebox. Turn FIRE KEY to arm Firebox (Red light on)
- 2.2.24. Verbally announce countdown "FIRING IN THREE, TWO, ONE" to all personnel. Press orange fire button
- 2.2.25. After gun fires, verbally announce "KEY OUT" to all personnel, remove key from Firebox, disconnect power from Firebox, and lock Firebox Cage. Retain CAGE KEY and FIRE KEY on person. Proceed to the Clear Gun Procedure (Section 2.3)
- 2.2.26. If gun fails to fire, verbally announce "KEY OUT" to all personnel, remove key from Firebox, disconnect power from Firebox, and lock Firebox Cage. Retain CAGE KEY and FIRE KEY on person. Proceed to the Gun Misfire Procedure (Section 2.3)

2.3. Misfire Procedure:

The following steps are to be performed only by the Gun Operator. Eye and ear protection is to be worn by all personnel during these steps

- 2.3.1. Ensure power to Firebox is disconnected and Firebox cage is locked
- 2.3.2. Call safety office to alert of misfire and walk through steps 2.4.3-2.4.14 together
- 2.3.3. Verbally announce "MISFIRE, 30 SECOND COUNT" to all personnel and begin a 30 second count

- 2.3.4. Approach gun from rear and turn Air Input Valve to “SAFE”
- 2.3.5. If cocking lever has not been pulled, disconnect cocking lever from bolt
- 2.3.6. Lower bolt and use extraction tool to remove loaded case
- 2.3.7. Return loaded case to loading bench and approach laser illumination source
- 2.3.8. Disarm SI-LUX laser announcing LASER DISARMED and LASER OFF, the gun operator retains the SI-LUX ARM KEY
- 2.3.9. If the misfire occurred due to a failure of the firing system (failure to trigger, broken firing pin, etc), return loaded case to loading bench. Make the necessary repairs to the firing system and return to Section 1.3: Fire System Checkout before returning to Step 2.2.13
- 2.3.10. If the firing system was observed to operate and a primer indentation found on the loaded case, return to Step 2.2.13 and proceed
- 2.3.11. If three misfires are observed, return loaded case to loading bench, remove foam wadding, and pour powder into weigh boat. Leave powder and set misfired primed case to the side. Return to beginning of firing procedure to proceed forward reloading a new case
- 2.3.12. If another misfire is observed with a newly primed case, suspend testing until the misfire cause can be identified and rectified
- 2.3.13. If three misfired are observed, return loaded case to loading bench, remove foam wadding, and pour powder to source container and set misfired primer to the side. Return to beginning of firing procedure to proceed forward reloading a new case
- 2.3.14. If another misfire is observed with a newly primed case, suspend testing until the misfire cause has been identified and rectified. Powder should be returned to source container and impacted primer to the lock box for later removal by EMRTC personnel

2.4. Clear Gun Procedure:

The following steps are to be performed only by the Gun Operator. Eye and ear protection is to be worn by all personnel until gun has been announced as clear

- 2.4.1. Ensure power to Firebox is disconnected and Firebox cage is locked
- 2.4.2. Approach gun from rear and turn Air Input Valve to “SAFE”
- 2.4.3. Lower bolt and use extraction tool to remove case from breech. If case cannot be extracted using extraction tool, insert the brass pushrod into the muzzle and push case out of breech
- 2.4.4. Visually inspect breech/bore to ensure barrel is clear
- 2.4.5. Insert Chamber Flag into breech and verbally announce “GUN CLEAR” to all personnel
- 2.4.6. Approach the laser illumination source, disarm the laser announcing LASER DISARMED, and LASER OFF. Retain SI-LUX ARM KEY on person
- 2.4.7. Personnel may now remove laser safety goggles and return to the BSL main floor
- 2.4.8. For continued testing, return to step 2.1.1

3. GUN POST TEST PROCEDURES

(Proceed if all testing with the gun system is complete for the day)

3.1. System Hardware Shutdown (Firebooth and gun system)

- 3.1.1. Ensure power is off to Firebox (No green or red light) by disconnecting the power supply
- 3.1.2. Ensure Firebox Cage is locked
- 3.1.3. Approach gun from rear and switch Air Input Valve on air cylinder to “SAFE”
- 3.1.4. Visually confirm breech and barrel are clear. As required to conduct visual inspection, disconnect cocking handle, open breech, and/or remove Chamber Flag
- 3.1.5. Insert Chamber Flag into breech
- 3.1.6. Disconnect yellow airline from air supply
- 3.1.7. Return CAGE KEY and FIRE KEY to lockbox
- 3.1.8. Turn off ventilation system

4. RP-80 Detonator Testing and Gun Firing Procedure

4.1. System Alignment

- 4.1.1. Ensure power to Firebox is disconnected, Firebox cage is locked, breech is open, Air Input Valve is set to "SAFE", and Chamber Flag is inserted in breech
- 4.1.2. Remove Chamber Flag and insert laser bore sight
- 4.1.3. Target/gun for desired impact point
- 4.1.4. Place detonation holder in the desired location
- 4.1.5. Inspect sabot stripper for damage that could degrade operation and ensure sandbags are in place on the bottom tray
- 4.1.6. Inspect sabot stripper to ensure projectile will not impact stripper plate
- 4.1.7. When alignment is complete, remove bore sight and insert Chamber Flag

4.2. Cartridge Loading

- 4.2.1. Ensure power to Firebox is disconnected, Firebox cage is locked, the breech is open, Air Input Valve is set to "SAFE", and Chamber Flag is inserted in the breech
- 4.2.2. Clear BSL ground floor of all non-essential personnel. Non-essential personnel is to remain in the Visitors and Instrumentation Observation Loft during the loading and firing of the gun system. The Firebooth is restricted to a maximum of five essential personnel only. The Test Engineer, Gun Operator, and Safety are the personnel considered essential
- 4.2.3. Turn on the ventilation fan. A ventilation fan is to remove combustion gases from BSL whenever necessary

The following steps are to be conducted by the Gun Operator only. Eye protection is required for all steps for all personnel, hearing protection is required for the gun operator for all other personnel until the gun has been cleared. The CAGE KEY FIRE KEY and SI-LUX ARM KEY are to always remain on the Gun Operator's person unless inserted in the Firebox Cage lock, Firebox, or SI-LUX laser unit, respectively.

- 4.2.4. Obtain propellant to be used for testing from the back room and bring it to the loading bench. ONLY ONE powder may be on the loading bench at any given time
- 4.2.5. Install resizing dies on a 50 BMG reloading press on the loading bench
- 4.2.6. De-prime and resize propellant case (cutdown 50 BMG case)
- 4.2.7. If the case originally had a crimped primer, deburr primer pocket
- 4.2.8. Use the rotary scraper to remove carbon deposits
- 4.2.9. If removed primer was impacted, but did not initiate, return impacted primer to the lockbox for later removal by EMRTC personnel
- 4.2.10. Remove resizing dies and install primer installing tool on 50 BMG reloading press
- 4.2.11. Insert No. 35 50 BMG primer, open the end up into the tool, and resized the case into the holder. Fully press primer into the case (press until tool stops at preset depth). Check that the primer face is recessed (~0.005") below the surface of the case base
- 4.2.12. Weigh out desired powder load for test using weigh boat on scale

- 4.2.13. Pour powder that has been weighed out into the case using a funnel.
- 4.2.14. Press floral foam into the case to fill the empty volume and ensure powder is retained against the primer
- 4.2.15. Place the projectile and loaded cartridge onto opposing sides of the gun stand

Only Ordnance will carry out steps 4.2.16 - 4.2.18, and 4.2.26

- 4.2.16. Insert the RP-80 detonator into the detonator holder from the back, detonator will remain disconnected from the firing line during insertion and cartridge loading
- 4.2.17. Ensure detonator is flush to the small lip at the front of the holder, and tape it in place from the back
- 4.2.18. Connect long detonator leads (5m to 30m in length) to the detonator so that it can be connected to the firing line from behind the gun or inside the firing booth after the cartridge is loaded.

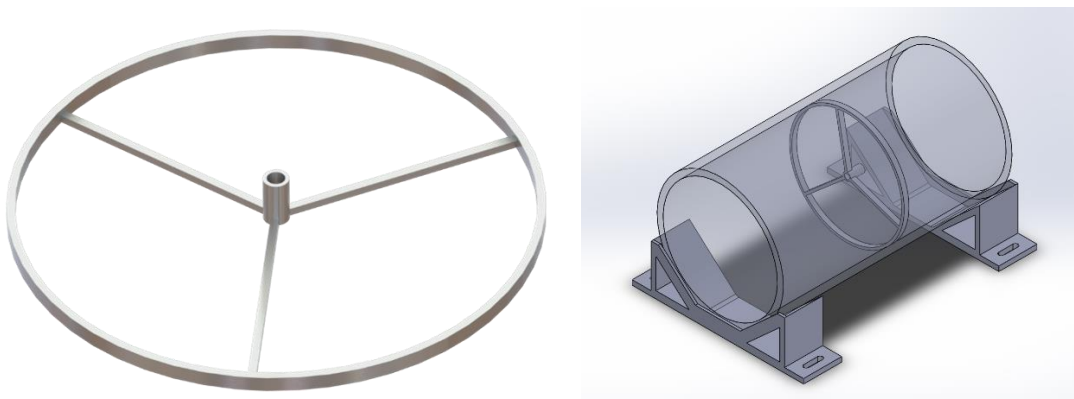


Figure 1: Image on the left is the detonator holder, and the diagram on the right is the fully assembled detonator holder with the casing (shown in grey) being a 6” PVC pipe, the detonator holder (shown as a dashed line) placed inside the PVC pipe, and the detonator (shown in blue) placed in the center of the holder.

- 4.2.19. Announce LASER GOGGLES ON, arm laser announcing ARMING LASER and LASER ARMED when each step is completed
- 4.2.20. Turn on the laser illumination source using the SI-LUX ARM KEY announcing LASER ON
- 4.2.21. Return to gun and load projectile using depth gauge to achieve desired insertion depth in breech
- 4.2.22. Verbally announce “EARS ON, LOADING GUN” to all personnel. Insert loaded case into the breech and close bolt
- 4.2.23. Engage cocking lever, then move to the rear of the gun and turn Air Input Valve to “ARM”
- 4.2.24. Return to Firebooth
- 4.2.25. Ensure non-essential personnel are behind barricades in the loft. Ensure essential personnel are behind Firebooth barricades

- 4.2.26. Ordnance will connect detonator firing line to the FS-17 fire set
- 4.2.27. Open Firebox Cage and connect power to Firebox (Green light on) Verbally announce “KEY IN” to all personnel and insert FIRE KEY into Firebox.
- 4.2.28. Ordnance charge fs_17, announce “READY TO FIRE”
- 4.2.29. Turn FIRE KEY to arm Firebox (Red light on) Verbally announce countdown “FIRING IN THREE, TWO, ONE” to all personnel. Press the orange fire button
- 4.2.30. After the gun fires, verbally announce “KEY OUT” to all personnel, remove the key from Firebox, disconnect power from Firebox, and lock the Firebox Cage. Retain the CAGE KEY and FIRE KEY on the person. Proceed to the Clear Gun Procedure (Section 9.3)
- 4.2.31. If the gun fails to fire, verbally announce “KEY OUT” to all personnel, remove the key from Firebox, disconnect power from Firebox, and lock the Firebox Cage. Retain the CAGE KEY and FIRE KEY on the person. Proceed to the Gun Misfire Procedure
- 4.2.32. If detonator fails to fire, but gun fires then attempt to fire the detonator again will be made using the FS-17 directly. If detonator still fails to function, a 30 minute wait time will be started. Then the gun will be cleared, the laser turned off, and the RP-80 cleared.

4.3. Clear Gun Procedure:

The following steps are to be performed only by Ordnance. Eye and ear protection is to be worn by all personnel until the gun has been announced as clear

- 4.3.1. Ensure power to Firebox is disconnected and the Firebox cage is locked
- 4.3.2. Ordnance will disconnect the firing line from the fire set
- 4.3.3. Approach the gun from the rear and turn Air Input Valve to “SAFE”
- 4.3.4. Lower the bolt and use the extraction tool to remove the case from the breech. If the case cannot be extracted using the extraction tool, insert the brass pushrod into the muzzle and push the case out of the breech
- 4.3.5. Visually inspect breech/bore to ensure barrel is clear
- 4.3.6. Insert Chamber Flag into breech and verbally announce “GUN CLEAR” to all personnel
- 4.3.7. Approach the laser illumination source, disarm the laser announcing LASER DISARMED, and LASER OFF. Retain SI-LUX ARM KEY on person Personnel may now remove laser safety goggles and return to the BSL main floor
- 4.3.8. For continued testing, return to step 4.1.1

4.4. Gun Misfire Procedure:

- 4.4.1. Ensure power to Firebox is disconnected and Firebox cage is locked

Only ordnance will conduct steps 4.4.2-4.4.3

- 4.4.2. Ordnance will detonate the detonator
- 4.4.3. Ordnance will disconnect the firing line from the fire set

The following steps are to be performed only by the Gun Operator. Eye and ear protection is to be worn by all personnel during these steps

- 4.4.4. Call safety office to alert of misfire and walk through steps 4.4.4-4.4.16 together
- 4.4.5. Verbally announce “MISFIRE, 30 SECOND COUNT” to all personnel and begin a 30 second count
- 4.4.6. Approach gun from rear and turn Air Input Valve to “SAFE”
- 4.4.7. If cocking lever has not been pulled, disconnect cocking lever from bolt
- 4.4.8. Lower bolt and use extraction tool to remove loaded case
- 4.4.9. Return loaded case to loading bench and approach laser illumination source
- 4.4.10. Disarm SI-LUX laser announcing LASER DISARMED and LASER OFF, the gun operator retains the SI-LUX ARM KEY
- 4.4.11. If the misfire occurred due to a failure of the firing system (failure to trigger, broken firing pin, etc), return loaded case to loading bench. Make the necessary repairs to the firing system and return to Section 1.3: Fire System Checkout before returning to Step 2.2.13
- 4.4.12. If the firing system was observed to operate and a primer indentation found on the loaded case, return to Step 2.2.13 and proceed
- 4.4.13. If three misfires are observed, return loaded case to loading bench, remove foam wadding, and pour powder into weigh boat. Leave powder and set misfired primed case to the side. Return to beginning of firing procedure to proceed forward reloading a new case
- 4.4.14. If another misfire is observed with a newly primed case, suspend testing until the misfire cause can be identified and rectified
- 4.4.15. If three misfired are observed, return loaded case to loading bench, remove foam wadding, and pour powder to source container and set misfired primer to the side. Return to beginning of firing procedure to proceed forward reloading a new case
- 4.4.16. If another misfire is observed with a newly primed case, suspend testing until the misfire cause has been identified and rectified. Powder should be returned to source container and impacted primer to the lock box for later removal by EMRTC personnel

Attachment 7

Sand Catch Cleaning Operation Procedures

1. SANDCATCH POST TEST PROCEDURES

A revised sand catch is used to safely catch projectiles of greater mass than the original 55 gallon drum used for RP-19-01: Study High Velocity Impact of Reactive Materials Using 0.55 Caliber Powder Gun. Specifications on the revised sand catch are in accordance with TP-19-25 for lot testing of 50 BMG. The sand catch is approximately 1800 pounds fully loaded, and as such any lifting operations will be performed by those wearing hard hats and steel toes. The Titan Telescoping Gantry Crane has the lowest capacity rating of all components in the sand catch with a load rating of 3000 pounds. The minimum factor of safety for the lifting operation is 1.7 on the published ratings for all components. No fewer than two operators will be involved with the emptying of the sand catch. The sand catch will be cleaned after a maximum of 20 shots into the catch, or at the end of a test series where the next session will exceed the maximum number of shots before cleaning.

- 1.1. Distribute appropriate PPE
- 1.2. Move the gantry crane into place and the sand catch tub and cribbing into place for receiving the sand if fully dumping
- 1.3. Ensure that the casters on the gantry crane and the catch tub are locked
- 1.4. Attach the three lifting lugs of the sand catch chain hoist to the crane using the lifting straps, and D-Ring shackles
- 1.5. Tension the chain hoist without lifting the sand catch, check that all lengths of chain are equal and tensioning properly
- 1.6. Begin lifting using the chain hoist such that the sand catch is raised off of the steel welding table
- 1.7. Unlock the casters on the gantry crane and using team pushing to position the sand catch above the catch tub
- 1.8. Position the front 4 to 10 inches of the sand catch overhanging the catch tub
- 1.9. Lower the sand catch onto the cribbing and the catch tub
- 1.10. Translate the gantry crane back and attach the rearward lifting lugs on the sand catch onto the crane
- 1.11. Remove the face plate of the sand catch using the four toggle clamps
- 1.12. Tip the catch up slightly using the gantry crane
- 1.13. Remove all of the sand from the catch using a shovel
- 1.14. Inspect the rubber plug and the plywood for damage
 - 1.14.1. Rubber plugs can be used for three shooting sessions
 - 1.14.2. Plywood is to be replaced after every other shooting session, or if any damage is noted on the face
 - 1.14.3. Visibly Inspect the AR500 back plate for damage, replace the AR500 plate if any damage is visible
- 1.15. Lay the sand catch back level, refill sand (if applicable) using shovels, and reinstall the faceplate on the catch

Attachment 8

Safety Data Sheets

Attachment 9

Test Matrix

Test Plan Revision

Reason for revision:										
<div style="border: 1px solid black; padding: 5px; margin: 0 auto; width: 80%;"> Additional test procedures for detonator only testing. </div>										
Engineer Signature:										
Date:										
Safety:		Ord:		Inst:		Field:		QA:		Dir:
Reason for revision:										
Engineer Signature:										
Date:										
Safety:		Ord:		Inst:		Field:		QA:		Dir:
Reason for revision:										
Engineer Signature:										
Date:										
Safety:		Ord:		Inst:		Field:		QA:		Dir:
Reason for revision:										
Engineer Signature:										
Date:										
Safety:		Ord:		Inst:		Field:		QA:		Dir:

Revision:

RP-80 Detonator Testing

1.1. System Alignment

- 1.1.1. Place any pressure gauges and cameras in the desired location. All devices will either be triggered externally (i.e. from the detonator shock) or from the FS-17.
- 1.1.2. Place detonation holder in the desired location

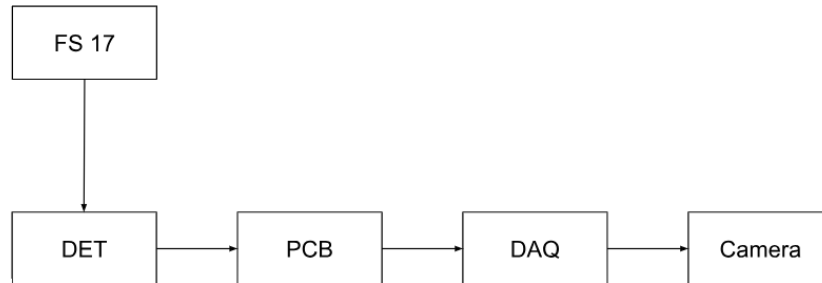


Fig: Firing and instrumentation systems with only detonators

Only Ordnance will carry out steps 1.1.1 – 1.1.3., and 1.1.9.

- 1.1.1. Insert the RP-80 detonator into the detonator holder from the back, detonator will remain disconnected from the firing line during insertion and cartridge loading
- 1.1.2. Ensure detonator is flush to the small lip at the front of the holder, and tape it in place from the back
- 1.1.3. Connect long detonator leads (5m to 30m in length) to the detonator so that it can be connected to the firing line from behind the gun or inside the firing booth after the cartridge is loaded.
- 1.1.4. Announce LASER GOGGLES ON, arm laser announcing ARMING LASER and LASER ARMED when each step is completed
- 1.1.5. Turn on the laser illumination source using the SI-LUX ARM KEY announcing LASER ON
- 1.1.6. Verbally announce “EARS ON” to all personnel.
- 1.1.7. Return to Firebooth
- 1.1.8. Ensure non-essential personnel are behind barricades in the loft. Ensure essential personnel are behind Firebooth barricades
- 1.1.9. Ordnance will connect detonator firing line to the FS-17 fire set
- 1.1.10. Ordnance charge FS_17, announce “READY TO FIRE”
- 1.1.11. Ordnance will announce “FIRING” and fire the detonator from the FS-17
- 1.1.12. If detonator fails to function, a 30 minute wait time will be started. The laser turned off and the RP-80 cleared.
- 1.1.13. After the detonator has been fired, turn off the laser announcing “Laser OFF” and ordnance will clear down range

All misfire procedures refer to page 14 of the test plan.

FULL-FIELD DENSITY MEASUREMENTS IN SUPERSONIC AND
EXPLOSIVELY DRIVEN FLOWS USING QUANTITATIVE SCHLIEREN

by

Jessica Cooke

Permission to make digital or hard copies of all or part of this work for personal or classroom use is granted without fee provided that copies are not made or distributed for profit or commercial advantage and that copies bear this notice and the full citation on the last page. To copy otherwise, to republish, to post on servers or to redistribute to lists, requires prior specific permission and may require a fee.

